Modelling temporal changes in the gravity field in the Nankai Trough Subduction Zone, Japan

by
Siri Catherine Vassvåg

Master of Science in
Geodynamics

Department of Earth Science

University of Bergen

November 2019

Abstract

The Nankai trough subduction zone off southwest Japan is prone to large earthquakes, causing tsunamis and great damages to the nearby islands. Linking the sources of these earthquakes to asperities along the plate interface is of great importance in monitoring earthquake and tsunami activity at the subduction zone. However, the location of asperities near the trough axis at the Nankai trough are not well constrained. During the interseismic period between megathrust earthquakes, shallow slow earthquakes occurring along the interface are messengers of the stress distribution outside of these asperities. They occur on areas were fluid migration on the interface leads to loosely coupled regions. Through gravity measurements, small changes in subsurface density caused by this fluid migration can be detected. These changes can be observed through time-lapse gravimetric surveys at the seafloor, allowing for detailed mapping of these gravity anomalies.

In this study, forward modelling of gravity is used to estimate variations of fluid volume needed to observe temporal changes in the gravity field above the Nankai trough subduction zone. The modelled density variations are caused by changes in fluid migration along fault planes and within the pore space of rocks. Thus, the aim is to model regions where fluid migration may trigger slow earthquakes in the shallow reaches of the subduction zone. A set of slow earthquakes are used to constrain modelling locations, assuming that fluid migration within these regions will trigger these events.

Through the time-lapse gravity modelling, an estimate has been made on the amount of fluid volume needed to be able to detect a gravity change at the seafloor. The modelling uses a threshold of 5 μGal for the minimum absolute gravity change, modelling variations of fluid volume within the Nankai trough accretionary prism and along the plate interface. The results are used to formulate a hypothesis on the change in fluid volume that is possible to detect at the seafloor, which can be tested through a time-lapse gravity survey on the seafloor above the accretionary prism. The results also indicate where measurement locations can be placed around the Nankai trough to obtain good precision for the measured gravity values during such a survey.

Acknowledgements

Firstly, I would like to express my sincerest gratitude to my supervisors Kuvvet Atakan (UiB) and Martha Lien (OEM) for always being available for assistance when I needed it. They provided me with valuable feedback and support throughout the whole two years of my masters degree.

In addition, I would like to give thanks to my co-supervisor Shuichi Kodaira, his colleague Toshiya Fujiwara, and JAMSTEC for giving me access to a detailed velocity model of the Nankai trough, without which my modelling would not have been possible. I would also like to thank Dr. Kodaira and Dr. Fujiwara for following my work and providing me with valuable feedback, and for introducing me to the GALILEO gravity database.

I would also like to thank OCTIO Gravitude for supplying the tools necessary to conduct my modelling, and for giving me the opportunity to participate in the 2018 and 2019 Summer Gravity surveys. This experience provided an exciting chance to increase my understanding of the processes behind gravity measurements, which proved very valuable while writing this thesis.

In addition, I wish to thank my parents, Theresa and Sigbjørn, and my sisters, Monique and Sarita, for always being supportive and for providing helpful advice. In particular, thank you for taking the time to proofread all these pages.

Last, but not least, thanks to my friends for their companionship and for being there when I needed to unwind during the last year of my studies. I would also like to give warm thanks to my classmates for five and a half years of their company, in particular Vilde and Regine for making my time in Bergen "the best".

Contents

Notation

Abbreviations

CMT - Centroid moment tensor

CP - Concrete platform

LFE - Low-frequency earthquakes

LFT - Low frequency tremor

OBS - Ocean-bottom seismometer

SSE - Slow slip events

TPGA - Trench-parallel gravity anomaly

TPBA - Trench-parallel Bouguer anomaly

VLFE - Very low-frequency earthquakes

VR - variance reduction

List of Figures

List of Tables

Chapter 1

Introduction

The importance of acquiring better knowledge of subduction zone processes was highlighted following the Tohoku earthquake of 2011, off northeast Japan in the Japan trench subduction zone. The earthquake reached a magnitude of M_w 9, exceeding the forecast size of M_w 7.5 (Satake 2015). Where usual earthquakes at the Japan trench would rupture a deeper portion of the interface, this event caused 50 meters of slip near the trench (Satake 2015). This lead to a large tsunami, with run-up heights as high as 20m along parts of the coast (Mori et al. 2011). The expected size and damage caused by a new earthquake was therefore highly underestimated, revealing the need for improved knowledge of the fault processes in the subduction zone.

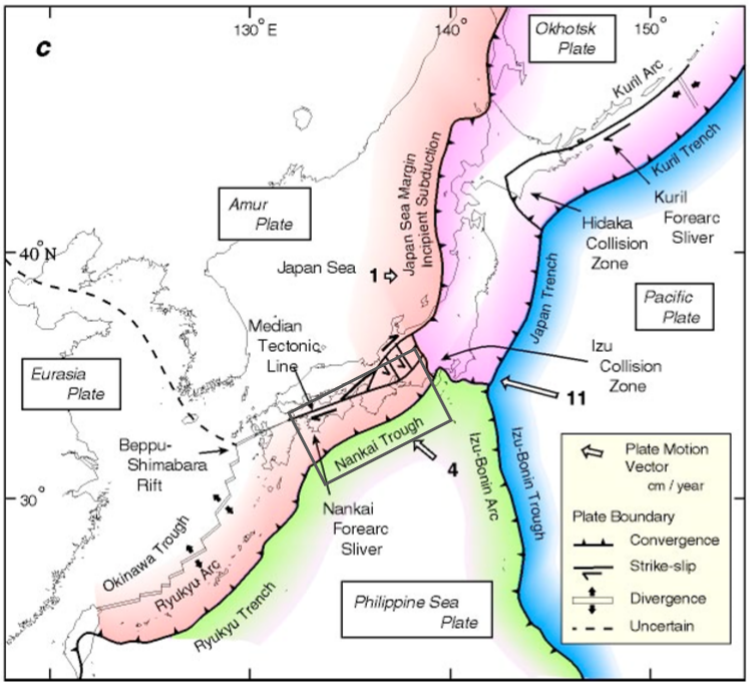

Figure 1.1: Illustration of the tectonic setting of Japan. Locations of the subduction zones are given, along with other marked fault zones in the area. The tectonic plates involved in each subduction zone are labeled. The gray square indicates the location of the study area, the Nankai trough subduction zone. The arrows indicate the convergence rate of each plate in cm/year. (Figure adapted from Figure 1 in Asahiko Taira 2001)

The Japanese islands lie among several other active tectonic regimes bordering the Pacific ocean, in what is commonly referred to as the Pacific "Ring of Fire" ((USGS) 2019). Figure 1.1 shows the Japanese islands bordered by several subduction zones, revealing the highly dynamic setting of the region. Of the four major subduction zones surrounding the islands, the Nankai trough off southwestern Japan is of particular interest for this thesis. Researching the Nankai trough subduction zone is of great importance due to the awaited occurrence of a large and possibly devastating earthquake. The last earthquakes in the subduction zone occurred in 1944 off the Kii Peninsula and in 1946 off the eastern Shikoku island, both with a magnitude of around M_w8 (Araki et al. 2017). The Japan Agency for Marine-Earth Science and Technology (JAMSTEC) estimate a 60% chance that a new earthquake of similar size to the 1944 and 1946 events will occur within 30 years (Kawaguchi et al. 2015). To be prepared for a new large earthquake, the possibility of a similar event as the 2011 Tohoku earthquake and rupture closer to the trench must be evaluated. A new earthquake may not follow the same pattern as historical earthquakes, creating a possibility of underestimating the expected damage from a new event. Extensive research and observation networks have therefore been put into place to monitor the earthquake activity at this subduction zone.

Increased information on the Nankai trough would be valuable in making sure a better understanding is achieved on the rupture processes of the megathrust earthquakes in this area. It is also important to determine the extent of stress accumulation during the interseismic period, and subsequent fault rupture during a new megathrust earthquake. In particular, acquiring better understanding of the near-trough area of the subduction zone will be valuable in evaluating whether a new earthquake here could possibly rupture a larger area than previously thought. In this research, slow earthquakes, defined as earthquakes with longer rupture time than normal earthquakes (Linde and Sacks 2002), are of particular interest. Considerable slow earthquake activity has been observed in the Nankai trough (Beroza and Ide 2011). A deeper understanding of these events and their occurrence could possibly give more information of the processes governing these events, and their relation to larger earthquakes (Beroza and Ide 2011).

The area of southwest Japan has several networks in place to monitor earthquake activity. On the seafloor, such networks include an array of GPS stations installed by the Hydrographic and Oceanographic Department of the Japan Coast Guard (JHOD) (Yokota et al. 2016) and the Dense Oceanfloor Network for Earthquake and Tsunami (DONET) (Kaneda 2014), which continuously monitor the activity within the Nankai trough subduction zone. These networks have greatly improved the coverage of information possible to obtain over the subduction zone (Masaru Nakano, Nakamura, et al. 2013; Araki et al. 2017). Even though extensive research has been done to study the processes in the Nankai trough, there is still much to learn about these major geological features. This is important especially near the trough region where coverage from onshore stations is unreliable (Masaru Nakano, Nakamura, et al. 2013; Hirai and Sagiya 2013), and offshore GPS stations still have some difficulties resolving slip values (Yokota et al. 2016; Noda, Saito, and Fukuyama 2018). Gravity measurements may therefore be useful in acquiring more information of this area, due to the sensitivity of gravimeters.

Gravity monitoring of the Nankai trough subduction zone has previously been conducted through land-based and shipborne gravimetry (Imanishi et al. 2004; Fujiwara, Goto, and Kobayashi 1998). Through the Accurate Seafloor Subduction Zone Monitoring project (ASUMO), the Norwegian company OCTIO Environmental Monitoring (OEM) wish to extend the knowledge of earthquake processes near the trough using relative gravimetry at the seafloor. Their sensitive gravimeters measure time-lapse changes in gravity between seafloor stations, and have previously been able to detect changes in measured time-lapse gravity down to less than 1 μGal (Gravitude 2019), which could prove very valuable in detecting small changes in the subduction zone prior to various earthquakes. In addition to this, improving the knowledge of temporal density changes such as fluid migration is crucial in understanding processes leading up to both slow and regular earthquakes, and to further determine locations of shallow slow earthquakes. Modelling of gravity can also contribute to

increased knowledge on asperity distributions near the trough region (T.-R. A. Song and Simons 2003; Raeesi and Atakan 2009). Considering limitations in resolution of other methods in this region, this could lead to improved knowledge of general processes within the subduction zone.

One aim of this thesis is to determine the scale of density changes within the shallow parts of the Nankai subduction zone that are possible to detect through gravity measurements at the seafloor. This is studied through forward modelling of gravity. The modelling involves processes within the subduction zone leading to fluid alterations, with particular focus on slow earthquakes. For the modelling, a detailed 3D P-wave velocity model by Nakanishi, N. Takahashi, Yamamoto, et al. (2018) is used to constrain a geological model over the area off the Kii Peninsula. Using this geological model, P-wave velocities are converted to densities, which are input values for the forward modelling of gravity.

The gravity computation is done by computing the gravity potential for a 3D distribution of rectangular prisms with known densities determined by the density map. The computation uses Newton's law of gravity and the fact that the gravity potential from an individual volume of mass affects a measurement point independently of nearby masses (Jacoby and Smilde 2009). The density map is divided into rectangular prisms, and a modelling tool developed by OCTIO models the surface gravity at specified measurement positions. Time-lapse gravity signals are analyzed as volume and density changes are applied to selected prisms, representing variations in fluid volume within sections of the rocks. The results obtained from the modelling are used to formulate hypotheses on how much fluid change is needed to detect temporal changes in the gravity field at the seafloor.

Chapter 2

Background

2.1 Tectonic setting

Some of the largest earthquakes on Earth occur at convergent plate boundaries. In particular, the forces active in subduction zones generate major and often devastating earthquakes, in some cases reaching magnitudes above M_w 9, such as the 1960 Chile and 2011 Tohoku earthquakes. To understand the mechanisms behind these major earthquakes, it is important to look at the geological settings and processes that might lead to such massive rupture events.

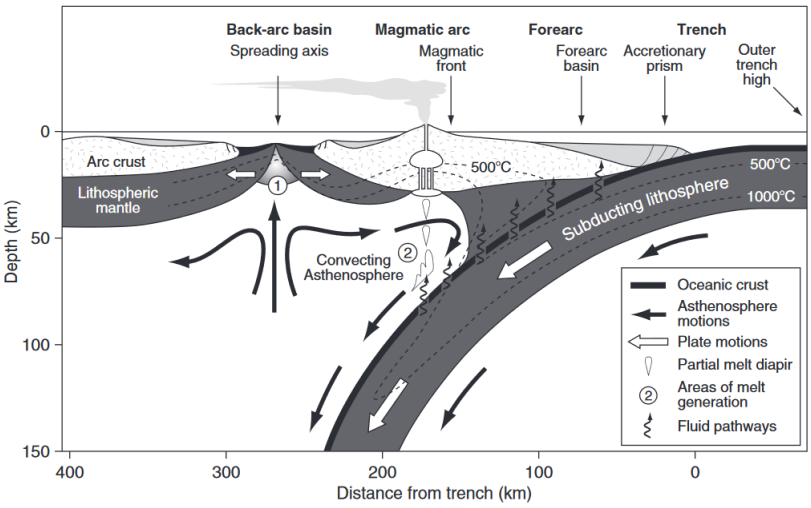

Figure 2.1: Schematic illustration of an island arc layout, from the outer trench high to the backarc basin. (Source: Kearey, Klepeis, and Vine (2009))

Figure 2.1 illustrates the layout of a typical island arc subduction zone, where the main regions of importance are shown. The Japanese islands form an island arc

system, and the subduction zones here follow this layout.

The main regions are divided into the outer trench high, also referred to as the "outer rise", trench, forearc, magmatic arc and backarc. In the contact zone between the plates, a deep trench is formed. Seaward of the trench lies the outer rise, where a bulge is created due to flexural loading on the oceanic lithosphere by the overriding crust (Engelder and Price 1993). Landward of the trench lies the forearc region, where features such as basins, ridges and accretionary prisms can be found. Following this is a mountain chain, the magmatic arc (Stein, Wysession, and Houston 2003). The magmatic arc is formed as fluids introduced into the mantle by the subducting plate cause melting of the asthenosphere above the descending plate, resulting in surface volcanism (Kearey, Klepeis, and Vine 2009). The fluids are likely introduced by mineral dehydration, and causes the mantle to melt at lower temperatures than usual (Ringwood 1974). In the back-arc region, the plate is either under compression or tension depending on certain stress variations here (Seiya Uyeda and Kanamori 1979). For island arc systems, this area tends to form a basin, reflecting backarc extension as seen in Figure 2.1.

2.1.1 General characteristics of subduction zone

The features of an island arc can vary for different subduction zones. The age of the converging plates, morphology of the descending plate and convergence rates can all affect the layout of the subduction zone (Kanamori 1971; Ruff and Kanamori 1983).

The age of the descending plate is closely linked to the the morphology of the subduction zone. For instance, considering that old oceanic plates are more dense than young plates, they tend to have a steeper subduction angle (Kearey, Klepeis, and Vine 2009). A lower dip angle leads to a larger contact zone between the overriding and descending plate in the subduction zone (Ruff and Kanamori 1983). The size of this contact zone, the plate interface, is crucial when discussing the occurrence of earthquakes here. An important concept that is closely related to the age of the subducting lithosphere, is the coupling on the plate interface between the overriding and descending plate. The concept of interplate coupling was introduced by Kanamori (1971), to describe how the two plates are connected at the interface. Kanamori (1971) noted how this connection depended on the convergence rate and density of the subducting plate, and therefore indirectly the age of the plate.

Introducing different degrees of coupling opened a new understanding of earthquake generation in fault zones (Ruff and Kanamori 1983). An area of the fault is said to be strongly coupled if little or no slip is detected along the plate interface during the interseismic period, implying that most of the slip is caused by earthquakes (Ruff and Kanamori 1983). The reason for this varying degree of coupling in the subduction zone could be the existence of subducted seamounts on the oceanic plate,

varying amounts of incoming sediments, heterogeneities in the hanging wall of the interface fault or thermal variations in rocks (Ruff and Kanamori 1983; Hyndman, Wang, and Yamano 1995). All these factors can contribute in either increasing or decreasing friction between the plates, and therefore cause some areas to be "locked" together along the plate interface. This concept will be discussed further in relation to the earthquake activity in subduction zones in Section 2.3.

The forearc region can either be defined by an accretionary or erosive margin (Clift and Vannucchi 2004). The margin experiences trench retreat as material from the overriding plate is eroded by the descending plate, and subducted along with oceanic sediments (Clift and Vannucchi 2004). Whether the subduction zone is accretionary or erosive is highly dependent on the thickness of the sediment layer on the subducting plate and the convergence rate of the plates (Kearey, Klepeis, and Vine 2009). If the subducting plate converges at higher rates than 7.6 cm/yr (Kearey, Klepeis, and Vine 2009) with an incoming sediment section of less than 1 km thickness (D. M. Saffer and Bekins 2006), the margin will likely be erosive.

In accretionary subduction zones, sediments can be scraped off of the descending plate and gathered onto the overriding plate as trench fill (Kearey, Klepeis, and Vine 2009). In addition to this, some of the sediments can be subducted along the surface of the descending plate and underplated the overriding sediment package (Clift and Vannucchi 2004). This forms the accretionary prism near the toe of the overriding plate, within which extensive faulting occurs and a diverse geological composition is created (Kearey, Klepeis, and Vine 2009).

The base of the accretionary prism is defined as the décollement, and marks the boundary between the overriding sediment package and the underthrust sediments (Kearey, Klepeis, and Vine 2009). The décollement defines a shear zone or a fault zone, depending on how developed it is (Kearey, Klepeis, and Vine 2009). Typically, mélange units form in underthrust sections of the accretionary prism, below the décollement (Gaku Kimura, Yamaguchi, et al. 2012). The composition of these mélange units show various types of rock fragments, depending on the subducting and eroded material (Kearey, Klepeis, and Vine 2009). The Nankai trough has a well developed accretionary prism (J. C. Moore and Daniel E Karig 1976), and the importance of studying it in greater detail will be discussed in Section 2.3.2, when discussing the distribution of slow earthquakes.

2.2 Study area

The Nankai trough, located off the coast of southwestern Japan, is one of several subduction zones surrounding the Japanese islands. The Japanese islands are prone to extensive earthquake activity, due to the highly dynamic tectonic setting surrounding the islands. A presentation of the Japanese islands will be made, followed

by a more detailed description of the Nankai trough and specific study area.

2.2.1 Geological setting of Japan

Figure 2.2 shows the location of the Japanese islands, along with the complicated plate boundaries here.

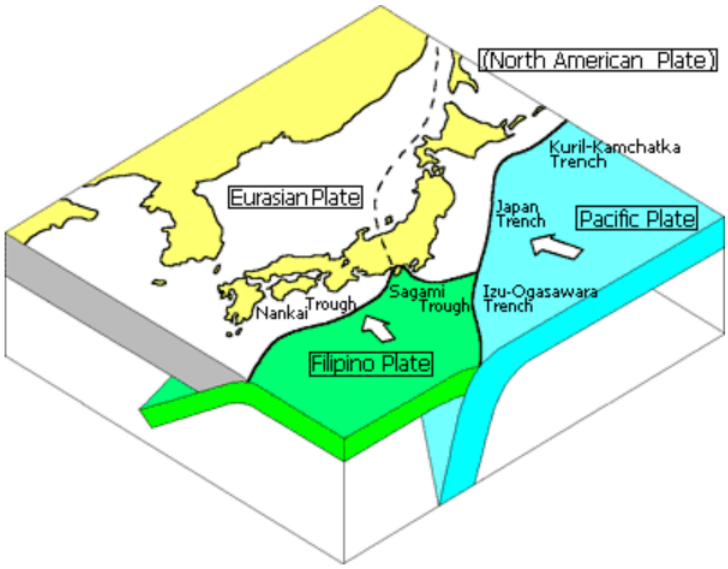

Figure 2.2: Illustration of the tectonic setting of Japan. Locations of the subduction zones are given, along with the tectonic plates involved in each subduction zone. What is here referred to as the Eurasian plate, includes the smaller Amur plate which overrides the Philippine plate at the Nankai trough. What is often referred to as the Izu-Bonin-Mariana trench is named the Izu-Ogasawara trench in the figure, and marks the subduction of the Pacific plate below the Philippine plate. (Source: Y. Okada (2013))

The islands are surrounded by five trench systems: the Ryukyu trench, the Nankai trough, the Sagami trough, the Japan trench and the Kurile trench (Sugimura and Uyeda 1973), corresponding to each their subduction systems. The Ryukyu trench is not included in Figure 2.2, but marks the western extension of the Nankai trough. The Izu-Bonin-Mariana trench divides two major subduction zones with highly differing characteristics: the Japan trench and the Nankai trough subduction zones (Sugimura and Uyeda 1973). The deepest parts of the trench formed where the Pacific plate subducts below northeastern Japan lies just over 8.4 km below sea level. In contrast, the maximum depth of the trough formed by the subduction of the Philippine plate below southwestern Japan is around 5 km below the sea level (Sugimura and Uyeda 1973). This large variation in trench depth is partly due to differing amounts of sediments on the plate interface (Sugimura and Uyeda 1973).

The differences between these two subduction zones is closely related to the age of the descending plates. The Philippine plate was created during a spreading episode

of the backarc region of the Izu-Bonin-Mariana arc between 26-15 Ma, forming the Shikoku basin (Okino, Shimakawa, and Nagaoka 1994). It is therefore much younger than the neighboring Pacific plate of approximately 140 Ma (Müller et al. 2008 as cited by Liu et al. 2017). This age is clearly reflected in the differing dip angle of the two subducting plates, which is also implied in Figure 2.2. The locked region of the plate interface in the Japan trench dips at around 27° (Kanamori 1971) and at intermediate depths the dip increases to 40° (Seiya Uyeda and Kanamori 1979), while the Nankai trough has a maximum dip of 11° down to 30 km depths along the plate interface (Nakanishi, N. Takahashi, Park, et al. 2002). Furthermore, the Japan trench subduction zone is non-accretionary (Tsuji, Juichiro Ashi, et al. 2015), while the Nankai trough has a prime example of an accretionary prism (Raimbourg et al. 2014).

Due to the different characteristics of the subduction zones, the main islands of Japan have a varying geological framework (Hashimoto 1991). Where the northeast Honshu island has large variation in onshore geology, the southwest Honshu island has distinct belts of similar geology that stretch across the whole island, parallel to the subduction axis (Sugimura and Uyeda 1973). This makes it easier to track the geological history of southwestern Japan, particularly in studying the evolution of the island arc crust, forearc basins and accretionary prism formation (Asahiko Taira 2001).

2.2.2 The Nankai trough subduction zone

Within the Nankai trough, the Philippine plate subducts below the Amur plate at a rate of 2-4 cm/yr in a northwestern direction (Seno, Seth Stein, and Gripp 1993). The low dip angle of the Philippine plate allows for a large area of coupling on the interface (Ruff and Kanamori 1983), and therefore a large fault area available for rupture during a coseismic event. The Philippine plate brings an approximately 1500 m thick sediment section into the Nankai trough from the Shikoku basin (Sugimura and Uyeda 1973), which leads to a significantly shallower trench area than the surrounding subduction zones.

The large influx of sediments into the accretionary prism is in part from Shikoku basin sediments on the Philippine plate, and drainage from the Suruga trough to the east (Jun'ichirō Ashi, Timothy Byrne, and Asahiko Taira 1992). The subduction angle of the descending plate varies across the Nankai trough due to the difference in age, topography and sediment thickness of the Shikoku basin (Ike et al. 2008; Nakanishi, N. Takahashi, Yamamoto, et al. 2018). Figure 2.3 shows depth contours for the descending Philippine plate within the subduction system, as defined by Nakanishi, N. Takahashi, Yamamoto, et al. 2018.

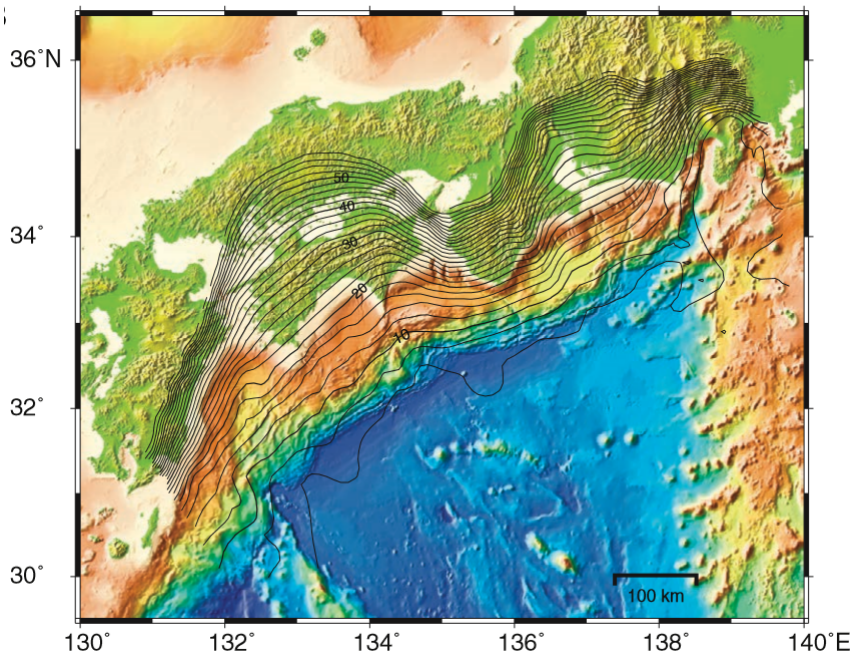

Figure 2.3: Depth contour map of the Philippine plate subducting below the Amur plate. Contour are indicated for every 2 km. (Source: Nakanishi, N. Takahashi, Yamamoto, et al. (2018))

The dip increases to the east and west, where the oldest sections of the Philippine crust subducts. This is specifically seen below the Kii Peninsula, where a significant increase in dip angle is observed, which is apparent in Figure 2.3. This increase may be related to a subducted ridge on the surface of the Philippine plate (Park et al. 2004). The existence of this subducted ridge is important to note, as they are proposed to be closely related to earthquake processes (Ding and Lin 2016). Ridges can affect the geometry and hydrology of the fault, therefore affecting the locations of earthquakes within (Ding and Lin 2016). This will be discussed in more detail in Section 2.3.

Considering the geological belts present on the southwest Honshu and Shikoku islands, the Shimanto belt is of particular interest in this project. This belt represents the ancient accretionary prism from the Cretaceous to Tertiary period (Taira, H. Okada, et al. 1982). Taira, H. Okada, et al. (1982) conducted an extensive study of the exhumed Shimanto belt on the coast of Shikoku island, revealing details of the structure within. Examining these rock formations can give an idea of the buried parts of the belt that are difficult to constrain through seismic imaging (Kodaira, N. Takahashi, et al. 2000). The Shimanto belt will be important when discussing the structure of the geological model in Chapter 4.2.

Through the Nankai Trough Seismogenic Zone Experiment (NanTroSEIZE) project,

the International Ocean Discovery Program (IODP), have conducted several drilling expeditions in the accretionary prism (JAMSTEC 2019a). These expeditions have contributed to a detailed understanding of the structure of the accreted sediments (Tsuji, Juichiro Ashi, et al. 2015). The décollement in this region lies between the accretionary prism sediments and the underthrust lower Shikoku basin sediments, some hundred meters above the oceanic crust (Kodaira, Kurashimo, et al. 2002). Near the trough, the décollement is relatively shallow and therefore possible to study through the NanTroSEIZE expeditions (Taira, Hill, et al. 1992), while the deeper regions are less accessible. Studying basal shear zones within exhumed Shimanto belt sections can give an insight into the future development of the accretionary prism (Taira, Hill, et al. 1992).

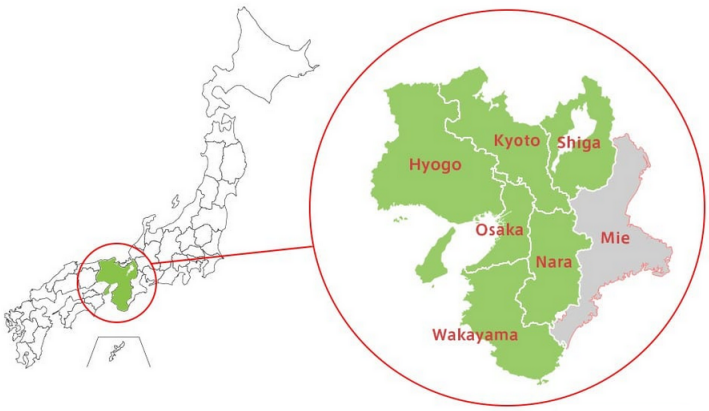

Figure 2.4: Location of the Kii Peninsula in Japan, including prefectures within the Kansai/Kinki region. (Source translated by: Radford (2016))

The area chosen for the gravity modelling covers the Kii Peninsula, shown in Figure 2.4. The forearc region here will be the focus of the forward modelling. The Kii Peninsula lies within the Kinki region of southwest Honshu island. Figure 2.4 shows the Kansai region in green. The Mie prefecture is not included in the Kansai region, however it is included in the Kinki region which covers the Kansai region and the Mie prefecture. Directly seaward of the peninsula lies the Kumano basin, below which the 1944 Tonankai earthquake took place on the plate interface (Ando 1975). This basin is bordered by outer ridges keeping a nearly 2 km thick layer of sediments within (Screaton et al. 2009).

Following the ridge is the accretionary prism and the frontal thrust zone. This complex fault zone is illustrated in Figure 2.5. Extensive faulting occurs within the accretionary prism, and the megathrust fault branches out into a splay fault and out-of-sequence thrust faults (Gaku Kimura, Kitamura, et al. 2007), which are labeled

as the *Megasplay fault zone* in the figure. The in-sequence faults are likely formed by compression in the forearc, and uplifted through the underthrusting of sediments (Daniel E Karig 1974). As more sediments are accreted, the faults develop a nearly vertical dip angle (Kearey, Klepeis, and Vine 2009).

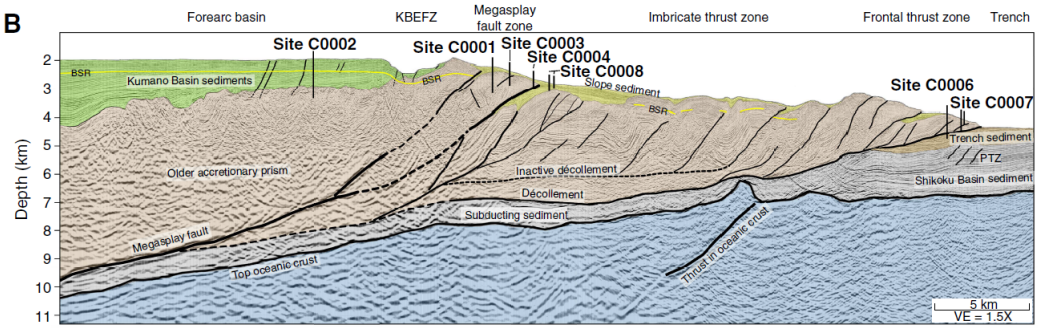

Figure 2.5: Structure of the accretionary prism off the Kii Peninsula. Locations of IODP drill sites are indicated by solid black lines on the surface labeled C0001-C0008. Black lines within the structure indicate faults, and fault zones are labeled. (Source: Screaton et al. (2009))

Below the zone of out-of-sequence thrust faults, the décollement connects, or steps down from the top of an underthrust sediment section, reaching the basement of the oceanic plate (Gaku Kimura, Kitamura, et al. 2007). This, along with the out-of-sequence thrust faults, marks the transition zone between the outer wedge and the inner wedge, a division of the Nankai accretionary prism defined by Gaku Kimura, Kitamura, et al. (2007). This transition zone marks the approximate up-dip edge of the fault zone involved in megathrust earthquakes (Gaku Kimura, Kitamura, et al. 2007), an area recognized by a distinct change in physical and geological properties compared to the seismogenic region (J. C. Moore and D. Saffer 2001). Of particular interest is variations in hydrological properties of this limit. Several processes, such a metamorphic dehydration of minerals or compression of porous rocks, may create increased pore pressures in this region (J. C. Moore and D. Saffer 2001).

An incoming sediment section with greater thickness than 1.5 km is observed in the trough off the Kii Peninsula (Ike et al. 2008). The Shikoku basin sediment sections are rich in sandy sediments (J. C. Moore and Daniel E Karig 1976); Ike et al. 2008). Dewatering of these sediments, along with bathymetric variations in the basement keeping the sediment sections within, may lead to trapping of fluid and in turn excess pore pressures (Ike et al. 2008). Increase in pore pressures has been linked to earthquake activity, and the process of this will be discussed more closely in the next section.

2.3 Earthquake activity

As mentioned at the start of this chapter, subduction zones are prone to large, often devastating earthquakes. In addition to these large scale earthquakes, a smaller, less easily detectable type of earthquake has been observed and termed slow earthquakes (Sacks et al. 1978). This section will go into further detail on where different earthquakes occur in subduction zones, which processes contribute to the accumulation and release of their seismic energy, and characteristics of different types of slow earthquakes.

2.3.1 Earthquakes in subduction zones

Within a subduction system, several major processes are at work. The forces are highly driven by gravity and resistive traction (Engelder and Price 1993). The resistive forces act either as friction between two plates or between the lithosphere and the underlying asthenosphere, referred to as mantle drag (Engelder and Price 1993). The main driving forces within the subduction system are slab pull, ridge push and suction. Slab pull is created by a strong gravitational pull on the dense oceanic lithosphere (Engelder and Price 1993). Ridge push occurs near spreading ridges, causing a force on the entire plate in the direction of spreading (Engelder and Price 1993). Suction refers to the force that occurs in the trench between the two plates, especially if irregularities on the plate are subducted causing a space between the overriding and subducting plate (Engelder and Price 1993). These forces may in turn cause friction between the plates (Kanamori 1971). Along with thermal, hydrological and geological variations, these forces contribute to stress accumulation within the subduction zone (Engelder and Price 1993), leading to fracture and faulting in the lithosphere.

Faults behave in a stick-slip pattern (Stein, Wysession, and Houston 2003). This implies that friction on the fault plane causes locking between the footwall and the hanging wall of the fault. When the stress builds up to exceed this friction, the fault will slip and result in an earthquake (Engelder and Price 1993). During this slip, a drop in stress can be measured, relating to the size of the earthquake (Engelder and Price 1993). How much stress is needed to cause slip on the fault plane depends on the strength of plane, or the sliding friction (Stein, Wysession, and Houston 2003). The Coulomb-Mohr failure criterion relates the amount of shear stress relative to normal stress that is necessary for a rock to fracture (Stein, Wysession, and Houston 2003). Fracturing of rock is analogous to slip on a fault plane, though failure here is related to the sliding friction on the fault plane rather than internal friction of the material (Stein, Wysession, and Houston 2003). The Coulomb-Mohr criterion for slip to occur on a fault is given by:

$$\tau = -\mu\sigma$$

Where τ is the shear stress, μ is the frictional coefficient and σ is the normal stress (Stein, Wysession, and Houston 2003). The equation implies that the shear stress must be at least equal to the product of the frictional strength and the normal stress in order to cause slip on the fault plane, while applying stress in the opposite direction of the frictional resistive force (Engelder and Price 1993). Reduction of either friction or normal stress will lead to fault rupture from a lower shear stress, which is important when discussing earthquake rupture in weak sections of subduction zones.

An important control on earthquake occurrence is the existence of fluids within fault rocks and the fault plane (Engelder and Price 1993). During metamorphic dehydration, released fluid may be trapped by impermeable rocks or sediment sections nearby (J. C. Moore and Vrolijk 1992; D. M. Saffer and Bekins 2006; Ike et al. 2008). The trapped fluid causes an increase in pore pressures within the rock, which in turn could have a large effect on the strength of the fault plane (Engelder and Price 1993). When pore pressures increase, the normal stress is reduced (Stein, Wysession, and Houston 2003). Following the Coulomb-Mohr criterion, this reduction in normal stress could lead to rupture along the fault.

Great forces between the crustal plates cause extensive faulting in several regions of the subduction system, both within the overriding and the descending plate (Engelder and Price 1993). Faults may form due to compression within the fore-arc region, along the surface of the descending plate, and within the subducted plate at various depths (Kearey, Klepeis, and Vine 2009). Hence, there are several areas within the subduction system available for earthquake generation. Figure 2.6 illustrates the five main regions.

At the surface, faults in region 1 and 2 usually generate small earthquakes (Stein, Wysession, and Houston 2003). Region 1 lies on the outer rise, where the bending of the crust causes faulting. Earthquakes in region 1 can also be caused by deep faulting, generally extending through the whole oceanic crust (Kanamori 1971). The earthquakes here usually exhibit a normal faulting mechanism (Kanamori 1971), and are often related to aftershocks following great interplate earthquakes (Raeesi and Atakan 2009). This outer-rise region can be under compression during the interseismic period close in time to the occurrence of megathrust earthquakes, leading to reverse a faulting mechanism. In other words, this compressional process, causing reverse faulting during the interseismic period, is reversed as tensile stress is released during a megathrust earthquake. This stress release therefore leads to normal faulting shortly after a megathrust earthquake (Raeesi and Atakan 2009). For accretionary margins, region 2 generally includes reverse, thrust and splay faults within the consolidated sediment sections (J. C. Moore and Vrolijk 1992). This region will be discussed further in the next section.

Varying frictional properties between the two plates cause earthquakes in region 3, within the major thrust fault on the plate interface (Stein, Wysession, and

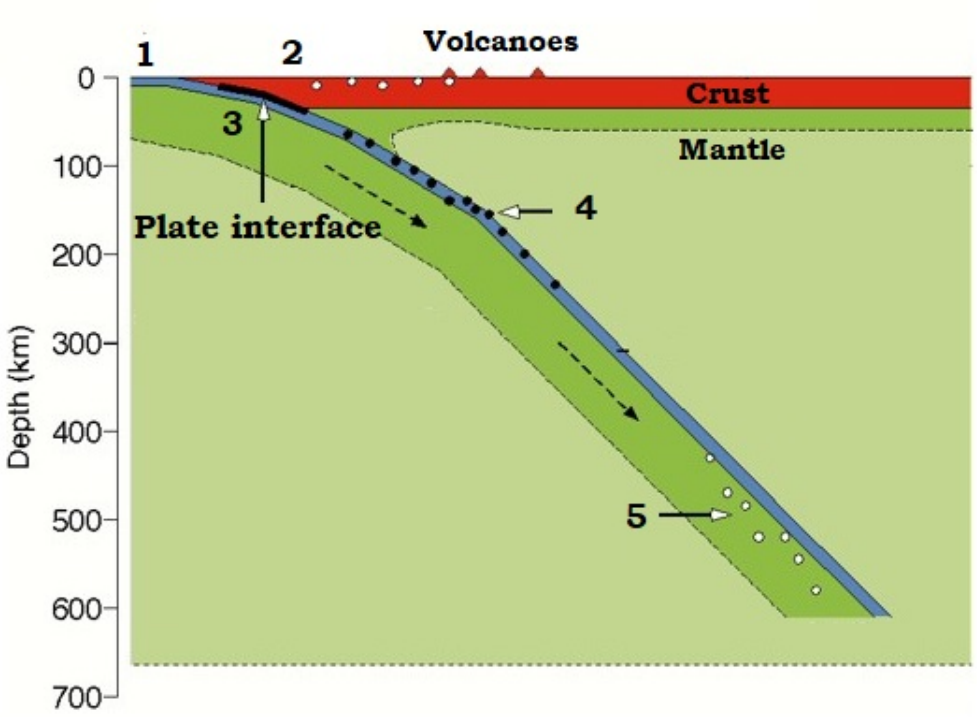

Figure 2.6: Illustration of regions within the subduction zone where earthquakes occur. 1: Outer rise, 2: forearc, 3: plate interface, 4: intermediate depths on descending plate, 5: deep region of descending plate.

Houston 2003). The seismogenic zone is locked during interseismic periods (Ruff and Kanamori 1983), on strong patches on the interface, referred to as asperities (Kanamori 1971). The distribution of asperities are controlled by frictional and bathymetric variations between the plates (Lay and Kanamori 1981), and provide an important control on earthquake size and location. Stress accumulates on the asperities as steady slip occurs on the rest of the plate interface (Lay and Kanamori 1981). This stress is then released, either by large interface earthquakes, or through slow earthquakes (Lay and Kanamori 1981; Sacks et al. 1978). The size of the earthquake then depends on the size of the asperity.

Below the accretionary prism, the plate interface is thought to slip aseismically, likely due to sediments on the interface and high pore pressures within them (D. E. Byrne, D. M. Davis, and Sykes 1988). The seismogenic zone generally begins where the subducting plate comes in contact with the overriding solid crust (Nakanishi, Kodaira, Park, et al. 2002). At depths below 40 km, most subduction zones appear to be uncoupled at the interface (Ruff and Kanamori 1983), confining the seismogenic zone to the up-dip region from this depth. Slow earthquakes have also been observed on the transition between the locked and unlocked zone at these depths (See Beroza and Ide 2011, and the references therein).

Region 4 and 5 comprise the intermediate and deep zones, within which the Wadati-Benioff zone is found, where extensive earthquake activity is documented in subduction zones (Stein, Wysession, and Houston 2003). Earthquakes in this region likely occur due to internal deformation of the plate (Kearey, Klepeis, and Vine 2009). Studies have suggested the existence of high pore pressures in this area, likely due to serpentinized mantle being dehydrated at the high temperatures and depth of this area (Kearey, Klepeis, and Vine 2009). The increase in pore pressure may cause brittle failure within the descending crust, and this process is referred to as dehydration embrittlement (Kearey, Klepeis, and Vine 2009). However, the exact process leading to this dehydration embrittlement is not well constrained (Barcheck et al. 2012).

The regions of most importance in this thesis are regions 2 and 3, and specifically the relation between earthquakes within them. The size of asperities on the plate interface are related to the size of the corresponding earthquake (Kanamori 1971). Therefore, locating and quantifying these asperities is an important part of explaining the earthquake activity in subduction zones, and relating them to future earthquakes. A better understanding of the rate of stress accumulation and release within the major subduction zone faults could be obtained by determining the asperity distribution within the subduction zone. As stress is also released through slow earthquakes, understanding the processes behind them may be a key factor in determining the rupture process of future earthquakes, or perhaps factors triggering earthquake generation (Beroza and Ide 2011). Obtaining more information on shallow slow earthquakes and their fault rupture extents may also contribute to locating asperities in the shallow regions of the subduction zone.

2.3.2 Slow earthquakes

The existence of slow earthquakes was first discussed during the 1970's. In particular, a study by Kanamori and Cipar (1974) suggested that an aseismic slow slip event in the Chilean subduction zone could be a precursor to the massive 1960 Chilean earthquake of magnitude M_w 9.5 (Lomnitz 2004). Kanamori and Cipar (1974) proposed a model where deep slip below the seismogenic zone increases the accumulation of stress on the interseismically locked zone above, until the frictional strength of the fault is exceeded, causing a massive earthquake. Following this, Lay and Kanamori (1981) introduced the asperity model as a means of describing the occurrence of these earthquakes. The model is based on the theory of stress accumulation on asperities, and implies that once one asperity has ruptured, loading is applied to other asperities in its vicinity, increasing the stress on these as well (Lay and Kanamori 1981). Therefore, if several asperities are located close to each other, one event can trigger others.

The asperity model has been used to discuss the distribution of deep slow earth-

quakes (Y. Ito, Obara, et al. 2007), illustrated in Figure 2.7. If a small asperity ruptures, it could trigger nearby asperities and from there clusters of earthquakes with low-frequency or slow slip are triggered by each other and can occur simultaneously (Y. Ito, Obara, et al. 2007). The asperity model opened up for a new perception of subduction zone earthquakes, and an increased interest in the study of these slow events and their implications for future large earthquakes (Y. Ito, Obara, et al. 2007).

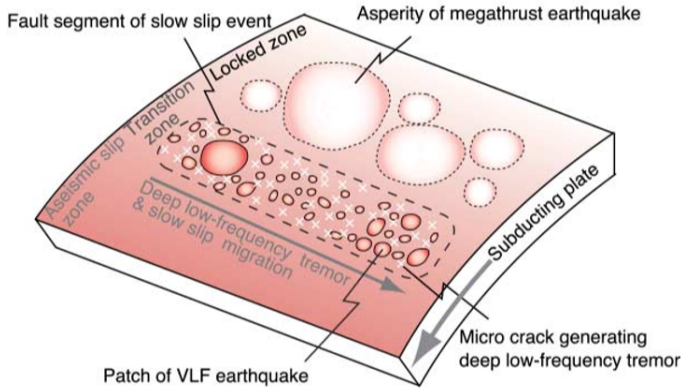

Figure 2.7: Illustration of the asperity model for deep regions of a subduction zone. The large patches indicate large asperities on which megathrust earthquakes occur. The smaller patches are asperities assumed to trigger slow earthquakes, or very low-frequency earthquakes (indicated as "VLF earthquakes" in the model). The model indicates micro cracks in the fault plane, linking them to the generation of low-frequency tremors. Y. Ito, Obara, et al. (2007) define the transition zone as the area between the interseismically locked zone above and the area where steady slip occurs along the plate interface. (Source: Y. Ito, Obara, et al. (2007)).

Numerous studies have been conducted on slow earthquakes in major boundary fault zones, particularly in subduction zones and transform plate boundaries. They have been detected in several subduction zones, such as Cascadia off western North America, Hikurangi in New Zealand and Nankai (Beroza and Ide 2011; Rogers and Dragert 2003; Douglas et al. 2005), as well as in the San Andreas transform fault (Nadeau and Dolenc 2005). Generally, slow earthquakes have been detected in regions 2 and 3, occurring along the interface both above and below the seismogenic zone (Beroza and Ide 2011). However, different studies have used different names for the same or similar events. Therefore, before discussing the actual earthquakes further, it is necessary to give an overview of the types of events that fall under the category of 'slow' earthquakes and the naming conventions that will be used in this thesis.

Slow earthquakes are generally divided into four main categories: slow slip events (SSE) (Obara, Hirose, et al. 2004), low-frequency tremors (LFT), sometimes referred to as nonvolcanic tremors (Obara 2002), low-frequency earthquakes (LFE) (Katsumata and Kamaya 2003) and very-low-frequency earthquakes (VLFE) (Obara and Y. Ito 2005). LFEs and VLFEs, as the names suggest, are earthquakes with lower

dominant frequencies than regular earthquakes (Beroza and Ide 2011). Dominant frequencies lie within $1-8Hz$ for LFEs (Ide et al. 2007) and around 0.02-0.05 Hz for VLFEs (Y. Ito, Obara, et al. 2007). Seafloor observations have showed that VLFEs can also be rich in high-frequency signals (Sugioka et al. 2012), and these signals were likely not previously observed at onshore stations due to attenuation of the higher frequency signals. Therefore, although the name implies that they only give off low frequency signals, this is not entirely correct. Dominant frequencies of the LFT signals lie between 1-10 Hz (Obara 2002). Contrary to this, typical frequencies of small earthquakes are around 10-20 Hz (Obara 2002). The events are therefore difficult to constrain using regular seismometers, which are set to detect higher frequency regular earthquakes. Some slow earthquakes can only be constrained using GPS measurements, as they usually give off few and very-low frequency seismic signals which might be difficult to distinguish from background noise (Beroza and Ide 2011).

A distinction needs to be made between SSEs, silent slip and aseismic slip. SSEs are defined as earthquakes that take significantly longer time to rupture the fault plane than ordinary earthquakes (Beroza and Ide 2011). SSEs give off seismic signals to some scale, though they may be difficult to detect through the seismic background noise. Aseismic slip is caused by creep on the interface rather than stick-slip behavior (D. M. Saffer and Wallace 2015), whereas silent slip may be caused by a combination of the two processes (D. M. Saffer and Wallace 2015).

The studies conducted in the Nankai trough subduction zone generally use the naming convention discussed above for slow earthquakes, while studies in the Cascadia subduction zone discuss a related phenomena: Episodic tremor and slip (ETS) (Rogers and Dragert 2003). Rogers and Dragert (2003) observed that slow slip episodes in the Cascadia subduction zone were often accompanied by tremors. Similar phenomena have also been related in the deep portions of the plate interface of the Nankai trough megathrust (Obara, Hirose, et al. 2004; Y. Ito, Obara, et al. 2007).

The characteristics of slow earthquakes vary with location on the plate interface. Deep events occur below the seismogenic zone, and typically follow a band or certain patches along the plate boundary (Audet et al. 2010; Beroza and Ide 2011). These events typically occur at depths of 30-40 km on the plate (Beroza and Ide 2011). Shallow slow earthquakes, however, occur more sporadically and often in clusters within particular areas near the trench, and are likely related to deformation of the accretionary prism (Beroza and Ide 2011). Due to the low resolution of these events at onshore seismic stations (Masaru Nakano, Hori, et al. 2018) and geodetic measurements both onshore and offshore near the trench (Hirai and Sagiya 2013; Yokota et al. 2016), shallow events are more difficult to study and confine.

Tremors are usually associated with volcanic activity, due to changes in hydrother-

mal properties or degassing in the magma chamber or conduit, evidently causing volume expansion (Chouet 1996). Even though the tremors occur in a slightly different setting in subduction zones, they are likely controlled by similar processes (Obara 2002), such as fluid within fault rocks (Schwartz and Rokosky 2007). The LFTs are therefore thought to be caused by crack propagation in the fault rocks due to an increase of pore pressures (Obara 2002). Shelly et al. (2006) proposed that increased pore pressures leading to slip on a fault could cause pressure release from the trapped fluid, which could explain the occurrence of these tremor episodes occurring in relation to SSEs and VLFEs.

Similar to regular earthquakes, slow earthquakes occur due to stick-slip mechanisms on a fault plane (Beroza and Ide 2011). Y. Ito, Obara, et al. 2007 proposed a mechanism for the coincidence of SSEs, LFTs and LFEs, relating to the previously discussed asperity model. Within the transition zone between the seismogenic and aseismic plate interface, small asperities are located within otherwise aseismic regions. As pore pressures increase, exceeding the strength of individual asperities, slip occurs. The stress increase causes generation of micro cracks on the interface, causing tremors, and slip migrates across the interface. This model could possibly explain why these events often occur simultaneously (Y. Ito, Obara, et al. 2007).

As slow earthquakes are relatively small, they also have a low stress drop (Y. Ito and Obara 2006). Y. Ito and Obara (2006) estimated that stress drops from shallow VLFEs off the Kii Peninsula were around 0.1 - 1% of the stress drop measured due to regular earthquakes. This low stress drop implies that the fault patches accumulate less stress before they rupture. Hence, slow earthquakes can be used to evaluate the amount of stress accumulated near the trough (Obara and A. Kato 2016). This highlights the impact these earthquakes could have on understanding the state of stress in a subduction zone.

2.3.3 Nankai trough earthquake activity

Throughout history, large earthquakes have occurred in the Nankai trough with recurrence intervals of approximately 100-200 years (Linde and Sacks 2002), and events have been dated as far back as year 684 AD (Ando 1975). The earthquakes are typically of M_w 8, showing low angle thrust mechanisms in the same direction as the plate convergence (Ando 1975). Rupture history at the Nankai trough either occurs as one event encompassing nearly the entire fault region, or as two events closely spaced in time, rupturing segments of the megathrust fault (Satake 2015). The last major earthquakes happened in 1944 in the Tonankai region and in 1946 in the Nankai region, following this historical pattern.

The megathrust earthquakes in these regions usually generate large tsunamis, causing massive destruction to the nearby Shikoku and Honshu islands (Satake 2015).

The likelihood of a new great earthquake in this region therefore increases the importance of extensive monitoring of the subduction zone. A splay fault was observed within the Tonankai rupture area (Park et al. 2004), which reaches the surface of the accretionary prism. This fault could possibly have contributed to the tsunami during the 1944 earthquake (Park et al. 2004).

R. E. Wells et al. (2003) discuss a possible link between basin locations in forearc regions and asperities on the interface. The basins could be a product of subsidence during the cycles of earthquakes throughout history (R. E. Wells et al. 2003; Nakanishi, N. Takahashi, Park, et al. 2002). The theory is consistent with locations of basins coinciding with seismogenic regions of the Nankai trough (Ando 1975). To describe historical megathrust earthquakes, the fault regions have generally been divided into separate segments. Ando (1975) introduced this model, by dividing the Nankai trough forearc region in four segments from A-D. The segments cover the regions from Shikoku island to the eastern Tokai region, the eastward limit of the Nankai subduction zone. The location of the segments are shown in Figure 2.8, together with the location of the Tonankai earthquake and the DONET network covering parts of the Nankai trough.

The Tonankai earthquake occurred on December 7., 1944 off the Kii peninsula, with a magnitude of around 8 (Kanamori 1972b). The epicenter was located on the coast of the Kii Peninsula, illustrated by the star in Figure 2.8. The earthquake occurred within the megathrust fault at a depth of 30 km, with an estimated slip of 3.1 m on the plate interface, along a fault area of 80×120 km^2 (Kanamori 1972b).

Other recent earthquakes off the Kii Peninsula occurred on September 5., 2004 near the trough and April 1., 2016, off the Mie prefecture. The 2016 earthquake was located near the updip limit of the seismogenic region, and had a magnitude of M_w6 (Tsuji, Minato, et al. 2017). The 2004 event consisted of a foreshock of $M_w7.1$, followed by the mainshock of $M_w7.4$, within a reverse fault at the outer rise (Saito, Satake, and Furumura 2010). Both of the 2004 earthquakes produced tsunamis that were measurable at GPS buoys nearby (T. Kato et al. 2005), and the maximum local run-up height was 4.6 m at the Mie prefecture (Koike et al. 2005). The fault slip of the main shock was estimated to 1.32 m, on a fault with an approximate size of 70×32 km^2 (Saito, Satake, and Furumura 2010).

Several studies have linked shallow slow earthquakes to regular earthquakes in the Nankai trough (Obara and Y. Ito 2005; Araki et al. 2017; To et al. 2015). Obara and Y. Ito (2005) observed VLFE activity in the shallow Nankai trough after the 2004 earthquakes, coinciding well with locations of aftershocks of the event. Araki et al. (2017) linked SSE activity between 2011 to 2016 with the off-Mie earthquake and the 2011 Tohoku earthquake, considering pore pressure changes in the accretionary prism following the earthquakes. SSEs with slips between 1-4 cm were detected through these pressure changes (Araki et al. 2017). Another cluster of VLFE events

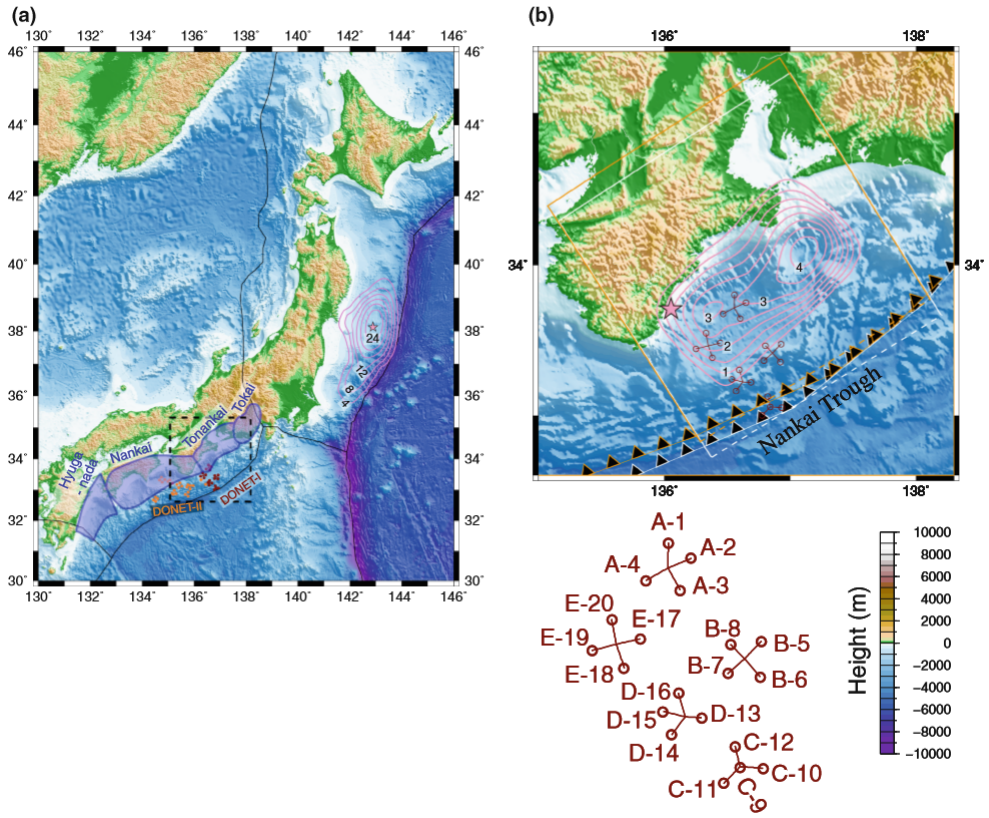

Figure 2.8: Locations of fault segments and DONET observatories within the Nankai trough. a) Fault segmentation of the Nankai trough, similar to that proposed by Ando (1975). The black rectangle indicates the area of interest above the Kii Peninsula. The fault rupture caused by the 2011 Tohoku earthquake is indicated along the Japan trench, where a star marks the epicenter of the earthquake. Both the DONET1 and DONET2 network are shown within the Tonankai and Nankai fault segments, respectively. b) Location of the fault segment involved in the 1944 Tonankai earthquake, along with locations of DONET1 observatories above the accretionary prism and Kumano basin. The star indicates the epicenter of the earthquake. The DONET1 network is indicated by circles in the map. The network is highlighted below the map, labeled with names of observatories corresponding to the A-E science nodes. (Source: Ariyoshi et al. (2014))

followed the 2016 off-Mie earthquake, starting as aftershocks and lasted for up to 17 days after the event (Masaru Nakano, Hori, et al. 2018). Masaru Nakano, Hori, et al. (2018) also noted the occurrence of a M_w7 earthquake in Kyushu island in the western Nankai trough on April 16., 2016, possibly triggering more VLFEs in this period. However, other episodes have occurred with no triggering event, such as in 2009 (Sugioka et al. 2012), suggesting that a triggering earthquake is not necessary for slow earthquakes to occur (Masaru Nakano, Hori, et al. 2018).

Shallow slow earthquakes have also been found to share common source regions and mechanisms with tsunami earthquakes (Sugioka et al. 2012), a type of earthquake that causes unusually large tsunamis compared to the size of the earthquake (Kanamori 1972a). It would therefore be beneficial to get a better understanding of

the relation between slow earthquakes and regular earthquakes, especially in evaluating the possibility for tsunami generation near the trough (Sugioka et al. 2012).

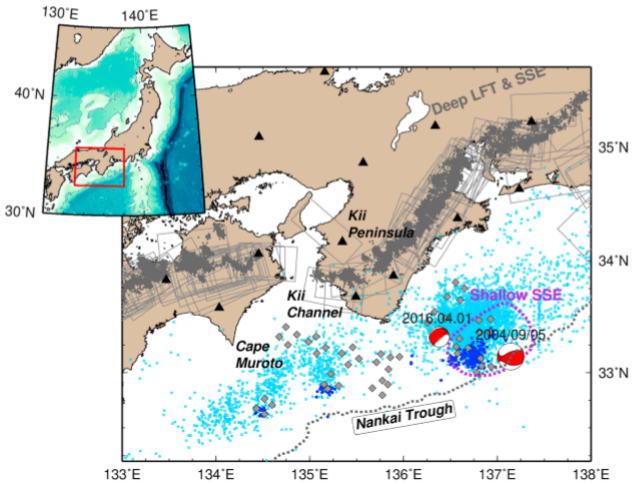

Figure 2.9: Location of slow earthquakes off Kii Peninsula and southwest Shikoku island. The inset indicates the location of the area amongst the Japanese islands. The gray dots represent deep LFTs and rectangles indicate locations of deep SSEs. The light blue dots are VLFE locations determined by onshore seismic stations, and the dark blue dots indicate locations of VLFEs determined by OBSs in the DONET network. The purple dashed line indicates locations of shallow SSEs. The focal spheres for the 2004 and 2016 earthquakes are represented and labeled. Location of all the DONET observatories are indicated by gray diamonds, and the onshore F-net stations are indicated by black triangles. (Source: Takemura, Matsuzawa, Noda, et al. (2019))

Figure 2.9 indicates locations of slow earthquake activity within both the deep and shallow region of the Nankai trough. The locations of deep slow earthquakes have been well constrained by onshore stations (Obara 2002). The Hi-net network, containing sensitive seismometers and tiltmeters, and the F-net network of broadband seismometers are able to detect earthquakes with lower frequencies on the plate interface below the Kii Peninsula (Obara 2002). As Figure 2.9 shows, they are generally observed along a band near the 30-35 km surface depth of the descending Philippine plate (Y. Ito, Obara, et al. 2007). Within this region, LFTs, LFEs and SSEs have been observed simultaneously (Y. Ito, Obara, et al. 2007).

Shallow slow earthquakes are more difficult to place accurately than their deep counterparts. However, the accuracy in their location has been improved following the installment of the DONET network above the source region (Masaru Nakano, Nakamura, et al. 2013). Even though seismic signals of VLFEs can be detected using DONET observatories, the SSEs still remain difficult to confine (Masaru Nakano, Hori, et al. 2018). Studies have suggested a link between tremors and VLFEs in the accretionary prism, and that tremor migration along faults could be a result of SSEs, allowing this tremor activity to reflect distribution of SSEs (Yamashita et al. 2015). SSEs can also be detected through pressure sensors, as their occurrence is sensitive to pore pressure variations (Araki et al. 2017). Recent studies of the shallow

VLFE activity at the Nankai trough has placed the events within faults along the décollement (Sugioka et al. 2012; Masaru Nakano, Hori, et al. 2018).

Within the Nankai trough, extensive research supports the theory of fluids being of importance for slow earthquake generation (Shelly et al. 2006; Kodaira, Iidaka, et al. 2004; Araki et al. 2017). Results indicate that higher pore pressures are present both in the deep and shallow regions of slow earthquakes. Through the DONET network, several zones of low seismic velocities have been found near the prism toe (Tonegawa et al. 2017), indicating increased fluids within the prism, below the observatories. The sources of fluids here might be due to dehydration of clay minerals at certain depths (J. C. Moore and D. Saffer 2001).

In addition to increased fluid migration along the faults, clay minerals on the fault plane may weaken the frictional strength (Brown et al. 2003). The weakened fault would then require less stress to cause rupture along the fault plane, which is reflected in the low stress-drop observed from these events. The subducted ridge off the Kii Peninsula also corresponds well with locations of shallow tremors and VLFEs (Park et al. 2004; Yokota et al. 2016). Following the discussion that high pore pressures may arise when water saturated sediments are compressed within regions of impermeable structures, these sea mounts may contribute to trapping of the migrating fluid. Therefore, a combination of increased fluid migration and impermeable structures could likely control locations of slow earthquakes in the accretionary prism. The shallow events align well with the updip limit of the Tonankai rupture area, within the accretionary prism (Takemura, Matsuzawa, Noda, et al. 2019). Changes in properties along the updip limit of the fault also play an important role.

Establishing weak zones within the Nankai trough megathrust would be valuable to better understand the fault extent of megathrust earthquakes here (Masaru Nakano, Nakamura, et al. 2013). Following the asperity model, deep slow earthquakes may increase the stress on the seismogenic fault. On the other end, shallow slow earthquakes may give valuable information of the state of stress within the shallow region of subduction zones. Obtaining a better understanding of the slow earthquakes and their relation to larger events could be crucial in predicting future earthquakes in the Nankai trough.

2.4 Gravity

Monitoring of subduction zone processes is important in determining when the next large earthquake could occur, as well as to determine processes leading up to an earthquake. To better understand the processes at work in subduction zones, and the mechanisms governing the size and distribution of both regular earthquakes and slow earthquakes, several different geophysical methods have been used. One such method is the study of Earths gravitational field.

2.4.1 Gravity measurements

Gravity surveys are extensively used in Earth research due to the low cost of surveys and the possibility of detecting vertical density variations in the subsurface, which can better constrain rock bodies of interest (Hinze, Von Frese, and Saad 2013; Jacoby and Smilde 2009). The aim of gravity surveying is to observe gravity anomalies - variations from the theoretical gravity field of the Earth (Hinze, Von Frese, and Saad 2013). This theoretical field is determined by the geoid, or the shape of the Earth reduced to mean sea level (Jacoby and Smilde 2009).

The acceleration felt at one point on the Earth is not only affected by the vertical pull, but from mass attraction in all directions. For instance, a mountain beside the measuring station will exert a vertical force on the instrument, slightly reducing the actual signal (Mussett and Khan 2000). Variations in Earth tides must also be accounted for, and the latitude of the measurement station (Mussett and Khan 2000). Therefore, when measuring gravity, several corrections must be applied before the values can be interpreted (Jacoby and Smilde 2009).

Which corrections apply to the measured gravity depends in part on the targeted anomaly, and the method of measurement. The effect of the bulging of the theoretical elliptical shape of the Earth is corrected for through the latitude correction (Mussett and Khan 2000). Lateral and vertical variations in topography must be accounted for through topographic corrections. These include the free-air correction, terrain correction and Bouguer corrections (Jacoby and Smilde 2009).

Topographic corrections account for when the measurement stations are placed at different elevations, and often in large scale surveys the reductions will place all measurements at the sea level (Mussett and Khan 2000). For instance, when conducting an airborne gravimetric survey, or analyzing GRACE data, a correction must be applied to account for the height above the reference, which is often chosen as the sea level. The free-air correction accounts for differences in height between measurements stations and the reference geoid, without accounting for the mass between the stations (Jacoby and Smilde 2009). Terrain correction removes the effect of basins or mountains near the measurement station, which may shadow the signal from the subsurface body of interest (Mussett and Khan 2000).

The Bouguer correction is generally applied to remove the effect of large bodies of water below the measurement station (Jacoby and Smilde 2009). This correction fills in oceans with crust to account for missing crustal layers here, thereby revealing anomalies that may be masked by the ocean layer. Through the Bouguer correction, the Bouguer plate of known thickness and infinite length is used to approximate gravity variations from the theoretical gravity field of the Earth at a given measurement station (Jacoby and Smilde 2009). After applying the different corrections to the measured gravity, lateral density variations are seen in the reduced gravity, and

thus gravity anomalies can be observed. If all these corrections are applied to the measured gravity, the Bouguer anomaly is obtained (Mussett and Khan 2000).

2.4.2 Gravity instrumentation

A gravimeter is used to measure gravity values (Jacoby and Smilde 2009). The most common gravimeter uses a mass attached to a spring to measure variations in the length of the spring (Jacoby and Smilde 2009). As the gravimeter is placed over the anomaly, the spring will have a measurable displacement due to the attraction of the anomaly, which is comparable to areas without the anomaly. Extensive measurements above this anomaly will then be able to constrain its placement, and the measurements can be used to interpret the shape and depth of the body (Mussett and Khan 2000). A temperature regulation system within the gravimeter is needed to make sure the spring is not affected by thermal variations.

Gravity surveys can be conducted using absolute or relative gravimeters. An absolute gravimeter measures absolute gravity values at a measuring station (Jacoby and Smilde 2009). In an absolute gravity survey, the total gravity at a point is measured. Often, an absolute gravimeter is stationary and uses lasers and accurate clocks in the instrument to measure the acceleration of a mass in free fall (Jacoby and Smilde 2009). In addition to surveying purposes, absolute gravity measurements can be used to calibrate relative gravimeters (Remy Agersborg et al. 2017). This procedure involves measuring at two locations with known absolute gravity values, covering the approximate gravity range of the gravimeter, and repeating the measurements to obtain an uncertainty on the value of gravity measured (Remy Agersborg et al. 2017).

Seafloor gravity measurements use land gravimeters within a pressure casing. A gimbal system is placed within the pressure casing to level the instruments to be able to measure accurate vertical gravity acceleration (Remy Agersborg et al. 2017; Zumberge et al. 2008). Uncertainties governing the precision are instrumental drift, changes in scale factor of the instrument, deviations from theoretical tides and actual tides and deviations in the tilt of the instrument (Jacoby and Smilde 2009).

During a survey, measurements are repeated at stations several times to obtain good precision for the measured gravity values and to correct for instrumental drift (Mussett and Khan 2000). This drift is caused by variations in the spring as it might stretch during a survey, resulting in observed gravity change that results from the spring variation rather than actual anomalies (Jacoby and Smilde 2009). Base stations are therefore used to calibrate the instruments for drift variations during a survey (Zumberge et al. 2008). This concept will be discussed more in the next section.

2.4.3 Time-lapse gravity surveys

Through time-lapse gravity measurements, it is possible to monitor temporal changes in the gravity field due to density variations in the subsurface. The current use of time-lapse relative gravimetry at the seafloor is in monitoring density variations and subsidence within producing gas fields (Hugo Ruiz et al. 2016). The method has also been used to estimate densities and porosities of new crust at mid-ocean ridges (Pruis and Johnson 2002), and in measurements of vertical deformations on seafloor volcanoes (Ballu et al. 2009). How this method can be used for monitoring gravity variations caused by processes in the subduction zone will be described further in Section 2.4.4.

Relative gravimetry measures the gravity difference between measurement stations (Mussett and Khan 2000). In doing so, the absolute values of gravity acceleration are not of importance during the survey, only the difference between the stations. Through relative gravimetry, small variations within the subsurface can be accurately detected, and generally they can measure over a range of 8000 mGal (Remy Agersborg et al. 2017). To obtain accurate measurements with relative gravimetry, stations need to be placed either on a line or on a grid above the target section (Mussett and Khan 2000). Base stations need to be placed on areas where little to no changes are thought to occur between base surveys and time-lapse surveys, and throughout the survey time (Mussett and Khan 2000). This implies that significant knowledge on the subsurface must be known, such as the lateral extent of the anomaly that is to be detected.

For time-lapse surveys on the seafloor, concrete platforms (CPs) are placed along the seabed some time before a survey is conducted, to allow the CP to settle in the sediments. The CP allows for a stable surface to conduct measurements on, making it simpler to obtain high precision of the repeated measurements (Remy Agersborg et al. 2017). The CP also assures that measurements are taken at almost the exact same position during repeat visits to the same station.

Precision of seafloor gravity measurements can be of the order of 1 μGal (Remy Agersborg et al. 2017), relating to the obtained repeatability in the measured values at stations during a survey. Shipborne gravity measurements tend to have a precision of around 1 mGal (Tomoda 2010). Therefore, the precision of seafloor gravimetry is much higher than shipborne gravimetry, which improves the accuracy of the time-lapse gravity results obtained through seafloor gravity measurements as opposed to shiborne measurements. In addition to this, seafloor gravity surveys measure gravity in a more stable environment, reducing the errors of the measured values.

The accuracy of seafloor gravimetry is dependant on a few factors. The dominating uncertainty is the instrumental drift, which can cause variations over 10 μGal/day in measured gravity (Hugo Ruiz et al. 2016). The uncertainty caused by this drift is

corrected through the use of base stations, where an estimated drift can be obtained by repeated measurements at these locations where stable gravity is measured. Tidal variations can also cause larger variations in gravity. The uncertainty caused by the tidal variation can however be corrected for by using tide gauges deployed at various locations near CPs, to determine the contribution to the measured gravity from tides during a survey.

During a survey, the repeatability of measurements is determined. This indicates how well repeat measurements at a station can replicate the same measured gravity. The largest effect of the measurement precision is the vertical changes in seafloor depth, creating an uncertainty around 2 μGal/cm (Agersborg et al. 2017). This implies that a change of 1 cm in depth will lead to an approximately 2 μGal uncertainty in the gravity estimates. Therefore, monitoring of the subsidence of measurement stations is often done parallel to the gravity measurements, by using pressure sensors (Remy Agersborg et al. 2017). In addition to this, lateral contributions from gravity and tidal variations cause uncertainties in the measured values. These uncertainties are considered when interpreting the final processed gravimetry measurements.

Even though some considerations must be taken with uncertainties in the measured values, there are considerable benefits in conducting measurement along the seafloor rather than the other discussed surveying methods (e.g. shipborne, GRACE). An important benefit is that measurement stations are located closer to the target subsurface anomaly. The resolution of gravity is determined by how deep the anomaly is placed, as the effect from the subsurface body on the surface measurement station is reduced with increasing distance between them. Hence, the depth resolution is improved for seafloor measurements. In addition to this, the measuring environment is much more stable than for shipborne gravity, and less noise will be present in the gravity values.

2.4.4 Implications for subduction zone monitoring

Gravity measurements at various scales can give important information about subduction zone processes. Large-scale density variations can be caused by processes like compression, subsidence or uplift, and coseismic events. On smaller scales, fluid variations can cause observable density variations, which is of specific interest in this thesis. Some of these processes can be detected through real-time gravity surveying. Data from the GRACE satellite has for instance been used in determining deformation patterns prior to and during great subduction zone earthquakes (Panet et al. 2018). Furthermore, shipborne gravimetry is commonly collected during seismic surveys of the Nankai trough (Tomoda 2010; Fujiwara, Goto, and Kobayashi 1998). Through shipborne gravity measurements, a gravity change of 1 mGal was detected in the Japan trench one month prior to the 2011 Tohoku earthquake (Tsuboi and Nakamura 2013), highlighting the relevance of using gravity for earthquake monitor-

ing. Hence, gravity measurements can be used to detect density variations prior to or during subduction zone earthquakes.

In addition to satellite and shipborne gravimetric surveys, a network of superconducting gravimeteres are placed around Japan (Imanishi et al. 2004). The network measures continuously, and detected coseismic deformations during the 2004 earthquakes off the Kii Peninsula (Nawa et al. 2009). The Geological Society of Japan have put together the GALILEO gravity database to combine gravity data of Japan, allowing for extensive studies of different types of gravity maps over several areas of Japan (Miyakawa et al. 2015).

Of particular interest, gravity measurements can be used to detect asperities along the subducting plate interface (T.-R. A. Song and Simons 2003). T.-R. A. Song and Simons (2003) introduced the importance of measuring the trench-parallel gravity anomalies (TPGA) in subduction zones. They concluded that regions with strong negative TPGA were seismogenic, while the ones with strongly positive TPGA were aseismic. Regions with negative TPGA would correspond to basins within the subduction zone, which is consistent with the theory by R. E. Wells et al. (2003) on basins corresponding to seismogenic faults. Therefore, mapping the TPGA can give insight into where earthquakes occur on the interface (T.-R. A. Song and Simons 2003). Raeesi and Atakan (2009) introduce an extension of this, the trench parallel Bouguer anomaly (TPBA). TPBAs can give more information on the coupling along the plate interface as it reduces the gravity even more, revealing clearer anomalies after the reduction of other subsurface variations as discussed in Section 2.4.1.

As mentioned earlier, relative gravimetric surveys can detect variations in fluid properties within the subsurface rocks (Remy Agersborg et al. 2017), which has been beneficial in monitoring offshore gas reservoirs. Given the importance of varying fluid properties in the generation of earthquakes, relative gravimetry could be valuable in monitoring fluid processes in subduction zones. Considering the detectability of fluid variations through gravimetric measurements, the forward modelling conducted in this thesis will aim to model alterations in fluid flow within fault rocks in the Nankai trough.

Seafloor gravimetry has yet to be used for the purpose of monitoring subduction zone processes. Some challenges follow using this method on such a large scale geological feature. Determining base stations on such a dynamic area may be difficult, and the spacing of measurement stations must be large enough to cover the large deformation area. The lateral spacing of measurement stations above a subduction zone must therefore be larger than the spacing of stations above gas reservoirs.

The detected changes in the subsurface occurring within the subduction zone must be larger than the uncertainties to be able to interpret the results. Through relative seafloor gravimetry, it might be possible to detect small changes in fluid properties

within the subduction zone, particularly near the trough, where changes are assumed to occur at relatively shallow depths below the seafloor. Therefore, determining the feasibility of applying this method to study processes in the Nankai trough subduction zone is of great importance.

Chapter 3

Method

The aim of this thesis is to model temporal gravity changes in the Nankai trough subduction zone. Gravity modelling requires detailed information on the density distribution of the subsurface, and a source for assumed time-lapse gravity variations. Therefore, a density map is created as an input for the GravMod modelling tool (OCTIO Gravitude 2014). A procedure for the time-lapse gravity modelling is set up, following three scenarios. These scenarios involve locations of slow earthquakes and low degrees of coupling along the plate interface, assuming that fluid migration occurs within these regions. Hence, the time-lapse modelling variations are set up to model variations in fluid migration along fault planes or within the pore-space of rocks in the modelled region.

The methods described in this chapter first involve the creation of the density map. which will be used in the forward modelling of gravity. The densities are estimated based on a given 3D P-wave velocity model. The computations follow the wave equation for a homogeneous medium, and requires knowledge on the effective shear and bulk modulus of the medium. In addition to the effective moduli, a predefined velocity range is made, attempting to replicate layers of the velocity model. To determine the correct density mapping of the velocity model, a geological model is created, which will be discussed in detail in Chapter 4.2. This geological model consists of 12 layers, where the two first layers are defined as air and ocean water, and the other 10 are rock layers within the subsurface.

Once the density map is created, the estimated densities are discretized to a 3D distribution of rectangular prisms with given density values, which are used to compute the gravity potential on a grid of measurement points at defined depths in the model. In other words, the gravity potential at each point is computed based on the effect of this distribution of prisms. The total 3D distribution is used for a Bouguer anomaly computation, which are computed to validate the density map.

The time-lapse gravity modelling is conducted on specified groups of these prisms, following the three separate time-lapse scenarios.

The details of all the steps used in the gravity modelling will be presented in this chapter. First, the methods used to convert seismic velocities to densities will be shown, followed by the computation done in the GravMod modelling tool (OCTIO Gravitude 2014) used for the forward modelling of gravity. Then the computation done for the Bouguer anomaly is discussed, and lastly the approach for modelling of the time-lapse gravity field is given.

3.1 Generation of a density map

The velocity model used in the analysis is a 3D P-wave model produced by Nakanishi, N. Takahashi, Yamamoto, et al. (2018), covering the whole southwestern Japan down to 60 km depth. The details of the 3D model will be discussed further in Chapter 4.1. To convert the P-wave velocities to densities, a geological model is created to make sure different velocity ranges are converted to realistic density values.

The geological model is constrained using literature on geological properties of the Kii Peninsula subsurface, combined with velocity ranges estimated by Nakanishi, N. Takahashi, Park, et al. (2002) and Nakanishi, N. Takahashi, Yamamoto, et al. (2018) corresponding to certain rock layers. Next, physical and geological properties are defined for the different rocks in the geological model. The properties include mineral composition, with their corresponding shear and bulk modulus, porosities and typical density values. The last property is studied to make sure the estimated densities are realistic, which is particularly important for the deeper layers where the porosity values are less constrained. The details of this background model will be discussed further in Chapter 4.2.

The equation used for the density conversion is based on the P-wave equation through a homogeneous medium (Mussett and Khan 2000):

$$v_p = \sqrt{\frac{K + \frac{4}{3}\mu}{\rho}} \tag{3.1}$$

Where K and μ are the effective bulk and shear modulus of the medium the wave travels through, and ρ is the bulk density.

To find the bulk and shear modulus of a porous rock, the Hashin-Shtrikman upper bounds are used, which indicate the highest bulk and shear modulus possible for a rock with a given porosity and constituent properties (Mavko, Mukerji, and Dvorkin 2009).

3.1.1 Hashin-Shtrikman bounds

The Hashin-Shtrikman bounds assume that both the medium and the mineral are isotropic, elastic and linear (Mavko, Mukerji, and Dvorkin 2009). Figure 3.1 illustrates the physical meaning of the effective bulk modulus computation. The medium is divided into spheres, where the shell of the sphere (light gray portion) is defined as one constituent of the medium, and filled with the other constituent (dark gray portion) (Mavko, Mukerji, and Dvorkin 2009). For a porous rock, the constituents would then be the solid and the fluid phase within the rock. The upper bounds are obtained when the shell is the mineral, filled with the fluid, while the lower bounds are obtained by defining the fluid as the shell (Mavko, Mukerji, and Dvorkin 2009).

The actual effective modulus of the medium will have values somewhere within these two bounds. To our knowledge, there is little to no information on the geometry of the solid rock and pore space in the modelled area. Thus, the effective bulk and shear modulus is not constrained further than these bounds.

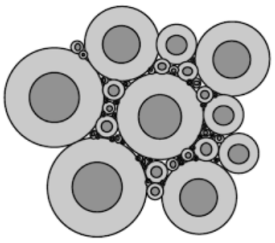

Figure 3.1: Interpretation of the Hashin-Shtrikman bounds for bulk modulus. (Source: Mavko, Mukerji, and Dvorkin (2009))

For a medium with one dominant mineral, given the bulk modulus (K) and shear modulus (μ) of the mineral and fluid, and the porosity (ϕ) of the medium, the Hashin-Shtrikman upper bounds for the effective bulk and shear modulus of the medium are computed using Eq. 3.2a,b (Mavko, Mukerji, and Dvorkin 2009):

$$K^{HS^+} = K_m + \frac{\phi}{(K_f - K_m)^{-1} + (1-\phi)(K_m + \frac{4}{3}\mu_m)^{-1}} \tag{3.2a}$$

$$\mu^{HS^+} = \mu_m + \frac{\phi}{(\mu_f - \mu_m)^{-1} + \frac{2(1-\phi)(K_m+2\mu_m)}{5\mu_1(K_m+\frac{4}{3}\mu_m)}} \tag{3.2b}$$

The subscripts m and f on the shear and bulk modulus account for the moduli of the mineral and fluid, respectively.

In the case of a medium where several dominant minerals are used, the equations are modified to account for the fraction of each mineral present within the solid rock. The bounds are then given by Eq. 3.3a,b (Mavko, Mukerji, and Dvorkin 2009).

$$K^{HS^+} = \left[\frac{\phi}{K_f + \frac{4}{3}\mu_{max}} + (1-\phi)\sum_{i=1}^{N}\frac{f_i}{K_{m,i} + \frac{4}{3}\mu_{max}}\right]^{-1} - \frac{4}{3}\mu_{max} \tag{3.3a}$$

$$\mu^{HS^+} = \left[\frac{\phi}{\mu_f + \zeta(K_{max}, \mu_{max})} + (1-\phi)\sum_{i=1}^{N}\frac{f_i}{\mu_{m,i} + \zeta(K_{max}, \mu_{max})}\right]^{-1} - \zeta(K_{max}, \mu_{max}) \tag{3.3b}$$

where

$$\zeta(K_{max}, \mu_{max}) = \frac{\mu_{max}}{6}\left(\frac{9K_{max} + 8\mu_{max}}{K_{max} + 2\mu_{max}}\right)$$

The variables K_{max} and μ_{max} are defined as the largest bulk and shear modulus for the mineral constituents, and the sum denotes the sum over the different mineral properties, where N is the number of minerals. The fraction of each mineral in the solid rock volume is indicated by f_i (Mavko, Mukerji, and Dvorkin 2009).

3.1.2 Converting velocities to density

Starting with Eq. 3.1, the direct relation between v_p and ρ would be:

$$\rho = \frac{K + \frac{4}{3}\mu}{v_p^2} \tag{3.4}$$

However, for constant K and μ the relation will lead to a decrease in densities with increased velocities. This will not reflect realistic density increase with depth within layers, which is caused by a porosity decrease with depth. Since little is known on the variation of porosity within each layer, an empirical equation is derived through Eq.3.4, creating a proportionality between the velocities and densities and reflecting more realistic density increases within the rock layers. The empirical relation is based on Eq.3.1 and the effective bulk and shear modulus found by Eq.3.2 or 3.3. Each rock type in the geological model is assigned a velocity interval, with a maximum and minimum value for the P-wave velocities to include in each layer. Before the densities are computed, the velocities from the 3D model are divided into the separate layers, based on these velocity intervals. The relation between the P-wave velocities and densities is then given by:

$$\rho_{ij} = \alpha_i v_{p,ij} \tag{3.5}$$

where

$$\alpha_i = \frac{K_i + \frac{4}{3}\mu_i}{\overline{v_{p,i}}^3}$$

The subscripts i and j are determined by the rock layers and the P-wave velocities in the layer, respectively, where the velocity values are from the 3D velocity model. Thus, $i = 1 : N$ where N is the number of layers in the geological model, and $j = 1 : M_i$, where M_i is the number of velocities of the 3D velocity model corresponding to the $i'th$ layer. The number of velocity values in each layer varies across the entire 3D velocity model, as the thickness of the layers vary. Equation 3.5 uses the computed K^{HS+} and μ^{HS+} values, assuming these are constant throughout each layer, and the mean P-wave velocity of the predefined velocity interval, $\overline{v_{p,i}}$. These variables are constant, and $v_{p,ij}$ is the $j'th$ velocity value within the $i'th$ layer, used for the density estimation.

3.1.3 Uncertainties in density conversion

The computation of the Hashin-Shtrikman bounds assumes no cracks or faults in the rocks, along with the general assumptions of an isotropic, linear medium (Mavko, Mukerji, and Dvorkin 2009). This implies constant porosity and bulk- and shear modulus within each rock, which is a simplification of the properties. Realistically, all these variables will vary within a rock, especially with depth. Specifically, the constant porosity with depths gives an overestimation of the fluid contained in the entire rock.

A test is conducted using the lower-, upper- and a mean value of the Hashin-Shtrikman bounds, which reveals that the upper bounds give the best estimate of densities compared to theoretical mean density values of each rock (Schön 2015; Mussett and Khan 2000). Since Eq. 3.2 and 3.3 give the upper bounds of the effective bulk and shear modulus of the rock, the estimated values are likely higher than real values for the rock. However, the estimation is satisfactory for the time-lapse modelling, considering the high uncertainties in general rock properties within the modelled region.

The most important factor is that densities are within reasonable values for the modelling purpose, and reflect an increase with depth. For the deeper layers, computation of the effective bulk and shear modulus within a porous media might not be the best fit due to low porosities generally found in these rocks. However, for the time-lapse gravity computation, the lower layers will not be altered and will therefore not affect the time-lapse gravity signal.

3.2 Gravity computation

For the forward modelling of gravity, two steps are taken. First, the 3D density map with point values is discretized into a 3D distribution of rectangular prisms representing the forward modelling grid. Next, the gravitational potential on a point within a grid of surface measurement points is computed analytically from each prism. These steps are conducted through the GravMod modelling tool (OCTIO Gravitude 2014), and the concept behind the computation will be described here.

In the simplest form, computing the gravity field is based on Newton's law of gravitation (Young and Freedman 2016):

$$F = G\frac{Mm}{r^2} \tag{3.6}$$

This states that the gravitational force exerted on an object of mass m from an other object of mass M with a distance r apart, is inversely proportional to the squared of the distance between the objects. Here, G refers to the gravitational constant, $G = 6.67384 \times 10^{11}$ $\mathrm{Nm^2/kg^2}$ (Young and Freedman 2016). Equation 3.6 approximates the gravitational pull from the Earth as if all of its mass is located at the center, assuming that Earth is a spherical symmetric body (Young and Freedman 2016). As the Earth is not a perfect sphere, but rather approximated as an ellipse (Jacoby and Smilde 2009), this force varies with latitude. For instance, the attraction from a mass at the surface near the poles will have a greater force than a mass near the equator, where the Earth bulges out creating a larger distance r between the surface mass and the center of the Earth. Equation 3.6 is the basis for the forward modelling.

The gravity computation is conducted on separate filled rectangular prisms of given density and volume within the model. The rectangular prisms have a uniform horizontal extent in x and y direction of length dx and dy, defined such that the lateral density variations can be resolved adequately. An illustration of a prism is given in Figure 3.2. If the size of the prisms are too large, they will not give a good representation of the local geology and the curvature of the layers. Each individual prism has a given mean density and a height defined by the uniformity of the density within the layer it encompasses. A tolerance is defined for the range of density values to include within each prism, and densities within a certain percentage of the initial density value included in each prism are grouped together. The height is then defined by the depth of these density values. Thus, layers with highly varying densities with depth are discretized into more prisms than layers with uniform density.

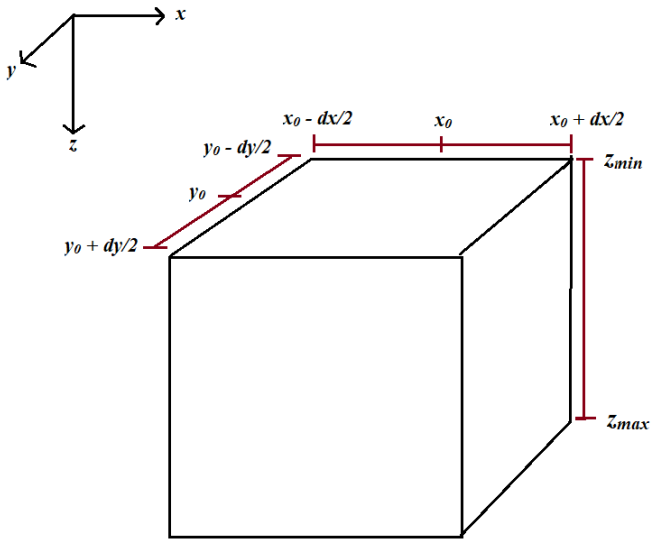

Figure 3.2: Illustration of a rectangular prism. The coordinates x_0 and y_0 correspond to the 2D grid coordinates of the studied density profile. The extent of each prism is predefined as dx and dy, and the 2D coordinates define the center of the prism. The z_{min} and z_{max} coordinates are based on the depth of the initial density value ($\rho(z_{min})$) and the last density value included in the prism ($\rho(z_{max})$).

3.2.1 Computing gravity from a rectangular prism

The gravity computation is based on the fact that the gravity potential of a mass in the subsurface does not influence the potential of other masses in the vicinity (Jacoby and Smilde 2009). In other words, the gravity response at a point P from a mass M within a volume V is independent of the surrounding mass distribution. The entire area is divided into a set of rectangular prisms, where the effect of the gravity potential can be computed by summing over individual volume integrals. A grid of measurement points, P_i, are then defined at certain depths in the 3D model, and the effect of the 3D prism distribution is computed on each individual point.

The gravitational attraction at a certain point on the Earth is defined by combining Eq. 3.6 and Newton's second law, $F = ma$. Through this, Eq. 3.7 is derived for the gravitational acceleration:

$$g = G\frac{M}{r^2} \tag{3.7}$$

This gravitational acceleration, g will have an average value of 9.81 m/s^2 (Jacoby and Smilde 2009). Through forward modelling, a value δg is computed from the rectangular prisms on a set of surface measurement points (Jacoby and Smilde 2009).

The computation does not account for the total mass of the Earth, but rather a section within. When discussing the computations, δg will be used to describe the gravity value for individual rectangular prisms. $\vec{g}$ is a vector in space, however only the z-direction is important for the computation as this is the dominant effect of gravity and what is measured through gravity surveys (Jacoby and Smilde 2009).

By differentiating Eq. 3.7 for the vertical direction, and using the fact that a section of the mass of the rectangular body, dm, can be written as $dm = \rho dV$, the gravity potential from the volume of an individual prism can be estimated through the following equation (Jacoby and Smilde 2009):

$$\delta g = \iiint G \frac{\rho \vec{r}}{r^3} dV \tag{3.8}$$

For Eq. 3.8, ρ is the density of the mass, $\vec{r}$ is the vector from the source mass to the measurement point, and r is the distance between them. Since only z-direction is considered, $\vec{r}$ is replaced b z. In addition to this, the distance between the mass and the measurement station, r can be written as $r = \sqrt{x^2 + y^2 + z^2}$ in Cartesian coordinates. Inserting this into Eq. 3.8 leads to the following equation:

$$\delta g_z = \iiint_B G \frac{\rho z}{\sqrt{x^2 + y^2 + z^2}^3} dV \tag{3.9}$$

Equation 3.9 implies integration of the gravity over the volume of a body B. To deduce the equation for gravity potential of a rectangular prism of volume V, a simpler case is introduced: the effect of a thin plate of constant density ρ, illustrated in Figure 3.3.

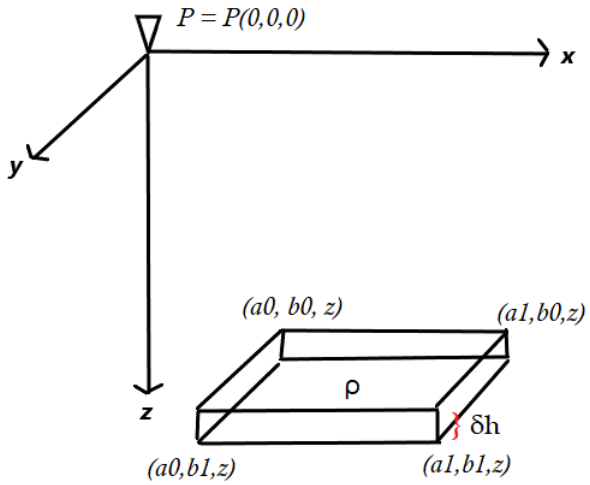

Figure 3.3: Illustration of the measurement point P relative to the thin plate.

First, assume that the gravity effect is from a thin, horizontal plate, with corners in the coordinates $(a_0, b_0, h), (a_1, b_0, h), (a_0, b_1, h)$ and (a_1, b_1, h) where $z = h$, on a point P in the origin, $(0, 0, 0)$. The thickness of the plate is given by δh and is infinitesimally small (Jacoby and Smilde 2009). The gravity from this plate to the measurement point P is given by:

$$\delta g = G\rho \int_{h}^{h+\delta h} \int_{a_0}^{a_1} \int_{b_0}^{b_1} \frac{z}{\sqrt{x^2 + y^2 + z^2}^3} dydxdz \tag{3.10}$$

Where ρ is constant within the plate and can therefore be extracted outside of the integral together with G. The first integral w.r.t. y becomes:

$$\delta g = G\rho \int_{h}^{h+\delta h} \int_{a_0}^{a_1} \left[\frac{yz}{(x^2 + z^2)\sqrt{x^2 + y^2 + z^2}} \right]_{y=b_0}^{y=b_1} dxdz \tag{3.11}$$

This produces two equations with the limits $y = b_0$ and $y = b_1$. Writing $b = b_1$, the first limit can be integrated w.r.t. x to get the following equation:

$$\delta g = G\rho \int_{h}^{h+\delta h} \tan^{-1}\left(\frac{bx}{z\sqrt{x^2 + b^2 z^2}}\right) \Bigg|_{x=a_0}^{x=a_1} dz \tag{3.12}$$

As previously, writing $a = a_1$ and integrating the first limit this time w.r.t. z gives the equation:

$$\begin{aligned}\delta g =& G\rho\Bigg[z\tan^{-1}\left(\frac{ab}{z\sqrt{a^2+b^2+z^2}}\right) - b\tanh^{-1}\left(\frac{\sqrt{a^2+b^2+z^2}}{a}\right) \\ & - a\tanh^{-1}\left(\frac{\sqrt{a^2+b^2+z^2}}{b}\right)\Bigg]_h^{h+\delta h}\end{aligned} \tag{3.13}$$

For each limit of a and b, Eq. 3.13 is computed. By evaluating the integral of Eq. 3.12 in the points $b = b_0, b = b_1, a = a_0$ and $a = a_1$, the gravitational effect of the plate on the point P is given by Eq. 3.14:

$$\begin{aligned}\delta g =& G\rho\int_h^{h+\delta h} \tan^{-1}\left(\frac{a_1 b_1}{z\sqrt{a_1^2+b_1^2+z^2}}\right) - \tan^{-1}\left(\frac{a_0 b_1}{z\sqrt{a_0^2+b_1^2+z^2}}\right) \\ & - \tan^{-1}\left(\frac{a_1 b_0}{z\sqrt{a_1^2+b_0^2+z^2}}\right) + \tan^{-1}\left(\frac{a_0 b_0}{z\sqrt{a_0^2+b_0^2+z^2}}\right)dz\end{aligned} \tag{3.14}$$

Where 3.14 integrates over the height of the plate. Each of the four functions in Eq. 3.14 integrate into Eq. 3.13 and must be evaluated at the limits h to $h+\delta h$, a_0, a_1, b_0 and b_1. By summing several thin plates with equal density, the total influence of the prism, B, on the surface point will be given by Eq. 3.14 with the z-interval given as z_{min} to z_{max}, indicating the minimum and maximum depth of the prism coordinates. Integrating this equation therefore gives the gravity potential exerted on the measurement point P from the rectangular prism volume V.

A measurement point P is influenced by volume elements within the solid angle, $d\Omega$, illustrated in Figure 3.4 (Jacoby and Smilde 2009). This solid angle indicates the projection of the prisms in the subsurface on the unit sphere around the measurement point P (Jacoby and Smilde 2009).

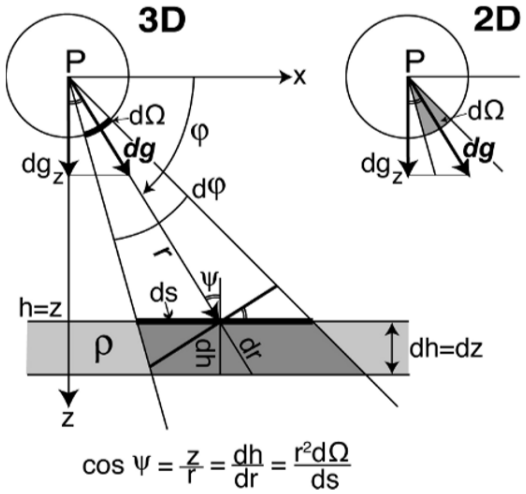

Figure 3.4: Illustration of the solid angle projection of a body with density ρ on the unit sphere around the measurement point P. (Source: Jacoby and Smilde (2009))

The angle Ψ gives the incidence angle of the 'ray' through $\vec{dg}$ on the plate, and the normal component of $\vec{dg}$ is given by $dg_z = G\rho dh d\Omega$. For a plate of uniform height h and infinite horizontal extent, $d\Omega = 2\pi$ (Jacoby and Smilde 2009), which is the case for the Bouguer plate which will be discussed further in Section 3.3. The solid angle decides how much an object can influence the measurement point P, and the influence is within a cone from the source to the object, or objects, in the subsurface, as illustrated in Figure 3.4.

Equation 3.14 is defined for a measurement point in the origin. To generalize the equation for any point within a grid of measurement points with coordinates $P(x_i, y_i, z_i)$, coordinate transformation is applied to the prism coordinates, to shift them relative to the measurement point (Nagy, Papp, and Benedek 2000). The coordinates of the the prisms are then defined by the following transformations (Nagy, Papp, and Benedek 2000), given the coordinates of a measurement point $P(x_i, y_i, z_i)$:

$$\begin{cases} X_{j,min} &= x_{j,min} - x_i \\ X_{j,max} &= x_{j,max} - x_i \\ Y_{j,min} &= y_{j,min} - y_i \\ Y_{j,max} &= y_{j,max} - y_i \\ Z_{j,min} &= z_{j,min} - z_i \\ Z_{j,max} &= z_{j,max} - z_i \end{cases}$$

The subscript i indicates the measurement point, and the subscript j indicates the individual prism used for the computation. The coordinates $x_{j,min}, x_{j,max}, y_{j,min}, y_{j,max}, z_{j,min}$

and $z_{j,max}$ are the original coordinates for the corners of a prism j. The variables $X_{j,min}, X_{j,max}, Y_{j,min}, Y_{j,max}, Z_{j,min}$ and $Z_{j,max}$ define the shifted coordinates of the prism relative to the measurement point. The integration limits a_0, a_1, b_0 and b_1 given in Eq. 3.14 define the minimum and maximum x- and y-coordinates, and a general z-coordinate is transformed by $Z_j = z_j - z_i$. The final equation for the gravity potential of an individual prism on a measurement point P_i is given by integrating Eq. 3.15 below.

$$\begin{aligned}\delta g_{ij} = G\rho \int_{Z_{j,min}}^{Z_{j,max}} \Bigg[& \tan^{-1}\left(\frac{X_{j,max}Y_{j,max}}{Z_j\sqrt{X_{j,max}^2 + Y_{j,max}^2 + Z_j^2}}\right) \\ & - \tan^{-1}\left(\frac{X_{j,min}Y_{j,max}}{Z_j\sqrt{X_{j,min}^2 + Y_{j,max}^2 + Z_j^2}}\right) \\ & - \tan^{-1}\left(\frac{X_{j,max}Y_{j,min}}{Z_j\sqrt{X_{j,max}^2 + Y_{j,min}^2 + Z_j^2}}\right) \\ & + \tan^{-1}\left(\frac{X_{j,min}Y_{j,min}}{Z_j\sqrt{X_{j,min}^2 + Y_{j,min}^2 + Z_j^2}}\right)\Bigg] dz\end{aligned} \tag{3.15}$$

The gravity potential of all the prisms on an individual measurement point P_i is then given by Eq. 3.16:

$$\delta g_i = \sum_{j=1}^{N} \delta g_{ij} \tag{3.16}$$

Thus, the gravity value at each measurement point is a sum of the force exerted on the point from the 3D distribution of rectangular prisms within the solid angle of the measurement point. In Eq.3.16, N is defined by the number of prisms in the distribution. The subscript i in δg_{ij} indicates that the gravity value from the individual prism is computed relative the measurement point P_i.

The aim of the computation is to find the surface gravity from each individual prism in the 3D model, δg, and sum up the effect of all filled rectangular prisms on individual measurement points. The effect of each prism is computed analytically using Eq. 3.15 through the GravMod modelling tool (OCTIO Gravitude 2014), and each δg_{ij} is summed up to account for a total observed gravity at the measurement points using Eq. 3.16. In addition to the prisms below each measurement point, the prisms above exert a negative gravity potential on the measurement point, thus the prisms here reduce the computed gravity value.

3.3 Bouguer anomaly computation

To validate the reference density map, it needs to be compared to actual gravity values. This is done by comparing with two maps showing Bouguer anomalies over the Kii Peninsula, obtained through the GALILEO databse (Geological Survey of Japan 2019), which are discussed further in Chapter 4.3. Since the density map is a three dimensional cube, a latitude correction is not needed. Thus, the modelled absolute gravity values only require a terrain correction and Bouguer correction.

The modelled gravity values are computed assuming measurements points at sea level, $z = 0$. Terrain and Bouguer corrections have been applied to the computed gravity values, and two separate approaches have been used to apply each correction, attempting to replicate the anomalies displayed in the maps. The following sections discuss the details behind the Bouguer and terrain corrections.

3.3.1 Bouguer correction

The Bouguer correction corrects for the ocean densities, essentially filling the ocean with a crust of constant density, $\rho_c = 2670$ kg/m^3. This has been done through:

1. A Bouguer plate approximation
2. Computing directly using modeled prisms for the ocean volume

The first approach uses the equation for the Bouguer plate (Jacoby and Smilde 2009):

$$\delta g_B = 2\pi G z(\rho_c - \rho_w) \tag{3.17}$$

Where ρ_c is the defined average density of the crust, commonly used for Bouguer corrections (Jacoby and Smilde 2009), and ρ_w is a constant ocean density. The depth, z, is defined by the depth from the sea surface down to the seafloor. The modelled seafloor is defined by studying density values of seafloor sediments in the density map, which will be discussed further in Chapter 5.2. The Bouguer plate is used as an approximation for all the mass below the observation point. For each measurement point, a Bouguer plate of thickness z corresponding to the depth down to the seafloor is used to compute the gravity at the point. Thus, an infinite slab is modeled as the source of the gravity variation from the ocean layer at this point. Through this correction, the effect of the ocean densities have been removed, and the effect of crustal densities added to avoid the seawater anomaly masking anomalies in the crust.

The second approach considers the distribution of rectangular prisms in the model. The prisms corresponding to the ocean layer are chosen, and the mean densities

within are replaced with values $\rho = \rho_c - \rho_w$. The computed gravity values from these prisms with the new density value are then added to the total computed gravity values.

3.3.2 Terrain correction

Terrain correction is a correction of the Bouguer plate assumption – this effect corrects for the varying terrain where the Bouguer correction assumes a horizontal or smooth surface (Jacoby and Smilde 2009). The modelled gravity is computed by excluding contributions from all the mass elements above the assumed measurement locations at sea level. Hence, the terrain correction is already included in the modelled gravity response.

The Bouguer anomaly maps from the GALILEO database (Geological Survey of Japan 2019) are found using a terrain correction with the same average crustal density used in the Bouguer correction. Since the crustal density of the terrain above sea level may deviate from this average crustal density, an additional terrain correction is applied. This correction uses the average density value to remove the effect of the terrain above sea level on the gravity measured at each point. The correction is then used to determine if the initial terrain corrected gravity is sufficient to replicate the map values, or if the added correction with average density values is better suited. The second approach to terrain corrections follows the steps below:

1. Gravity values for the landmass above sea level are computed, excluding mass from the air layer.

2. The computed gravity values from the landmass are subtracted from observed gravity at sea level. This therefore includes the negative effect of densities above the measurement point to the absolute gravity.

3. Gravity values are computed for the terrain correction using new densities within the prisms.

4. The terrain correction is subtracted from the measured gravity values at sea level.

The densities used for the second terrain correction are defined by $\rho = \rho_c - \rho_r$, where ρ_r is the actual density of the prism. The different Bouguer anomaly results are then compared to the original Bouguer anomaly maps, showing which correction gives the best results.

3.4 Time-lapse modelling

The time-lapse gravity modelling involves computing the gravity signal resulting from alterations of properties of the rectangular prisms, accounting for volume and density variations of the rocks. The modelling has been conducted through three separate scenarios, aiming to model fluid migration in rocks relating to slow earthquake processes:

1. Fluid increase along the descending plate
2. Fluid increase at slow earthquake locations
3. Compression within accretionary prism sediments

The scenarios will be discussed in more detail in Chapter 5.4, but the method for computing the actual time-lapse gravity values for the three scenarios is done in the same fashion. The time-lapse modelling includes the following steps:

1. Define a threshold for the gravity value which would be possible to detect at the surface
2. Define which rectangular prisms are assumed to experience mass changes following the scenarios mentioned above
3. Define alterations to be done with the rectangular prisms chosen for the analysis, reflecting volume or density variations
    - For volume alterations, new blocks dV are defined. The height, dh, is constant for all new blocks, and the x and y extent of the new block is equal to the original prism.
    - The density in each new block is constant and corresponds to water density, ρ_w
    - Volume increase is modelled through adding dV on top of the prism (as in Figure 3.5a)
    - Volume decrease is modelled through a "lowering" of the prism height (as in Figure 3.5b), removing a volume dV from the prism
    - Pure density alterations are done by changing the effective density within the volume V of the entire prism

    .
4. Compute gravity for the applied changes to the prisms, either the altered volume section dV or the volume with an altered density $\Delta\rho$. Since it is assumed that no changes occur elsewhere in the model, and the only change

within the chosen prism is the fluid volume, the computation is only necessary for the fluid variation.

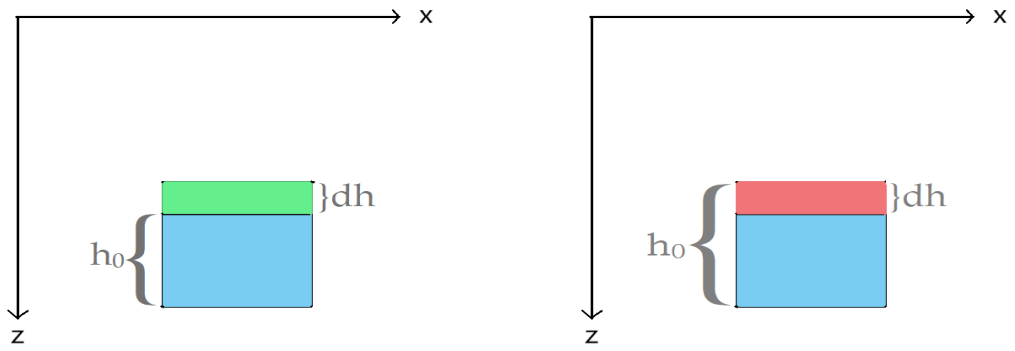

(a) Illustration of volume increase

(b) Illustration of volume decrease

Figure 3.5: Volume alterations of prisms in two dimension. The height h_0 is the original height of the prism, while dh is the height either added (green section in (a)) or removed (red section in (b)).

The illustrations in Figure 3.5a,b show how the rectangular prisms are modified for generating the time-lapse signal. A section dV of fluid volume is added on top of the prism to model a volume increase, while a section dV of fluid volume is removed from the top of the prism to model a decrease in volume.

An illustration defining the location of the modelled scenarios can be found in Chapter 5.4, Figure 5.7, where a more detailed explanation of the three scenarios is given. Scenario 1 involves an area along the surface of the Philippine plate. The aim here is to see how the surface gravity will be affected by fluid influx on the interface. Scenario 2 involves specified locations within the accretionary prism, aiming to model a case where the slow earthquake locations are given and fluid increase is likely to occur prior to or during the event. Both scenarios 1 and 2 are set up based on actual slow earthquake locations, which are discussed further in Chapter 4.4.

Scenario 3 involves alterations along the trough, where compression is likely to occur. The prisms are chosen from a sedimentary rock section here, and alterations will be made to model compression of the rock, and therefore a porosity decrease. The compression is modelled either through a decrease in volume, or a constant volume and an increase in density. The first approach models a situation where compression of the rock causes volume loss through pore space reduction, while the second approach implies that the volume is not lost for the individual prism element, but some of the pore space is replaced by solid rock. Both cases model fluid loss within the rock. When computing the density changes at constant volume, the time-lapse density $\Delta\rho$ is computed using the following equation:

$$\Delta\rho = (\rho_r - \rho_w)\Delta\phi \tag{3.18}$$

Where ρ_r is the original density of the rock, that replaces parts of the water density within the compressing pore space, and $\Delta\phi$ is the porosity loss.

Chapter 4

Data

The aim of the forward modelling is to study the size and extent of density variations in the subsurface of the Nankai trough that may cause observable temporal gravity variations. To conduct the forward modelling of gravity, I first needed to define a density distribution for the chosen region of the Nankai trough around the Kii Peninsula. Starting with a detailed 3D P-wave velocity model provided by JAMSTEC, I aim to create a 3D density mapping of the velocities, reflecting the details of the subsurface structures provided by the velocity distribution. I chose the section of the velocity model corresponding to the Kii Peninsula region, considering the extensive slow earthquake activity within this region and thus the possibility of detecting temporal gravity changes here. The DONET1 network provides detailed information of the earthquake activity near the trough, making it simpler to relate density changes with earthquakes here.

I started by creating a geological model, using the layering of the velocity model. I chose which rocks to assign to each layer by comparing literature involving several studies of seismic sections along the Nankai trough. I studied additional literature on the Shimanto belt rock group in further detail, assuming that this section defines the upper crust of the island arc.

After I assigned a specific rock type to each layer, physical and mineralogical properties of the rocks were determined through studying relevant literature on rock properties, in addition to detailed drill reports describing results from various IODP expeditions. The layers of the geological model are then defined by each rocks' porosity, elastic moduli and P-wave velocity range. By using the constructed geological model, I converted the 3D velocity model to a 3D density map, allowing for use in the forward modelling of gravity.

To validate the density map, I chose to compare the modelled absolute gravity based off the density map to two Bouguer anomaly maps, provided by the GALILEO

gravity database of the Geological Survey of Japan. I chose two maps that include parts of the offshore region of the Kii Peninsula, considering that the time-lapse modelling will involve regions close to the trough axis.

I chose three slow earthquake catalogs that include events near the trough off the Kii Peninsula region. The catalogs represent a range of events from various time periods, with events recorded both by onshore seismic stations, and through ocean-bottom seismometers (OBSs) of the DONET1 network. I have used the catalogs to define scenarios for the time-lapse gravity modelling, where I assume the slow earthquake events are related to variations in fluid flow along fault planes.

In this chapter, a description is given for each of the data sets I have considered throughout the modelling, along with a detailed description of the geological model I created to convert the P-wave velocities to densities.

4.1 P-wave velocity model

The P-wave velocity model resolves the 3D velocity structure over the Nankai trough. The model covers an area of approximately 600×900 km^2, down to 60 km depths. Nakanishi, N. Takahashi, Yamamoto, et al. (2018) constructed the model by combining previous results on the velocity structure of the Nankai trough with new results from their seismic surveys (See Nakanishi, N. Takahashi, Yamamoto, et al. 2018 and references therein)). The seismic surveys were conducted between 2008 and 2012, and long term seismic observations were conducted for 10 months at a time (Nakanishi, N. Takahashi, Yamamoto, et al. 2018).

The model was created in order to better constrain structures within the Nankai trough and increase the coverage of the velocity model, with specific interest in producing the structure of the Philippine plate (Nakanishi, N. Takahashi, Yamamoto, et al. 2018). Through the use of 2D velocity models along seismic lines and 3D tomography, the 3D velocity structure was created (See Nakanishi, N. Takahashi, Yamamoto, et al. 2018 and references therein). The 2D structures were obtained through seismic reflection and refraction surveys, using OBSs and tuned airgun arrays (Nakanishi, N. Takahashi, Yamamoto, et al. 2018). The tomography was conducted with a combination of active and passive sources, using OBSs as receivers (Nakanishi, N. Takahashi, Yamamoto, et al. 2018).

Nine interfaces are located within the model, defined by velocity contrasts across the interfaces, and each layer is described by a given velocity range (Nakanishi, N. Takahashi, Yamamoto, et al. 2018). The 3D velocity model was then created by interpolating grid values between these known interfaces and 2D seismic profiles, finally obtaining a complete 3D velocity structure (Nakanishi, N. Takahashi, Yamamoto, et al. 2018). Through this velocity model, the subsurface of the Nankai

trough is very well constrained, and local variations along the interfaces and within the layers can be seen where previous models showed less variations (Nakanishi, N. Takahashi, Yamamoto, et al. 2018). The 3D structure was verified by comparing hypocenter locations using the new structure and a reference structure by Yamamoto et al. (2013) over the western Nankai trough.

The grid spacing of the 3D P-wave model is 500 m in horizontal direction, and 100 m in vertical direction (Nakanishi, N. Takahashi, Yamamoto, et al. 2018). The data set includes four arrays: the geographical coordinates in decimal degrees of each separate data point, in total 337500 surface coordinates, an array of depth profiles for the surface coordinates, each with 641 points between -4 km and 60 km depths, and a P-wave velocity array corresponding to every depth point. The section chosen for the modelling covers the Kii peninsula and the off-Kii Peninsula area of the trough, including the Kumano basin, the trough axis and parts of the Shikoku basin. The extent of the entire velocity model used for the analysis, shown in Figure 4.1, covers an area of 223×373 km, and depths down to 60 km.

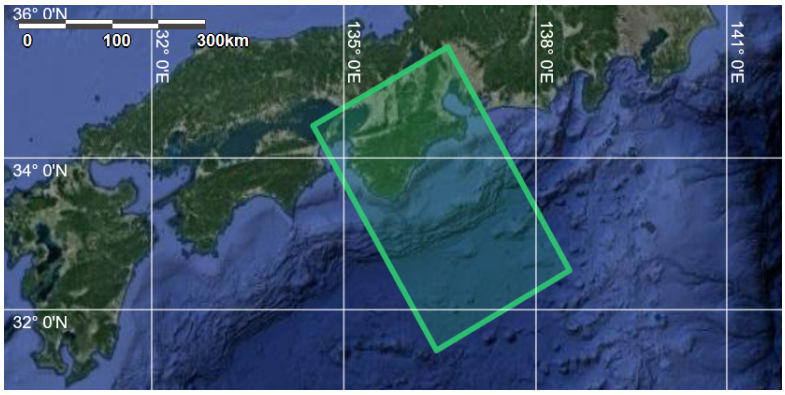

Figure 4.1: Area covered by the total velocity model over the Kii Peninsula. (Source: D-map (2019))

4.1.1 Uncertainties in velocity model

The structure below 40 km uses traces from previous studies by Yamamoto et al. (2013) and Yamamoto et al. (2014) over the Kyushu and Shikoku island segments in the western Nankai trough, therefore they are not as reliable as the upper 40 km structure for the entire region (Nakanishi, N. Takahashi, Yamamoto, et al. 2018).

Higher uncertainty is also observed below onshore regions. Through hypocenter location, the difference between using the 3D velocity structure and the reference velocity structure by Yamamoto et al. (2013) resulted in ±0.05° difference in latitude and longitude, and ±5 km difference in depth (Nakanishi, N. Takahashi, Yamamoto, et al. 2018). The uncertainties of 5 km in depth may have an effect on the observed gravity values using this model, since observed gravity is sensitive to the depth of the structure in the subsurface.

4.2 Geological model

The geological model is created from a combination of geological and geophysical knowledge of the area. First, the velocity model by Nakanishi, N. Takahashi, Yamamoto, et al. (2018) is studied in further detail, and divided into sections, or layers, based on significant changes in velocities. Starting out with a rough velocity range for each of the layers given by Nakanishi, N. Takahashi, Park, et al. (2002) and Nakanishi, N. Takahashi, Yamamoto, et al. (2018), the velocity range is further refined by studying the velocity model in more detail. Profiles from the P-wave velocity model, along with identification of significant jumps in the velocity values, are used to define the velocity range of each layer in greater detail. Within a layer, the velocities increase quite smoothly, and a jump is observed when the P-waves have crossed a layer interface, making it simpler to note when a large variation in velocity occurs and a new layer starts. The interfaces proposed by Nakanishi, N. Takahashi, Yamamoto, et al. (2018) are used, along with an addition to include the three sediment layers defined by Nakanishi, N. Takahashi, Park, et al. (2002). The model is also divided into a subducting and an overriding plate, distinguishing layers found with similar velocity ranges in each of these plates from each other. Dividing the model into an overriding plate and a subducting plate makes it easier to define layers with overlapping velocity ranges.

Defining such a deep geological model is complicated, as it is difficult to determine exact properties of the deepest rocks without drill cores. Cores taken from drill sites covering the Kumano basin and the accretionary prism provide detailed descriptions of the upper sedimentary layers (Underwood and C. Song 2016; Kinoshita et al. 2012), while the layers deeper than 3 km below the seafloor have not been penetrated (Underwood and C. Song 2016). For the deeper portions of the subduction zone model, literature discussing exhumed ancient rock formations and the structure of typical oceanic and island arc crust are combined to create a rough model of the rock distribution at depths (Taira, H. Okada, et al. 1982; Asahiko Taira 2001).

The rock properties needed for the density conversion include mineral composition, with corresponding bulk and shear moduli, a porosity value, and velocity ranges. Values for porosities for the deepest layers, specifically in the island arc crustal model, are difficult to determine through literature, and have therefore been defined by studying the effect of porosity on the density conversion. This might result in inaccurate porosities, while more accurate density values are obtained.

Figure 4.2 illustrates the layering of the geological model. In addition to these rock layers, two other layers are included in the velocity model: one ocean layer and one layer representing air. The cross-section of Figure 4.2a is chosen at a longitude of approximately 136.5°, stretching from north to south across the model area, as indicated by Figure 4.3. Therefore, the cross section is not perpendicular to the

trough axis, but still gives an illustration of the layers within the model.

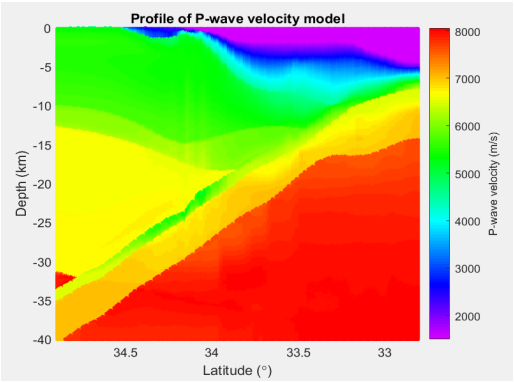

(a) Cross-section of the 3D P-wave velocity model.

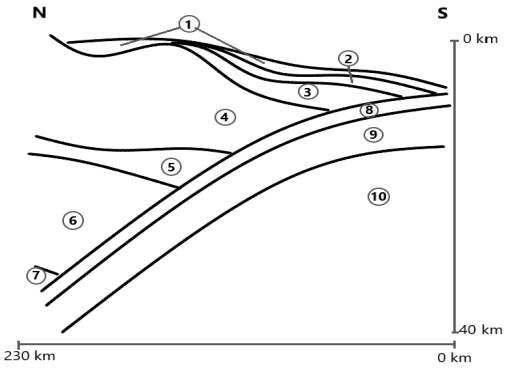

(b) Division of layers within the subduction zone.

Figure 4.2: Cross section of the velocity model by Nakanishi, N. Takahashi, Yamamoto, et al. (2018), compared to the division of layers within the geological model. The cross section in a) is chosen at 136.5 ° latitude.

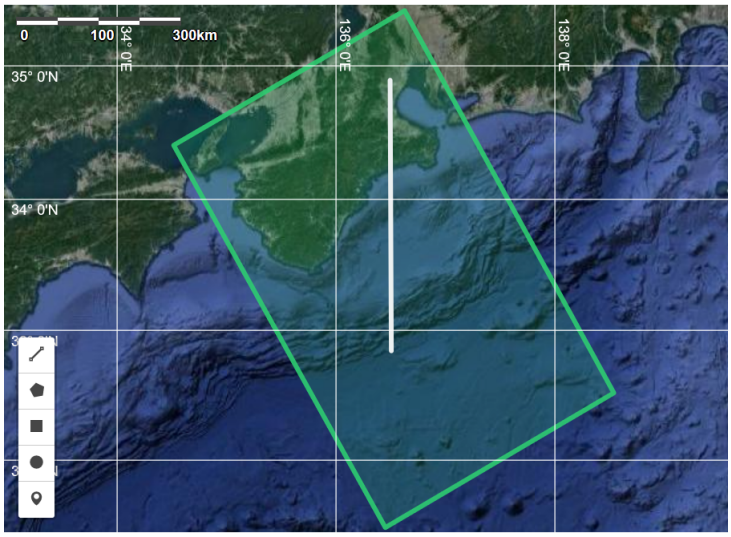

Figure 4.3: Location of the cross-section within the model region. (Source: D-map (2019))

4.2.1 Island arc crust

The rocks chosen for the island arc crust model are summarized in Table 4.1, defining layers 1-7 in the geological model of Figure 4.2b.

Layer	Rocktype	Mineral	Porosity (%)	Velocity (m/s)	Density (kg/m^3)
1	Unconsolidated sediment	Clay	70	1600 - 2046	1760 - 2251
2	Mudstone	Smectite and Illite	55	2046 - 3115	1674 - 2549
3	Sandstone	Feldspar	25	3115 - 4700	1751 - 2643
4	Limestone	Calcite	25	4700 - 5700	2273 - 2757
5	Basalt	Augite and feldspar	5	5700 - 6349	2451 - 2730
6	Gabbro	Augite	10	6349 - 7200	2832 - 3033
7	Peridotite	Olivine	10	7200 - 8177	3184 - 3467

Table 4.1: Rocks used for island arc geology model. The corresponding minerals, porosities, density- and velocity ranges are given.

The first three layers are sedimentary. The upper sediments are in reality quite complicated, with several turbiditic deposits, mostly consisting of mud interlayered with varying amounts of ash, silt and sand (Underwood and Pickering 1996). To simplify the model, they are divided into three layers which are based on the layered structure of turbidite sequences. Results from IOPD expedition 314, 315, 316 and 338 (Kinoshita et al. 2009; Kinoshita et al. 2012; Underwood and C. Song 2016) are used to determine sediment properties within the accretionary prism. The drill cores show high variations in lithology within the accretionary prism, implying that some simplification of this lithology must be applied when choosing rocks to determine the three sedimentary layers.

The drill sites are shown in Figure 4.4. Through studying drill reports, and taking into account that turbidite sequences have coarser grains at depth (Mulder and Hüneke 2013), specific rocks are chosen to represent the three sediment layers. Layer 1 is defined as unconsolidated clay, with a high porosity of 70% near the surface determined by studying reports by Bray and D. Karig (1985) and Screaton et al. (2009). General clay minerals are chosen to represent this layer, with their properties given by Schön (2015).

Layer 2 is based on results from site C0002 within the Kumano basin. Kinoshita et al. (2012) define different lithological units within the upper sedimentary layers, and unit 4, directly below the Kumano basin sediments, consist mainly of clayey siltstone and silty claystone (Kinoshita et al. 2012). Based on the results from IODP expedition 315 and 316, mudstone has been chosen to represent the entire second sedimentary layer, to simplify the sediment composition here. The porosity of this layer is defined at 55% based on results from Screaton et al. (2009). The drill

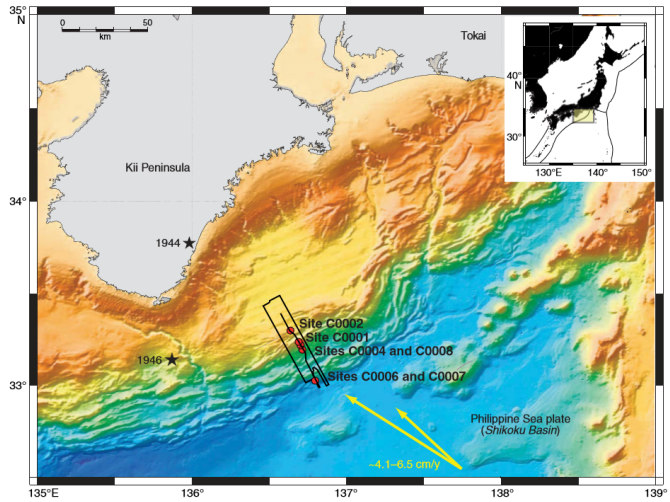

(a) Location of drill sites over the Kumano basin and accretionary prism. The stars indicate epicenters of the Nankai and Tonankai earthquakes. Yellow arrows show the velocity magnitude and direction of the Philippine plate movement, defined by Kinoshita et al. (2012).

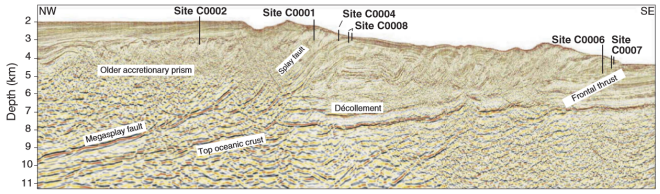

(b) Depth of drill sites within the accretionary prism.

Figure 4.4: Location of drill sites from IODP expeditions 315 and 316. (Source: Kinoshita et al. (2012))

report notes varying amounts of clay minerals within this section, but unit 4 includes a mass fraction of nearly 40 wt% illite minerals and almost the same percentage of smectite minerals (Underwood and C. Song 2016). Based on these results, smectite and illite are chosen as dominant minerals for the mudstone layer.

The last sedimentary section, layer 3, is defined as sandstone. This assumption is based on the fact that turbidite sequences become progressively coarser with depth, with thick coarse basal units (Boggs 2009). In addition to this, the upper layer of the Shikoku basin that subducts below the accretionary prism is rich in turbidite deposits (Taira, Hill, et al. 1992), so it is safe to assume that some of these are included in the lower sedimentary section. Choosing which mineral defines the sandstone layer is difficult, as sandstone generally has a varying mineral composition based on the origin of the sand grains it consists of (Kehew 1994). However, considering how prominent feldspar minerals generally are in rocks (Kehew 1994), this mineral has been chosen as the dominant mineral for the sandstone layer. A specific décollement composition is not included in this model since it could be difficult to constrain accurately using velocity ranges. Therefore, parts of this sandstone section

will represent the location of the décollement zone.

Layer 4 is defined as the upper island arc crust (Nakanishi, N. Takahashi, Park, et al. 2002). This layer is referred to as the old accretionary prism, the tertiary Shimanto belt (Nakanishi, N. Takahashi, Park, et al. 2002). Asahiko Taira (2001) defined the Tertiary Shimanto belt as trench-fill turbities, underlain by hemipelagic and pelagic sediments, and a section of reef limestones underlain by basalts. Based on this, layer 4 is defined as limestone, to simplify the structure of the upper island arc crust. The dominant mineral of this section is defined as calcite based on the mineral composition of limestones presented by Kehew (1994). The inner sections of the tertiary Shimanto belt cannot be defined through the velocity model. Therefore, no such division has been made, and one rock type is chosen to represent the whole layer.

Porosities within this layer are not well constrained, and carbonate rocks are often identified by both primary and secondary porosities (Imbt, Ellison, et al. 1946). Primary porosity refers to the *in situ* porosity values, while secondary porosity occurs due to later chemical weathering of the rock (Imbt, Ellison, et al. 1946). Therefore, these different processes can create highly variable porosity values for limestones. The porosity value chosen for this layer is 25%.

Following studies discussing the old accretionary prism by Asahiko Taira (2001), layer 5 below the limestone layer is defined as basalt. Two minerals are chosen to represent this rock, following mineral compositions given in (Kehew 1994): pyroxene in the form of augite minerals and feldspar. The porosity of this basalt layer is chosen as 5%.

Studies of seismic structures from several island arc systems show that the lower crust is mainly gabbroic in composition (Calvert 2011). Based on this, layer 6 is defined as gabbro in this model as well. The dominant mineral within the layer is defined as augite (Kehew 1994). The remaining layer of the island arc crust, layer 7, is the upper mantle, where the rock type is defined as peridotite, following general upper mantle rock composition (Kearey, Klepeis, and Vine 2009). The dominant mineral is chosen to be olivine (Kehew 1994), and porosities for layer 6 and 7 are chosen as 10% in this model.

4.2.2 Philippine sea plate

For the Philippine plate, three main layers are identified through seismic studies (Nakanishi, N. Takahashi, Park, et al. 2002; Nakanishi, N. Takahashi, Yamamoto, et al. 2018; Kodaira, Kurashimo, et al. 2002). The layers define two crustal layers and an upper mantle layer. This is consistent with the structure of typical oceanic crust consisting of two igneous crustal layers, where the top layer is primarily comprised of basalts, and the deepest portion of the oceanic lithosphere down to the Moho

is composed mainly of gabbro (Kearey, Klepeis, and Vine 2009). Below the crust, an upper mantle layer is added, comprised of peridotite (Kearey, Klepeis, and Vine 2009). The composition of the last two layers follow the composition of the island arc layers 6 and 7, to keep the model consistent. Common rocks found within oceanic crust are then used to define the properties of the three layers of the Philippine plate in the geological model.

In reality, the incoming Philippine plate has a thick upper sediment layer (Sugimura and Uyeda 1973). Within the Nankai subduction zone this sediment layer is only present until a certain depth on the plate interface, and at greater depths only the crustal layers have been identified. There is evidence of underthrust sediments on the plate interface, below the décollement (G. F. Moore et al. 2015). This area extends downdip to an approximate depth of 10 km (G. F. Moore et al. 2015). The incoming sediments are defined as Shikoku basin sediments, and the sediments within the décollement are consistent with lower Shikoku basin sediments, consisting mainly of hemipelagic sediments and turbidite sequences (Taira, Hill, et al. 1992). The underthrust sediment section is important to note in relation to the time-lapse modelling, and will be discussed further in Chapter 5.4.

For the geological model, the sedimentary layer along the surface of the Philippine plate within the Shikoku basin is included in the island arc sediment layers. Since the P-wave velocities and sediment composition of the island arc sediment sections are fairly similar to the Shikoku basin sediments, there is little need to define separate sections for these layers. Thus, the sediments of the Shikoku basin are not included in the Philippine plate model, but as a part of the island arc crust layering discussed in the previous section.

In addition to the sediment section at the surface of the Philippine plate, the section of subducted sediments likely located along the surface of the basalt layer of the Philippine plate are not defined as a separate sedimentary layer within the model. This is done due to difficulties in separating the lower accretionary prism velocities with the velocities of the upper basalt layer. Therefore, it is uncertain where these sediments are located within the velocity model, and it is assumed that the velocities corresponding to the underthrust sediments are grouped together with the accretionary prism velocities.

Three layers are defined as part of the Philippine plate: layers 8-10. Layers 8, 9 and 10 are therefore composed of basalt, gabbro and peridotite, respectively, considering the discussion above. These rocks are similar to layers 5,6 and 7 in the island arc crust section, but with slightly different velocity ranges. For consistency, the same dominant minerals as for the other layers are chosen to represent these layers.

Carlson and Herrick (1990) conducted a study on the densities and porosities of oceanic crust in the Atlantic ocean. Two sites, 418A and 395A, were chosen, where

the age of the crust was 110 Ma and 6 Ma, respectively (Carlson and Herrick 1990). Site 418A was cored down to 544 m within the oceanic crust, and site 395A down to 570 m, with depths given relative to the basement. The results show that for densities above 2600 kg/m^3, the oldest site showed porosities from 15%, and a decrease from with increasing densities. For the youngest site, the porosities were slightly higher for the same density range, reaching porosities of nearly 20% (Carlson and Herrick 1990). The oceanic crust at the Kii Peninsula is approximately 20-25 Ma, based on the spreading age estimated by Okino, Shimakawa, and Nagaoka (1994). It is therefore reasonable to assume porosities within the range of 15-20% could occur here, and the porosity defined for layer 8 is chosen as 15%. The porosities for layer 9 and 10 are again chosen as 10%, as for the previous gabbro and peridotite layers. The rocks defined within the Philippine plate are summarized in Table 4.2.

Layer	**Rocktype**	**Mineral**	**Porosity (%)**	**Velocity (m/s)**	**Density (kg/m^3)**
8	Basalt	Augite and feldspar	15	4520 - 6500	2214 - 3111
9	Gabbro	Augite	10	6449 - 7200	2832 - 3123
10	Peridotite	Olivine	10	7200 - 8177	3182 - 3429

Table 4.2: Rocks used for the Philippine plate geology model. The corresponding minerals, porosities, density- and velocity ranges are given.

Table 4.2 shows that densities within layer 8 have large variations, from 2200 kg/m^3 to 3310 kg/m^3. This variation reflects areas of low velocities along the surface of the Philippine plate (Nakanishi, N. Takahashi, Park, et al. 2002), and high velocities found in the deeper regions of the velocity model. The mineral bulk and shear moduli corresponding to the minerals that are chosen for each layer of the entire geological model are given in Table 4.3.

Mineral	**Bulk modulus, K (GPa)**	**Shear modulus, μ (GPa)**
Clay	20.9	6.85
Illite	39.4	11.7
Smectite	12.3	15.6
Feldspar	37.5	15
Calcite	78.6	32
Augite	94.1	57
Olivine	130	80

Table 4.3: Bulk and shear moduli for minerals (Source: Schön (2015))

4.2.3 Uncertainties in the geological model

A few assumptions are made to create the geological model. First, there are assumed to be no cracks or intrusions in the rocks. The porosities are considered constant with depth for each rock layer, which in reality should be reduced with depth. This is taken into consideration through the density conversion, where the velocity accounts for the density increase with depth following the computations presented in Chapter 3.1.2. Therefore, the bulk density can be computed, and realistic values obtained, without considering an increase of porosity with depth. This is also the case for bulk and shear moduli of the rocks, which are defined as constant within each layer. Hence, the only property altering the density variation with depth within a given layer is the velocity variation.

Tsuji, Juichiro Ashi, et al. (2015) discussed the existence of an igneous dome located within the forearc region off the tip of the Kii Peninsula, overlying the old accretionary prism. However, within the 3D velocity model no obvious variations indicative of such a dome are found in this region. It is therefore not included in the geological model.

The main minerals decide the effective elastic moduli of the rock through the Hashin-Shtrikman upper bounds (as discussed in Chapter 3.1.1). In some cases, this leads to large densities as this is a simplification of rock properties. The model is created without taking into consideration metamorphic altering of the minerals either, which is important especially in the downgoing slab (Kearey, Klepeis, and Vine 2009). This is therefore one of the main uncertainties in this basalt layer. The choice of using either one or two minerals is based on different factors. For the mudstone layer, this is based on logs of clay minerals where both illite and smectite have been observed at above 30 wt% (Kinoshita et al. 2012). For the basalt layers, this second mineral is added in order to constrain porosities to more realistic values. However, for the gabbro and periodite layers, adding a second mineral leads to an underestimation of the densities within each layer. Therefore, the addition of more minerals does not allow for lowering of the porosity values chosen for these layers. In most layers, one mineral is chosen as not to introduce too many uncertain parameters into the model.

Following the discussion above, it is clear that the main uncertainty in this model lies in parts of the Honshu island arc crust and within the deeper layers. For instance, choosing which rock to use for the upper crust (layer 4) is difficult due to variable structures within the old accretionary prism. Due to the difficulty in defining these structures from seismic surveys (Tsuji, Juichiro Ashi, et al. 2015), the upper island arc crust is defined by one layer, which might be a simplification. However, typical velocity values of limestone, ranging between 3.9 - 6.2 km/s (Mussett and Khan 2000), are reasonable within the velocity range for this layer.

When it comes to the lower arc crust, the rock properties are the greatest uncertainty, due to high porosity values chosen here. This might reflect issues with the method for converting these high velocity ranges, or issues with choice of minerals. The properties of the deeper igneous layers could be improved by further constraining typical mineral compositions or reducing the porosity value with depth. However, considering the uncertainties in the geological properties of the model it is problematic to constrain the rock properties within these layers.

The aim of the geological model is to obtain densities that most accurately reflect the properties of rocks within the model region. Therefore, some steps have been taken to obtain these density values that may represent trade offs between mineral composition and porosity values and the need to constrain the complexity in the geological model. The resulting density values remain within reasonable range for the chosen rock types, and are therefore suited for the purpose of gravity modelling.

4.3 Bouguer anomaly maps

To validate the density model created for the modelling, the computed gravity values are compared to known gravity values for the region off the Kii Peninsula. Two maps of Bouguer anomalies are obtained from the GALILEO Gravity database (Geological Survey of Japan 2019). An attempt to recreate the anomaly maps is done through correction of the modelled absolute gravity values.

The maps used for the comparison are given in Figure 4.5. They have been found by using densities of 2670 kg/m^3 for both the Bouguer correction and the terrain correction. They are located within the Kii Peninsula region, where Map 1 partly covers the trough area and parts of the mainland, and Map 2 covers parts of the Kumano basin.

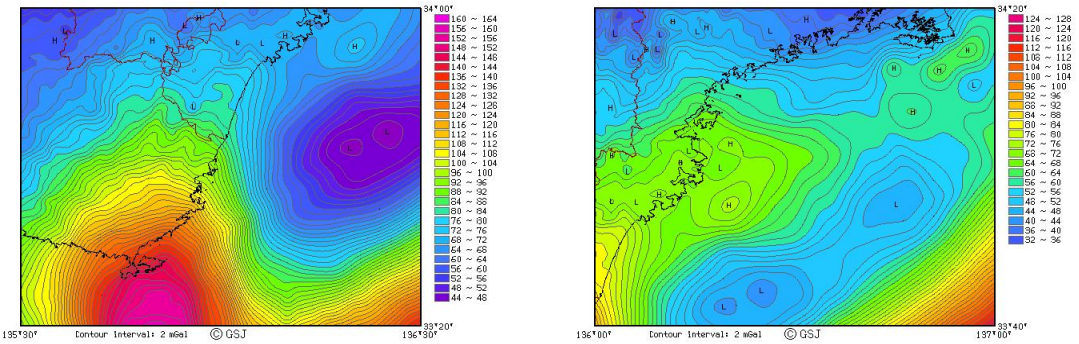

(a) Map 1: Kii Peninsula and Kumano basin

(b) Map 2: Kumano basin area

Figure 4.5: Bouguer anomaly plots over the coast of the Kii Peninsula. Anomaly values are given in mGal. (Source: Geological Survey of Japan (2019)).

An important anomaly to note in Figure 4.5a is the large positive one at the edge of the peninsula. This could reflect the igneous dome discussed in Section 4.2.3, so the anomaly will likely not show up while comparing to the density model since it is excluded from the geological model.

Figure 4.6 shows the locations of the two maps within the area covered by the 3D velocity model.

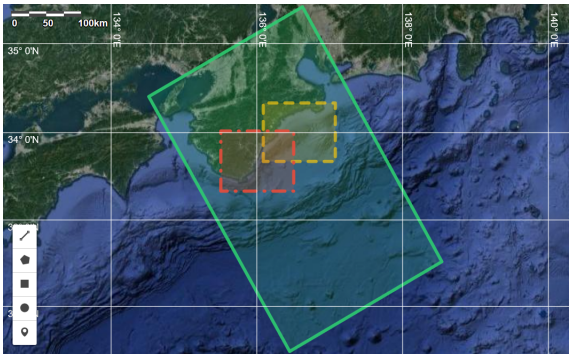

Figure 4.6: Location of the two Bouguer anomaly maps within the study area. The red rectangle indicates the location of Map 1, and the orange rectangle indicates the location of Map 2. (Source: D-map (2019))

4.3.1 Uncertainties in Bouguer anomalies

The main uncertainty in computing Bouguer anomalies is overestimation of average densities. The assumption that the mean crustal density is 2670 kg/m^3 may not be correct for the Kii Peninsula crust. This would then effect the values of the gravity anomalies.

4.4 Slow earthquake catalogs

The time-lapse modelling uses slow earthquake information from three catalogs to constrain areas of interest. These catalogs are defined by Nakano et al. (2016), Masaru Nakano, Hori, et al. (2018), Sugioka et al. (2012) and Takemura, Matsuzawa, Noda, et al. (2019). The earthquakes studied by Nakano et al. (2016),Masaru Nakano, Hori, et al. (2018) and Takemura, Matsuzawa, Noda, et al. (2019) are located using a centroid moment tensor (CMT) inversion method, while Sugioka et al. (2012) use moment tensor inversion. CMT inversion gives the average location of the seismic energy release in space and time as well as the moment tensor, rather than the point of origin of the earthquake, which is found through moment tensor inversion (Stein, Wysession, and Houston 2003). CMT uses both the body waves and the surface waves within the seismogram to locate the earthquakes, while moment tensor inversion generally involves either body waves or surface waves (Stein, Wysession, and Houston 2003).

The catalogs define VLFE episodes, all located between the toe of the accretionary prism and the upper limit of the Tonankai fault region. From here, an episode is defined as a set of VLFEs occurring over a fairly continuous duration.

The earthquake catalog by Nakano et al. (2016) and Masaru Nakano, Hori, et al. (2018) include two separate episodes from 2015 and 2016. The catalog defined by Sugioka et al. (2012) include events from 2009. The last catalog, by Takemura, Matsuzawa, Noda, et al. (2019)), includes several VLFE episodes from June 2003 to May 2018. The complete catalogs containing the episodes used for the analysis can be found in Appendix C, Section C.1. The following sections will discuss each earthquake catalog separately. The modelling involves parts of the episodes defined by the different catalogs. A summary of the entire VLFE episode chosen from the catalogs is given in Table 4.4.

Year	2004	2009	2009	2015	2016
Catalog	[3]	[2]	[3]	[1]	[1]
Number of events	539	12	197	56	318
Date	May 17. - December 27.	March 24.-28.	March 24. - July 11.	August 10.- October 27.	April 1.-28.
Duration (days)	48	5	34	17	20
Mangitude	3.27-4.73	3.8-4.9	3.19-4.52	3-4.3	2.2-4.1
Depth range (km)	4.88 - 9.27	5.2 - 11.6	4.88 - 8.9	5 - 30	3 - 19
Mean depth (km)	6.04	7.4	6.48	8.75	6.97

Table 4.4: Summary table of the episodes within the three catalogs that are used for the modelling. The duration indicates the number of days in which the episodes occurred. The number of events is indicated for the entire episode, while only some of these events are considered in the modelling. Source catalogs: 1: Masaru Nakano, Hori, et al. (2018) and Nakano et al. (2016), 2: Sugioka et al. (2012), 3: Takemura, Matsuzawa, Noda, et al. (2019).

Figure 4.7 shows the location of all the earthquakes defined for each episode given in the catalogs.

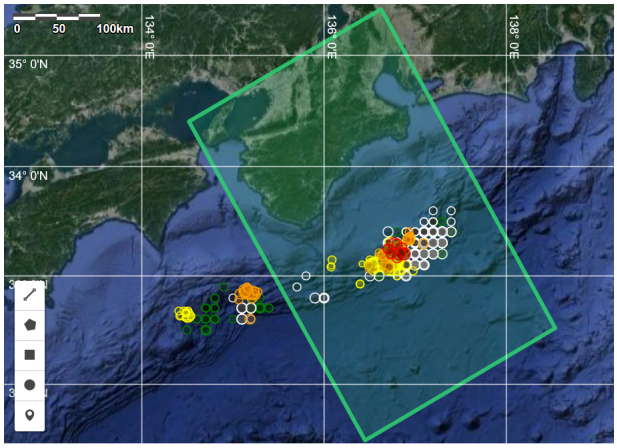

Figure 4.7: Location of VLFE episodes from all catalogs. The colors indicate which catalog each VLFE is located in. White: 2004 episode defined by Takemura, Matsuzawa, Noda, et al. (2019), Green: 2009 episode defined by Takemura, Matsuzawa, Noda, et al. 2019, Red: 2009 episode defined by Sugioka et al. (2012), Orange: 2015 episode defined by Masaru Nakano, Hori, et al. (2018) and Nakano et al. (2016), Yellow: 2016 episode defined by Masaru Nakano, Hori, et al. (2018) and Nakano et al. (2016). The scale factor is set to 1.2, and the size of the bubbles indicate the magnitude of the event. The magnitudes range from M_w2.2 to M_w4.9. (Source: D-map (2019))

4.4.1 Catalog by Masaru Nakano, Hori, et al. (2018) and Nakano et al. (2016)

The catalog of VLFEs defined by Nakano et al. (2016) and Masaru Nakano, Hori, et al. (2018) consists of 375 VLFEs occurring between August 10. to October 27., 2015 and April 1.-28., 2016. The VLFES range in magnitude between 2.2 and 4.1, and are located at depths of 3 to 30 km below sea level. The total moment release of the episodes from 2015 and 2016 is estimated at 5×10^{15} Nm and 2.9×10^{16} Nm, respectively (Masaru Nakano, Hori, et al. 2018). The estimation is done for events of $M_w \geq 3$.

Waveforms are obtained through broadband seismometers within the DONET network (Masaru Nakano, Hori, et al. 2018). Most events within the 2016 episode showed thrust fault mechanisms, located at around 6-9 km depth. However some deeper events showed strike-slip mechanism (Masaru Nakano, Hori, et al. 2018). The events deeper than 10 km have larger uncertainties in depth location than the shallower events. Properties of the events used for the modelling are given in Table 4.5.

Since the estimated depth uncertainty is larger for the deeper VLFEs, only VLFEs shallower than 15 km depths have been used in the gravity modelling. A test is presented in Chapter 5.4.2 and 6.2.2, showing how much the results differ when including or excluding the events down to 15 km depths.

Year	2015	2016
Duration	August 10. - October 29.	April 1. - 28.
Number of events used	23	279
Depth (kmbsl)	5 - 15	3 - 15
Magnitude	3 - 3.9	2.2 - 4.1

Table 4.5: Data for VLFE events taken from the 2015 and 2016 episodes as defined by Masaru Nakano, Hori, et al. (2018) and Nakano et al. (2016).

4.4.2 Catalog by Sugioka et al. (2012)

The VLFEs occurred in March 2009, and were detected by three broad band OBSs (Sugioka et al. 2012). 12 events occurred between March 24. to March 28, and moment tensor inversion with a grid search was used to obtain focal mechanisms, location and source time functions of the events (Sugioka et al. 2012). For the moment tensor inversion, they used a 3D P-wave velocity over the accretionary prism and Philippine plate by Nakanishi, Kodaira, Miura, et al. (2008).

The moment tensor inversion produces low angle thrust fault mechanisms for the VLFEs, with magnitudes ranging from M_w 3.8 to 4.9, located at 5.2 - 11.6 km depths (Sugioka et al. 2012). The events are summarized in Table 4.6. Sensitivity studies on the VLFE locations show that they likely occur along the base of the accretionary prism (Sugioka et al. 2012). However, the location is not accurate enough to determine if they occur at the interface or within the accretionary prism (Sugioka et al. 2012).

Year	2009
Duration	March 24. - 28.
Number of events used	12
Depth (km)	5.2 - 11.6
Magnitude	3.8 - 4.9

Table 4.6: Data for VLFE events taken from 2009 episodes as defined by Sugioka et al. (2012).

4.4.3 Catalog by Takemura, Matsuzawa, Noda, et al. (2019)

The entire catalog by Takemura, Matsuzawa, Noda, et al. (2019) covers a period between June 1., 2003 to May 31., 2018, and a total of 942 events. The catalog is gathered by studying previous onshore records of VLFE activity off the Kii Peninsula, using seismograms from 15 years obtained through the onshore F-net seismic

stations (Takemura, Matsuzawa, Noda, et al. 2019). The centroid locations, given in Figure 4.8, are located beneath the accretionary prism, assumed to be on the Philippine plate boundary (Takemura, Matsuzawa, Takeshi Kimura, et al. 2018, 2019a).

To conduct the CMT inversion, a detailed S-wave velocity model of the accretionary prism created by Takemura, Kubo, et al. (2019) was used, combined with a model of the Philippine plate by Koketsu, Miyake, and H. Suzuki (2012) (Takemura, Matsuzawa, Noda, et al. 2019). The 3D S-wave model uses S-wave profiles from the DONET stations found by Tonegawa et al. (2017), making this a reliable model within this region (Takemura, Matsuzawa, Noda, et al. 2019, Takemura, Kubo, et al. (2019)). By comparing synthetic and observed seismograms, variance reduction (VR) was found, and CMT solutions with VR greater than 20% were chosen (Takemura, Matsuzawa, Noda, et al. 2019). The source locations for the 2009 VLFEs determined by Takemura, Matsuzawa, Noda, et al. (2019) were verified by comparison to the 2009 events located by Sugioka et al. (2012).

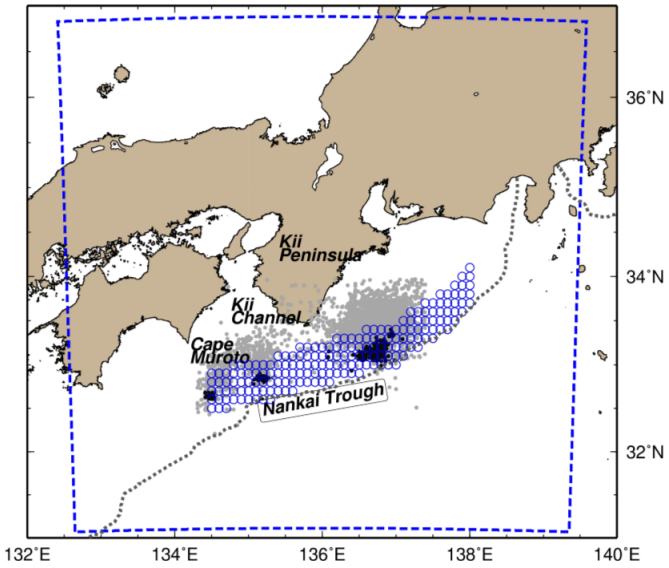

Figure 4.8: Location of centroid grid used for locating the VLFEs. Gray dots are epicenter locations determined by onshore stations, while black dots are the 2015 and 2016 episodes located by offshore DONET stations. The blue circles indicate the grid location. (Source: Takemura, Matsuzawa, Noda, et al. (2019))

The results indicate that VLFEs occurred along thrust faults, where strike angle of the mechanisms were observed to be parallel to the trough axis, suggesting rupture along the plate boundary (Takemura, Matsuzawa, Noda, et al. 2019). The seismic moment for the events are evaluated within the source grids, giving a cumulative moment for several events at each grid point. The estimated total seismic moment release from the 2004 and 2009 episodes is around 5×10^{17} Nm and 1.5×10^{17} Nm, respectively (Takemura, Matsuzawa, Noda, et al. 2019). The region covered by these

events experienced a total moment release of 6.8×10^{17} Nm during the whole 15 year period (Takemura, Matsuzawa, Noda, et al. 2019).

The episodes used in the modelling occurred in 2004 and 2009, and the events used for the modelling are given in Table 4.7. These episodes are used due to the extensive amount of events occurring within this time frame, and in order to compare the 2009 episodes by Sugioka et al. (2012) with the ones from this catalog.

Year	2004	2009
Duration	September 6. - 30.	March 24. - April 28.
Number of events used	332	141
Depth (km)	4.88 - 9.03	4.88 - 8.49
Magnitude	3.27 - 4.54	3.35 - 4.54

Table 4.7: Data for VLFE events taken from the 2004 and 2009 episodes as defined by Takemura, Matsuzawa, Noda, et al. (2019).

4.4.4 Uncertainties in VLFE location

For the earthquake catalog by Nakano et al. (2016) and Masaru Nakano, Hori, et al. (2018), the uncertainty in the horizontal locations of the events are 5 km. The vertical uncertainties for events shallower than 10 km depth are ±2 km, while the deeper locations have larger uncertainties. Figure 4.9a,b shows a cross section of the velocity model, indicating error bars for some of the 2015 and 2016 VLFE episodes.

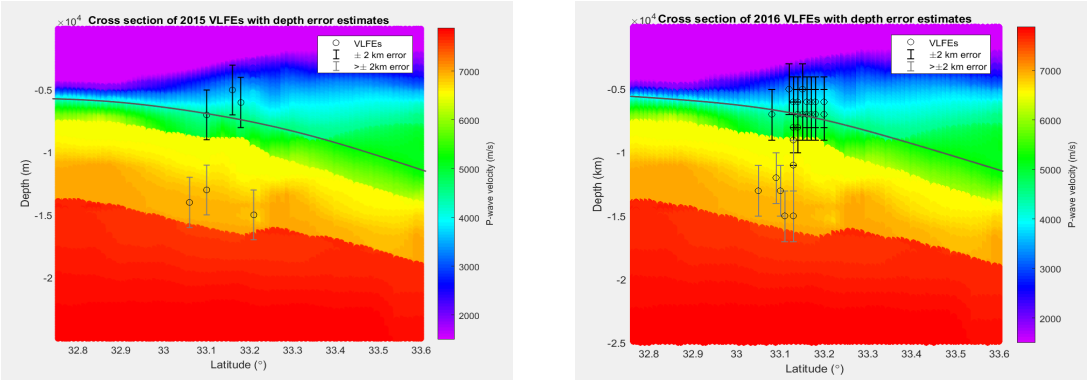

(a) Error bars for 2015 episode.

(b) Error bars for 2016 episode.

Figure 4.9: Depth uncertainties for the 2015 and 2016 episodes, estimated by Masaru Nakano, Hori, et al. (2018). The velocity cross section is taken at 136.65° longitude, crossing the model from south to north. The events are within ±0.05° of the cross section. The line indicates the boundary of the plate interface.

For the catalog by Sugioka et al. (2012), minimizing the difference between the synthetic and observed seismograms showed that the difference was larger for depths

over ±800 m from the assumed source grid. Hence, solutions within ±800 m give a good result, reflecting the uncertainties in depth estimation for these events. Uncertainties in the horizontal placement of the events are within $< \pm 4$ km. The depth uncertainties to some of the analyzed VLFEs are given in Figure 4.10.

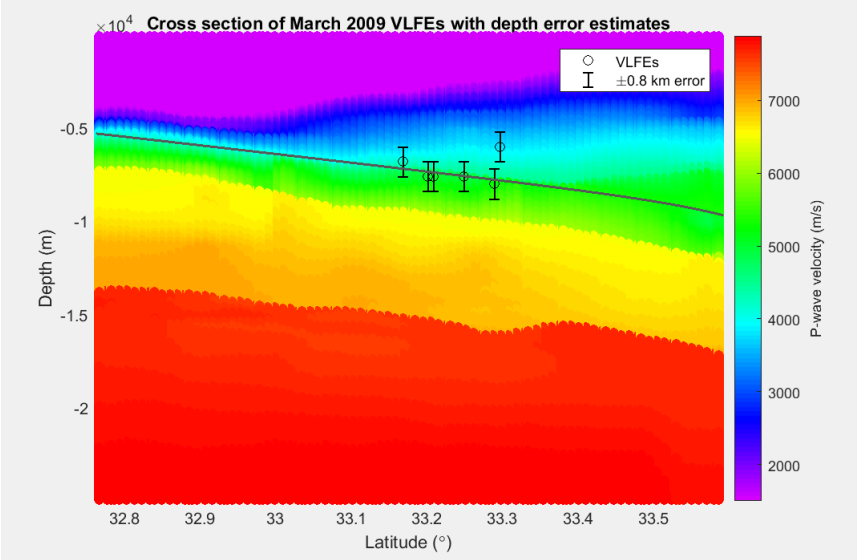

Figure 4.10: Depth uncertainties for some of the 2009 VLFEs, estimated by Sugioka et al. 2012. The velocity cross section is taken at 136.8° longitude, crossing the model from south to north. The events lie within ±0.05° of this cross section. The line indicates the boundary of the plate interface.

The catalog defined by Takemura, Matsuzawa, Noda, et al. (2019) shows some uncertainties in location due to the use of seismograms from onshore stations (Takemura, Matsuzawa, Takeshi Kimura, et al. 2018). Using the onshore seismograms, Takemura, Matsuzawa, Takeshi Kimura, et al. (2018) tested the effect of a deeper or shallower source grid for the CMT inversion, and noted that adjusting the depth with ±2 km had little impact on VR estimations, although moving them 2 km deeper gave a slightly worse fit to the observed seismogram. However, when comparing events from their defined 2016 VLFE episode with seismograms from the DONET stations, the VR estimates became worse if the grid was moved away from the plate interface. Therefore, the best fit was achieved when the source grid was located on the interface, which is the basis for their assumption of placing the centroid grid here (Takemura, Matsuzawa, Takeshi Kimura, et al. 2018). Based on this, the estimated depth uncertainties to the VLFE locations is defined as ±2 km, which is shown in Figure 4.11.

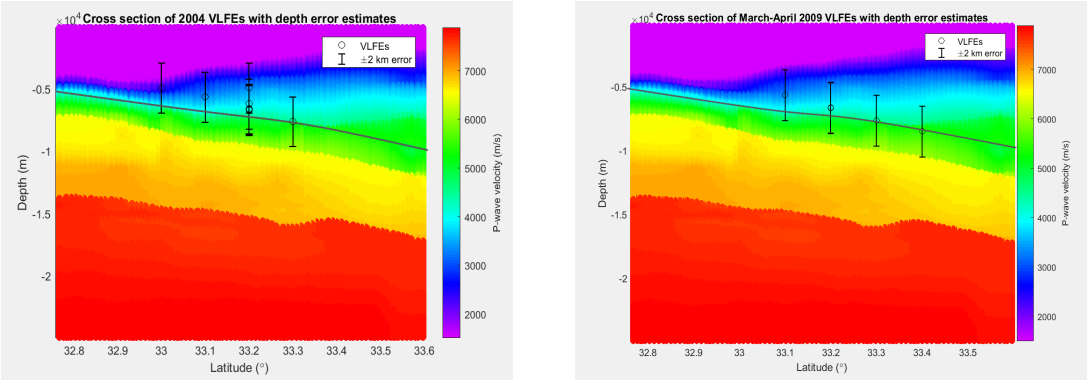

(a) Error bars for 2004 episode.

(b) Error bars for 2009 episode.

Figure 4.11: Depth uncertainties for the 2004 and 2009 episodes, estimated by Takemura, Matsuzawa, Noda, et al. (2019). The velocity cross section is taken at 136.8° longitude, crossing the model from south to north. Both sets of VLFE events are within ±0.001° of the cross section. The line indicates the boundary of the plate interface.

4.5 Slip-deficit rate distribution

Geodetic measurements have been used extensively in subduction zone research (e.g. T. Ito, Yoshioka, and Miyazaki 1999; Hirai and Sagiya 2013). Slip rates on the plate interface are a major factor in determining the asperity distribution along the megathrust fault, and can give information on coseismic fault slip. This can be inferred from inversion of geodetic measurements. Here, measurements from GPS stations are used to determine slip-deficit rate distributions on the plate interface, or the difference between the inferred slip caused by steady movement of the plate and the actual slip due to locking in certain areas (Hirai and Sagiya 2013).

Slip-deficit rates have been determined by Yokota et al. (2016), using inversion of geodetic measurements from GPS stations both onshore and offshore through the JHOD network. The network consist of 15 GPS stations distributed across the seafloor (Yokota et al. 2016). This study therefore gives a highly detailed distribution of slip-deficits within the offshore regions of the Nankai trough. Only raw data from stations installed after the 2011 Tohoku earthquake were used, to reflect steady movement of the plates and no excess slip caused by the earthquake (Yokota et al. 2016). Regions with high slip-deficit rates coincide well with the fault rupture slip distribution of the Tonankai earthquake (Yokota et al. 2016). The slip-deficit rates are shown in Figure 4.12, and two asperities are clearly seen located off the Kii Peninsula, within the source region of the 1944 megathrust earthquake.

The results show patches of high slip-deficit rates within the Nankai trough, and areas of low rates corresponding to subducted ridges and VLFE distributions (Yokota et al. 2016). The exact location and size of values used to determine the slip-deficit rates of Figure 4.12 are given in Table C.8 of Appendix C. The data include geo-

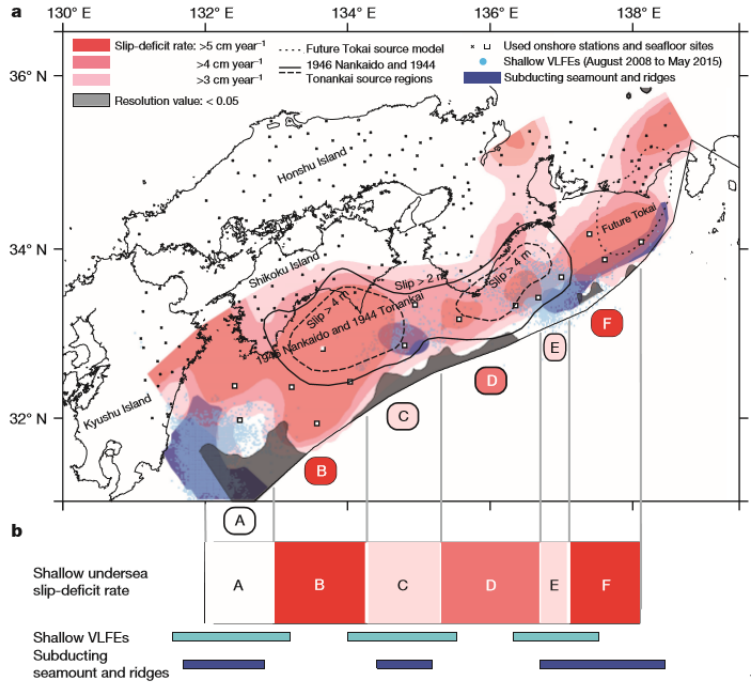

Figure 4.12: Distribution of slip-deficit rates within the Nankai trough. Blue dots indicate VLFEs between 2008 and 2015. The solid and dashed lines indicate the fault segments ruptured by the 1944 Tonankai and 1946 Nankai earthquakes. Dark blue areas indicate locations of subducted ridges and seamounts. (Source: Yokota et al. (2016))

graphical coordinates of the region covering the entire Nankai trough, excluding the region closest to the trough axis. The slip-deficit rates are given in m/yr.

The slip-deficit rate distributions have been included for visualization purposes, to compare slow earthquakes distribution with the inferred slip on the plate interface.

4.5.1 Uncertainties in slip-deficit rate distribution

Uncertainties in the slip deficit rate is found for two standard deviations, 2σ, to be 0.3 cm/yr for onshore data and 1.5 cm/yr for offshore data, and combining results from both onshore and offshore data gave the best results (Yokota et al. 2016). Regions near the trough could not be resolved accurately due to lack of stations there (Yokota et al. 2016).

4.6 DONET network

One of the most recent monitoring system at the Nankai trough was developed by JAMSTEC's Department of Oceanfloor Network System Development of Earthquakes and Tsunamis in 2006 (JAMSTEC 2019b), and is operated by JAMSTEC and the National Research Institute for Earth Science and Disaster Resilience (NIED)

(Takemura, Matsuzawa, Takeshi Kimura, et al. 2018). Deployment of the DONET1 observatories on the seafloor off the Kii Peninsula was completed in 2011, and the observatories were in operation by August 2011 (Ariyoshi et al. 2014). A second set of observatories, DONET2, started construction in 2010, and the deployment off the southeastern Shikoku island was completed in 2016 (JAMSTEC 2016). DONET2 covers the western part of offshore Kii Peninsula, and together with DONET1 gives almost complete coverage of the off-Kii Peninsula area. Figure 4.13 gives the location and placements of the DONET1 and DONET2 observatories.

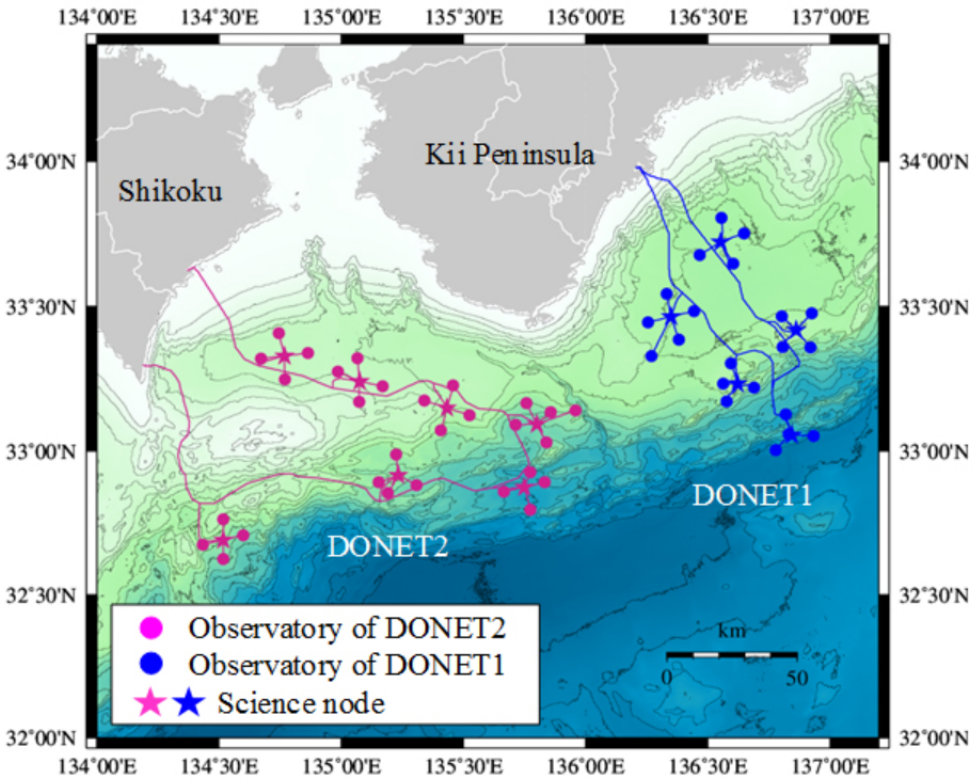

Figure 4.13: Placement of all DONET observatories and science nodes on the seafloor of the Nankai trough accretionary prism. (Source: JAMSTEC (2016))

The DONET1 network over the Kumano basin and accretionary prism consists of five nodes (labelled A-E), each branching out in four observatory positions. The coordinates of the nodes and observatory stations for the DONET1 network are provided in Appenix C.2, Tables C.6 and C.7. The data does not include the DONET2 network as it lies outside of the studied region off the Kii Peninsula. Instruments within the network include OBSs, pressure sensors, hydrophones and thermometers, with a detection limit of $M_w 0.8$ for observing earthquake activity (Masaru Nakano, Nakamura, et al. 2013). This network has therefore been very important in obtaining detailed information on earthquake activity near the trough off the Kii Peninsula.

The locations of DONET1 observatories are included to relate the time-lapse gravity values to this network, both for visualizing where the gravity changes occur in the trough, and to relate the DONET1 observatories to locations of high time-lapse gravity values found in the modelling.

Chapter 5

Analysis

The analysis first involves creation of the density map, based on the 3D P-wave velocity model and geological information on the area. The velocity model is dived into an overriding island arc crust and a descending oceanic crust. A total of 12 layers are created, based on distinct layers found in the velocity model. Once the layers are created, with corresponding rocks and their physical and geological properties, the density map can be created. Specific velocities within the 3D velocity model are assigned to each layer, and the densities are estimated based on the rock types in the geological model.

The density map is then discretized to a 3D distribution of rectangular prisms, all with a predefined lateral extent and heights and depths in the model defined by studying individual density profiles. These prisms are used in the forward modelling of gravity, following the methods described in Chapter 3.2. An absolute gravity computation is conducted, and with this Bouguer anomalies are modelled. The Bouguer anomaly modelling is done to compare with Bouguer anomaly maps provided by the GALILEO Gravity database (Geological Survey of Japan 2019), to validate the density map.

The time-lapse gravity modelling follows the three separate scenarios introduced in Chapter 3.2.2. The three scenarios are created to model fluid migration within the accretionary prism and along the plate interface. The scenarios assume slow earthquakes within this region are triggered by fluid migration, creating a temporal gravity change within the shallow reaches of the Nankai trough.

The following sections discuss the steps taken to obtain the results throughout the project, where first the process of creating the density map and the 3D distribution of rectangular prisms is discussed, then the Bouguer anomaly modelling will be presented. The last section includes the gravity modelling, where the different modelling scenarios mentioned in Chapter 3.2.2 will be discussed in more detail.

5.1 Creating the density map

The geological model is created by first dividing the velocity model into layers, and defining which rock types to use for each layer. Next, a mineral composition and typical physical properties of these rock types are defined, along with the maximum and minimum velocity to include in each layer. To define the physical properties of the rocks, theoretical densities of each rock type needs to be used to make sure the estimated values lie within reasonable ranges. Mean density values, given in Table 5.1, are used for comparison with the estimated rock densities.

Rock type	Theoretical mean density (kg/m^3)
Unconsolidated sediment	1800 [1]
Mudstone	2350 [1]
Sandstone	2350 [2]
Limestone	2500 [2]
Basalt	2850 [2]
Gabbro	2900 [2]
Peridotite	3200 [2]

Table 5.1: Mean densities of the rock types used for the creation of the geological model. [1]: Mussett and Khan (2000), [2]:Schön (2015).

Although the mean values of Table 5.1 are used to decide if the estimated densities for each rock are within reasonable ranges, it is important to note that the real values vary with depth, fluid saturation, and mineral composition (Schön 2015). Therefore, the actual mean values are highly variable, and the theoretical mean values are not used as an absolute mean density for the layers.

The starting velocity ranges discussed in section 4.2 (given in Tables 4.1 and 4.2) are defined by first applying the density conversion to a rough model, using the original ranges provided by Nakanishi, N. Takahashi, Park, et al. (2002) and Nakanishi, N. Takahashi, Yamamoto, et al. (2018). The converted density map reveals where more refinement is needed for the velocity ranges, i.e. if any individual layers in the 3D density model are represented incorrectly in the density map. This is done in several ways:

- Studying individual profiles comparing velocities with the resulting densities
- Studying cross-sections comparing velocities and densities
- Trial and error for the density estimation using specified velocity ranges compared to the theoretical mean densities, revealing if too wide velocity ranges

are chosen

Cross-sections of the velocity model and density map are compared to observe if the conversion approximately replicates the same layered structure. Layers that are off are then adjusted, and tested again. Mostly, individual depth profiles of velocities and densities from -4 km to 60 km depths are chosen at various locations in the model for comparison. This process also involves altering the geological model throughout the analysis, for instance if changes in the velocity range of the rock create large deviations from the mean value. The deeper layers (e.g. the upper mantle and the lower crust) have significantly higher velocities compared to other layers, and are therefore simpler to define than the rest of the model due to significant velocity contrasts between layers. However, the areas above and below the plate interface are of great importance to study in more detail, as these layers are more difficult to define owing to partly overlapping velocity ranges.

As discussed in Chapter 3.1.2 in relation to the empirical density equation, Eq. 3.5, each estimated density value is based on the maximum and minimum velocity defined for the rock type, its effective bulk and shear modulus and the individual velocity values of the 3D model corresponding to the layer represented by this rock type. To group the 3D velocities, a function is created in which all velocities and their corresponding indices in the velocity array are placed in a group relating to a certain layer. In this way, each layer can be isolated and studied individually, and the effect of the rock properties on the estimated density range of the layer is easier to observe.

The geological model is separated into an oceanic crust section and an island arc crust section, and the layers within are studied separately. This division is important to distinguish between the surface of the descending plate and the overriding upper island arc crust and accretionary prism. Dividing the model into two sections allows for layers of similar velocity ranges but different compositions to be accurately chosen for the density estimation. In particular, defining the upper layer of the oceanic crust, the basalt layer, is important to get an accurate representation of the separate layers of the geological model. Studying the 3D velocity model in detail reveals that this layer has a highly variable velocity range, from 4520 to 6500 m/s in some areas. The minimum and maximum velocity for this layer therefore overlap the ranges given for the sandstone, limestone, island arc basalt and both the gabbro layers, highlighting the importance of isolating this layer to get a good representation of the geological model.

The method used to find the velocity indices corresponding to the layers is based on the fact that the lower gabbro and peridotite layers included fairly high velocities with uniform velocity increase, as seen in Figure 5.1. It is therefore simpler to define the three layers of the Philippine plate before the other layers are assigned velocity values. The function parses through each individual velocity profile from the velocity

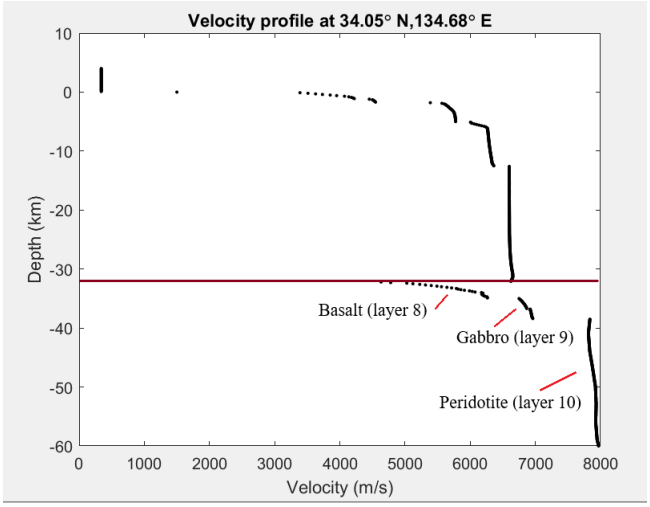

Figure 5.1: Example of a profile from the velocity model. The line indicates the division between the layers corresponding to the descending Philippine plate velocities (bottom) and the layers corresponding to the overriding Amur plate (top).

value at 60 km depth and up, dividing the velocity values corresponding to specified velocity intervals into lists. This way, the bottom two layers are identified first, then the upper layer of the descending plate, the basalt layer, is defined within the velocity model. This layer is allowed a maximum thickness of 2 km, further constraining the layer and separating its corresponding velocities from similar velocities above. After the three layers of the oceanic plate are defined, the rest of the model is simple to divide due to no overlapping velocity ranges within the overriding plate. Thus, layers of similar composition in the descending Philippine and overriding Amur plates are not mixed together. The introduction of the velocity indices corresponding to each layer solves the problem with the overlapping velocity ranges.

To compute the estimated densities, a MATLAB (MathWorks inc. 2018) structure is defined. This structure follows the layering of Figure 4.2b in Chapter 4.2, including the first two layers in the velocity model which consist of air and water velocities. A total of 12 layers are defined, where the first two comprise the air and ocean layer, and the following 10 layers are defined by the geological model. In addition to the predefined velocity ranges of the layers, the structure includes the effective elastic moduli and porosity of each rock type, the conversion factor α from the empirical relation in Eq. 3.5, and indices of the velocity values corresponding to each layer. The indices are used directly in the density conversion to define which layer and rock parameters to use for a set of velocities in the 3D model. The MATLAB functions used for creating the structure of rocks and their properties and computing the density values are given in Appendix A.

With the mean density values of Table 5.1 as a base, the mineral properties and porosity of the chosen rock types are refined. For rocks where porosity values can

be defined directly by studying IODP drill reports, a porosity value approximately corresponding to these known values or ranges is used in the model, and slightly refined in layers where over- or underestimation of densities is observed. For the lower layers, where porosities are unknown, the theoretical mean density values are the basis for deciding the porosity value.

To include the effect of porosity on the bulk density of the rock, the Hashin-Shtrikman boundaries are used to define effective moduli of each rock layer. By introducing the porosity values in the computation, more reasonable densities can be estimated for the porous rocks. A test is conducted on the density estimates, where porosities are altered and the effect of the porosity on the density estimation is evaluated. Through this test, it is determined that a change in porosity of 0.01 from the original value (i.e. $\Delta\phi = 0.01$, in fractions), leads to an approximate change in mean density of 2% relative to the original density value. If the porosity is altered, the new mean density can be defined approximately by the following relation:

$$\overline{\rho}_{new} = \overline{\rho_0}(1 - 2\Delta\phi)$$

Where $\overline{\rho_0}$ is the original mean density for the layer with the original porosity ϕ_0, $\overline{\rho}_{new}$ is the new mean density, and $\Delta\phi$ is the change from the original porosity, $\Delta\phi = \phi_{new} - \phi_0$. This is an empirical relation based on varying porosity values, and gives an idea of how sensitive the bulk density of the rock is to porosity changes. For instance, if the porosity of the oceanic gabbro layer (layer 11) is changed from 10% to 13%, the new mean density is reduced by approximately 6% - from a mean density of 3060 kg/m^3 to a mean of 2876 kg/m^3. If the porosity value for this layer were to be reduced to a lower value than 10%, which might reflect actual porosities in an oceanic gabbro layer, this would create a large bulk density for this layer compared to realistic values. Thus, the chosen porosity values are based on the mean densities in Table 5.1, and are not refined much further to reduce the number of assumptions made to the geological model.

Even though the density values are quite sensitive to porosity changes in the model, the most sensitive parameter to the density estimation is the rock mineral composition. Assuming a mono- or dimineralitic rock is a necessary simplification when the actual parameters are not well known, as to not introduce more uncertainties by assuming a more variable composition. However, the wrong mineral may result in highly unrealistic density estimates for the given rock type. For instance, if only one of the minerals representing the basalt layers are chosen, the resulting mean density is determined to vary between 1620 kg/m^3 and 5007 kg/m^3 for the oceanic basalt layer, depending on if the feldspar mineral or the augite mineral is used. To lower the highest density to a more realistic mean value would then require adding a much higher porosity value, leading to even more unrealistic rock parameters.

When choosing the appropriate minerals to use for the rock properties, an important step is to find realistic mineral compositions for the different rock types that also accounts for realistic density estimates. The appropriate mineral compositions are chosen by trial and error for the layers where the composition is not known through IODP drill cores. Thus, the final mineral composition of the geological model is determined by common minerals found in the different rock types, along with how realistic the porosity and resulting density values are in combination with this mineral.

	Effective modulus	
Layer	Bulk modulus (GPa)	Shear modulus (GPa)
Air	2.3×10^{-12}	0
Ocean	2.34	0
1	4.95	1.29
2	8.35	4.28
3	21.26	9.21
4	41.85	19.62
5	54.15	29.05
6	76.27	46.81
7	105.19	65.69
8	45.68	24.72
9	76.27	46.81
10	105.19	65.69

Table 5.2: Effective bulk and shear modulus used for all layers in the geological model.

After the geological and physical properties are refined, the final Hashin-Shtrikman upper bounds that give the best fit between theoretical rock densities and the density estimation are defined. The computed effective rock moduli are given in Table 5.2. For the rocks where two dominant minerals are chosen, a fraction of $f_i = 0.5$ is defined for each mineral in the Hashin-Shtrikman equations 3.3a,b.

The final density conversion is shown in Figure 5.2, compared to the P-wave cross-section of Figure 4.2a presented in Chapter 4.2:

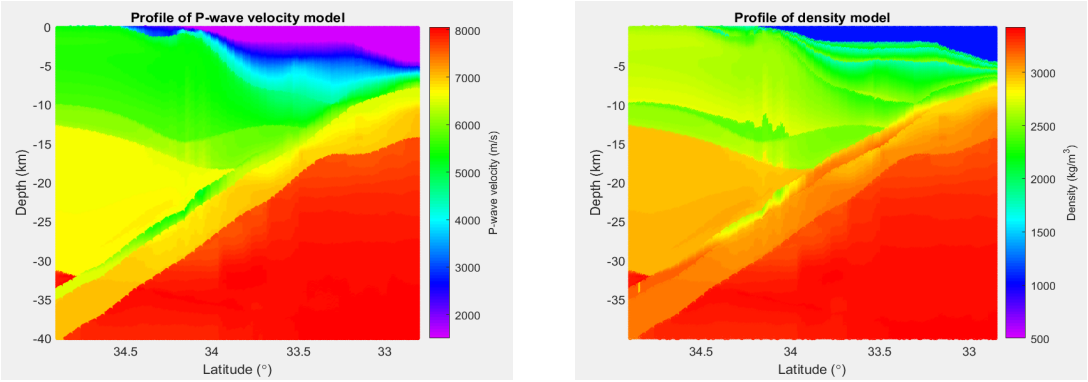

(a) Velocity model

(b) Final density model

Figure 5.2: Comparison of a cross-section of the 3D velocity model with a cross-section of the density map. The cross-sections are taken at 136.5° longitude, covering the area from north to south.

5.2 Discretizing the density map

To conduct the gravity modelling, the density map first needs to be divided into rectangular prisms, which are then used for the gravity computation following the method discussed in Chapter 3.2. The prisms will hereafter be referred to as boxes. The 3D velocity model includes coordinates in latitude and longitude, depth and P-wave velocities. To divide the values into separate boxes, the geographical coordinates first need to be converted to Cartesian coordinates. This is done through a conversion tool provided by OCTIO Gravitude on conversion from geographical coordinates to Transverse Mercator coordinates, creating a Cartesian map projection with outputs given in meters. Following the steps given in Chapter 3.2, the density distribution is discretized in boxes based on density variations within each layer, and a predefined horizontal extent dx and dy for each box.

The measurement points are based on the 2D surface coordinates of the 3D velocity model. The original order of the points is shown in Figure 5.3. These points are rearranged to a regular grid with a predefined spacing through interpolation. Through Delaunay triangulation, irregular grid points are connected by lines in a triangular pattern, allowing for connections between the points lying within the triangulated points to be made. First, the original 2D values are interpolated to a regular grid using scatter interpolation. Once a regular grid has been created based on the original coordinates, triangulation is done on the 2D grid points of the 3D velocity model, and this triangulation is used to find points within the regular grid that are nearest the original grid points, thus creating a regular grid based on the original points of the velocity model.

The division of the 3D density map into boxes is an important step before conducting the gravity modelling, as these need to correspond well to the initial density map to obtain accurate gravity values. To achieve good lateral resolution of the

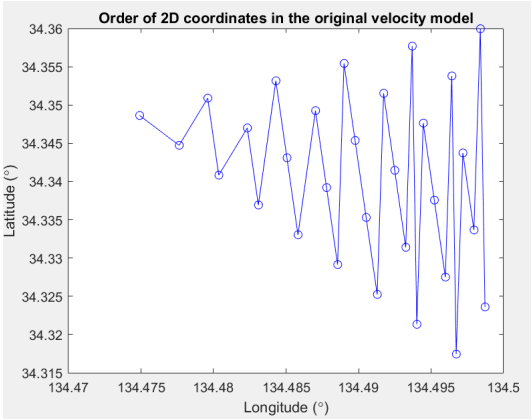

Figure 5.3: Plot of the 30 first 2D grid points in the 3D velocity model. The points or connected by a line indicating the order in which the points are placed in the original model.

density variations within the model, the horizontal extent of the boxes cannot be too large. By trying different box sizes starting at 3×3 km, the length of 1.5×1.5 km is determined to give a satisfactory resolution of the 3D model. The first density value included within each box defines which layer the box lies within. The tolerance between this first density value and the following density values is chosen as ±5%, meaning that densities within ±5% of this initial value are grouped together and corresponded to the same box. The mean density of these values is used as the density for the entire box.

Layers with small density variations with depth are discretized to fewer boxes. For instance, the peridotite layers have a low variability in individual profiles between the top and the bottom of the layer, as seen in Figure 5.1, and most of the layer in the separate profile can be defined in one box. This results in some boxes with vertical extents of more than 40 km. In contrast, some of the shallower layers included boxes of only 100 m heights. The minimum height of a box in the model is around 100 m due to the spacing of the depth points at 100 m intervals. Hence, a high variability is found for the extent of the boxes in the entire model, which is accounted for when conducting the time-lapse analysis on individual boxes. Discretizing the boxes in this way reduces the number of boxes needed to represent the density map, and therefore the computation time when computing the corresponding gravity signal from the box distribution.

The tolerance of the densities included in each box is based on how well layers of different rock types are separated when in the model. If the tolerance is too high, different rock types of similar densities are all placed within the same box, which makes it difficult to separate individual layers to use for the modelling. This brings back the issue with separating layer 8 in the box discretizaion as well, considering that the overlapping velocity ranges also creates some overlapping densities. For

the time-lapse modelling, it is therefore especially important that all the boxes corresponding to the basaltic layer of the Philippine plate are placed in the correct layer to reflect a relatively continuous plate interface. Thus, a fine tolerance of ±5% is necessary to make sure the boxes follow the structure of the plate.

To make sure the boxes give an accurate representation of the density model, they are all given a number 1-12, corresponding to the layer they represent. In this way, boxes corresponding to certain layers can be studied individually to make sure the layers are chosen correctly. This also makes it easier to choose certain layers to use for the time-lapse gravity modelling without needing to use the entire model. Thus, each individual box is defined by its horizontal and vertical extent (i.e. the position of each corner of the box), the mean density of the section of the density profile encompassed in the box, and which layer it lies within.

When discretizing the density map, the coordinates of the seafloor are also extracted. The depth of the seafloor is assumed to be located where the densities change from <1100 kg/m^3 (corresponding to the ocean layer) to above 1100 kg/m^3, where densities from seafloor sediments are found. Considering that this density variation is found above the Kii Peninsula topography as well, coordinates cover the entire area, not just the sediments below the ocean layer. The resulting seafloor depth coordinates are used to determine depths of measurement points used for the time-lapse analysis and the depth of the oceanic layer in the Bouguer anomaly estimation. The resulting seafloor depths are given in Figure 5.4, showing the area used for the time-lapse analysis. The DONET1 observatories are located along the seafloor of the model.

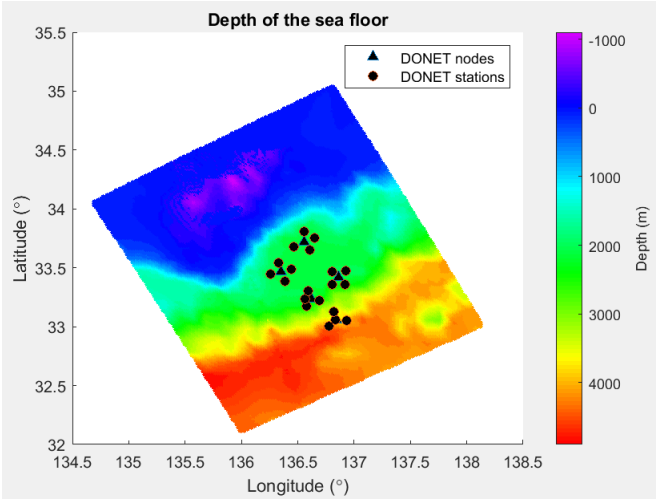

Figure 5.4: Depth of the seafloor estimated from density variations between the ocean and the seafloor sediments. The DONET1 observatories are shown, located along the seafloor. The seafloor depth is given relative to sea level. Some coordinates are chosen above the Kii Peninsula (indicated by depths of ≤ 0), which indicates sediments above sea level ($z = 0$) covering the Kii Peninsula.

5.3 Absolute gravity modelling

The complete gravity model is computed using a 1.5×1.5 km horizontal grid spacing for the surface measurement points. The absolute gravity values are computed for the entire model, shown in Figure 5.5. The maximum obtained gravity for the entire model is around 6000 mGal, or 0.06 m/s^2.

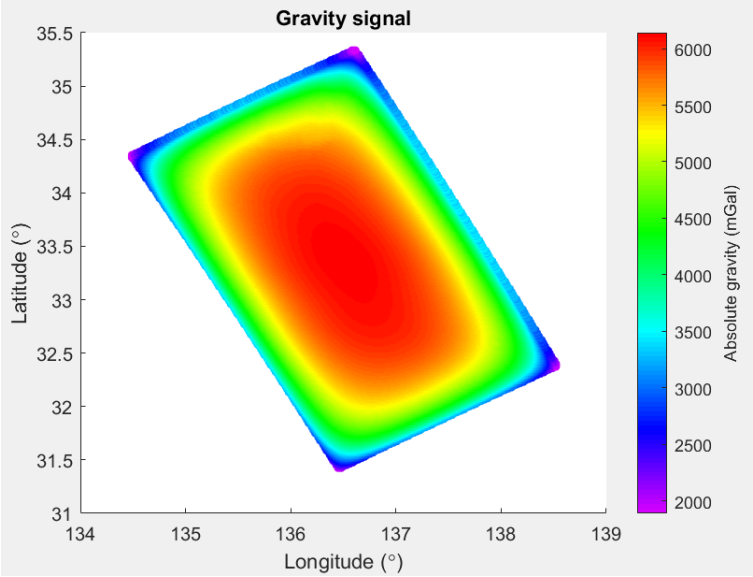

Figure 5.5: Gravity computed for the entire study area.

The absolute gravity plot is difficult to analyze due to the boundary effects seen in Figure 5.5. This effect is caused by the solid angle, which leads to an underestimation of the values at the edge of the model due to fewer boxes influencing the gravity signal here. This issue is prominent in the Bouguer anomaly plots. In particular, the deepest layers with large densities have a great effect on the modelled absolute gravity values.

The solid angle affects the measurement points within a conical region below the point, where the radius of the base of the cone increases with depth. Thus, boxes in the deeper regions will affect a measurement station in a wider radius, causing larger boundary uncertainties. The measurement points at the center of the model will therefore have a larger absolute gravity value than the measurements at the edge of the region, where only half as many boxes are used for the gravity computation. The absolute gravity value at the measurement points is steadily reduced towards the edge of the region, as the number of boxes within the region of influence are reduced. This effect therefore needs to be taken into consideration when estimating the Bouguer anomalies.

5.3.1 Bouguer anomalies

The Bouguer anomaly estimation uses the density model covering the full area of Figure 4.1 to avoid too large boundary effects within the areas covered by the maps. The lateral extend of the boxes used in the analysis is 1.5×1.5 km. The computation assumes measurement points at sea level ($z = 0$), and all mass above this level is excluded from the gravity computation. This way, the terrain onshore of the Kii Peninsula above the sea level does not affect the original gravity computation. The total gravity was initially computed for all the mass between $z = 0$ and $z = 60$ km. However, since the deepest layers cause large boundary effects, these values make it difficult to analyze the resulting anomaly maps. Therefore, the results are found by computing absolute gravity for all boxes between $z = 0$ and $z = 35$ km. This was a reasonable approach since the gravity values below this depth are fairly uniform and will therefore likely not have an effect on the anomalies.

The Bouguer corrections on the ocean layer are computed both by using the GravMod modelling tool (OCTIO Gravitude 2014) and by using a Bouguer plate. When correcting with the Bouguer plate, the estimated seafloor depth is used to determine the thickness of the Bouguer plate at each measurement point.

For the correction using the GravMod tool (OCTIO Gravitude 2014), the boxes labeled with layer 2 are extracted from the model. They are given a new density of 1630 kg/m^3 based on the difference between the average crustal value usually used for Bouguer correction, $\rho_c = 2670$ kg/m^3, and ocean densities, which lie around 1040 kg/m^3 in the density map. The gravity computation is then conducted for the oceanic boxes with the new densities, for all surface measurement points. The new gravity values are added to the absolute gravity.

After testing different ways of applying Bouguer and terrain corrections to the computed gravity values, it is determined that the corrections that give the most similar results is a terrain correction through exclusion of boxes above sea level, thereby removing the negative effect on the gravity signal at each measurement station from the terrain above sea level. There is little difference between the two methods used for the Bouguer correction, indicating that the errors in using the Bouguer plate approximation are limited. Both methods therefore give a similar representation of the Bouguer anomalies.

5.4 Time-lapse analysis

The time-lapse gravity modelling is done using a reduced section of the study area, shown in Figure 5.6. The reduced density map covers a region of 59 764 km^2, and 60 km depth. The spacing of the measurement points along the seafloor is chosen as 1.5×1.5 km to obtain fairly detailed solutions for the gravity values, while also

allowing for lower computation time of the time-lapse gravity than a finer grid.

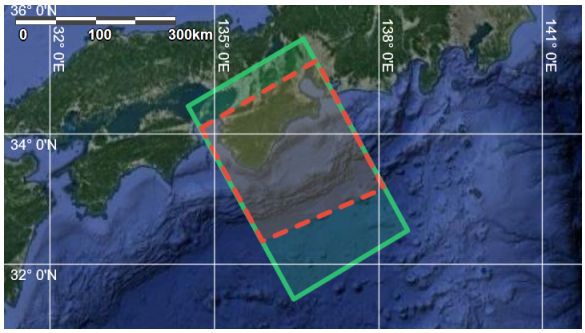

Figure 5.6: Extent of the reduced study area (red) used for the time-lapse analysis, compared to the total study area (green) within the Nankai trough and southwestern Japan. (Source: D-map (2019))

The main assumption of the time-lapse modelling is that slow earthquakes occur due to changes in fluid migration within fault rocks. The feasibility of detecting fluid changes along these areas is then studied, and with that the detectability of slow earthquake events and fluid changes leading up to them through time-lapse gravity measurements. The modelled regions are also chosen based on the assumption that sediments along the plate interface affect the coupling between the overriding and descending plate. The assumption is that the transition between the seismogenic zone and the loosely coupled region is found when this sediment section no longer comes into contact with the descending basalt layer in the model. It is therefore assumed that all regions below this transition zone on the plate interface are locked during the interseismic period, and no alterations in fluid composition occur here.

Slow earthquakes in the shallow region of the Nankai trough have been linked to increased pore pressures within fault rocks, as discussed in Chapter 2.3.2 on slow earthquake mechanisms. The fluid alterations done through the modelling are therefore chosen to reflect changes in pore pressures within the modelled rocks. The permeability of a rock is controlled by the pore space geometry, cracks and fractures within the rock. These factors control how fluid flows through the rock. Through the time-lapse modelling, one case assumes that an increase in pore pressure within a rock implies that impermeable sections in the rock traps the water from flowing through, leading to a build up of water within the rock. The increase in water is assumed to cause expansion of pore space, and therefore a volume increase. Compression of the rock is also assumed to cause an increase in pore pressures, as the pore space is compressed along with the water within. This is then assumed to lead to fluid expulsion from the rock section. The two cases for pore pressure increase, either through expansion or compression, are modeled through the three scenarios introduced in Chapter 3.2.3.

Scenario 1 assumes that slow earthquakes occur along the plate interface, therefore

the aim is to model an increase in water volume along the descending basalt layer. In the next scenario, the locations of increased water volume are determined by the exact location of slow earthquakes in the set of shallow VLFE catalogs introduced in Chapter 4.4. This implies that the earthquakes do not necessarily occur along the plate interface, but could also initiate along smaller faults either within the accretionary prism or the subducting slab. This scenario would then reflect deformation over an area covering several layers, which implies that the changes in physical properties could occur over a larger area, not only along a single fault plane.

Scenario 3 uses the sedimentary layer at the base of the accretionary prism to model compression of the sedimentary rocks. This layer is chosen assuming that these sediments contain water either due to suction at the trough introducing oceanic water into the system, or from mineralogical and hydrological processes taking place within the rocks as they are buried. This scenario accounts for compression of basal sediments solely caused by the locking of the seismogenic zone in the interseismic period. The modelling therefore does not consider changes in pressures on the rock caused by increasing overburden weight on the basal rocks of the Nankai trough sediment section, which would be the case as the thickness of the overlying sediments in the accretionary prism increase.

In contrast to the two previous scenarios, the purpose of the modelling of the sediment section is to reflect loss of fluid within the rocks, through cases where the compression expels fluid from the pore space. Figure 5.7 gives an illustration of the modelled regions in the subduction zone. The depth of 9 km and the horizontal length of 34.9 km from the trough indicates the extent of the area used for scenario 3. The depth of the sediment layer towards the trough is indicated in the Figure as 4.2 km. Scenario 1 follows approximately the same extent, however the basalt layer is included down to 10 km depths along the plate interface as it lies slightly deeper than the sediment layer. The orange stars aim to illustrate the approximate extent of the VLFE catalogs used, and the square indicates the parts of the area used for the modelling. For the second scenario, some of the slow earthquakes outside of the square are used as well, however only to a maximum depth of < 15 km.

The alterations done to the boxes in scenario 1 and 2 are based on volume increase of the boxes involved. When modelling an increase of fluid in the rock, a volume section dV is added on top of all the boxes, assuming that a build up of water will lead to an increase in pore pressure, and thus an increase in pore space and fluid volume. The new volume added is therefore solely caused by water increase in the rock, with a density of $\rho_{water} = 1030$ kg/m^3. Considering the large variability in the size of boxes as discussed in Section 5.2, the volume increase is assumed to be equal for all boxes. This allows for a more direct comparison of the gravity signal obtained from different sections of the modelled region, as the extent of the initial

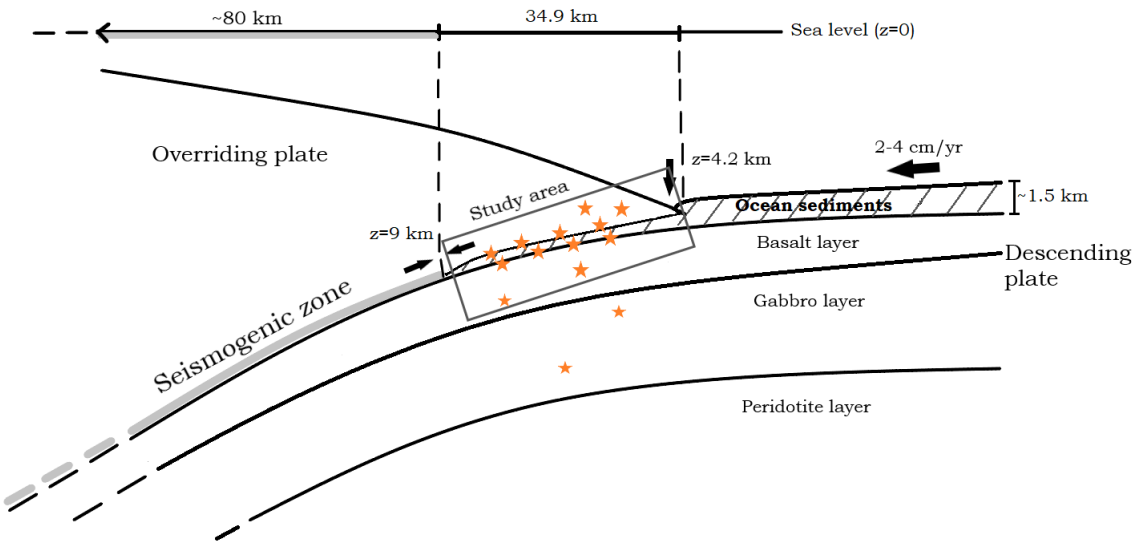

Figure 5.7: Illustration of trench region used for the time-lapse analysis, with parts of the 1.5km thick incoming sediment section subducting along with the Philippine plate. The arrows indicate the direction of the plate movement, and compression in regions of the plate. The orange stars indicate areas where VLFEs have been located within the accretionary prism and the descending plate. The length of the seismogenic zone is taken from the edge of the study area (gray square) and landward, determined by studying Figure 10 of Nakanishi, N. Takahashi, Park, et al. (2002).

box does not affect the added volume. For the third scenario, the case modelling a reduction of volume uses a similar method as the two previous scenarios, with a constant volume removed from each box. The constant volume case, however, uses the original extent of the chosen boxes and a constant porosity decrease for all boxes. Therefore, the added mass varies across the chosen region depending on the size of the initial box.

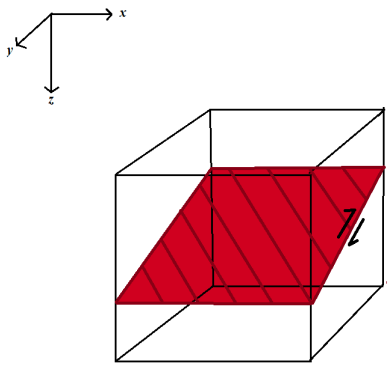

Figure 5.8: Illustration of the fault plane on which VLFEs and fluid alterations occur within the box. Since the majority of the VLFEs included in the analysis exhibit thrust fault mechanisms, the fault mechanisms is indicated as such in the illustration.

When modelling the specified VLFE locations, the boxes are assumed to represent the fault planes on which the events occur, as illustrated in Figure 5.8. This implies that a fault plane is enclosed within each box, and fluid increase within the fault plane leads to a volume increase for the whole box. For boxes where several VLFEs are included due to close spacing of the events, the modelling assumes that all these events occur along the same fault plane.

When choosing the lateral extent of each box to use for the modelling, the choice is first based on how small the boxes need to be obtain a good resolution of the area, without leading to long computation times. The size of the boxes are also compared to estimated rupture lengths of faults where VLFEs occur, to determine if each box can represent a fault section involved in a VLFE event, as Figure 5.8 illustrates. If the box is smaller than the rupture extent of the VLFE it is supposed to represent, the box will not give a good representation of the fault plane involved in the rupture. D. L. Wells and Coppersmith (1994) introduced empirical relations between fault properties and earthquake magnitudes, based on displacement of regular earthquakes. Even though VLFEs generally have smaller rupture areas than regular earthquakes, the relation can be used to estimate approximate fault parameters involved in VLFE events of significant sizes. The equation determined by D. L. Wells and Coppersmith (1994) for the relation between fault rupture width and magnitude was defined as:

$$M = 4.06 + 2.25 \log(W) \tag{5.1}$$

In Eq. 5.1, W defines the width of the ruptured fault, and M the earthquake magnitude, while the constants are defined by regression. An other relation defined by D. L. Wells and Coppersmith 1994 is found for a fault rupture area A and magnitude:

$$M = 4.07 + 0.98 \log(A) \tag{5.2}$$

Regression lines for Eq. 5.1 and 5.2 are given in Figures 5.9a,b.

Assuming that earthquakes with smaller magnitudes than the events studied by D. L. Wells and Coppersmith (1994) will follow this linear pattern, Eq. 5.1 and 5.2 are used to determine fault parameters of some of the events used in the modelling. For each VLFE catalog, the event with maximum magnitude is used to define approximate fault rupture area and width involved in the event, with results for this analysis given in Table 5.3. To more accurately define fault areas for the VLFE modelling, the size of each box cannot be smaller than the fault properties given here, hence the width of the box must at least be large enough to account for the size of the ruptured fault segment.

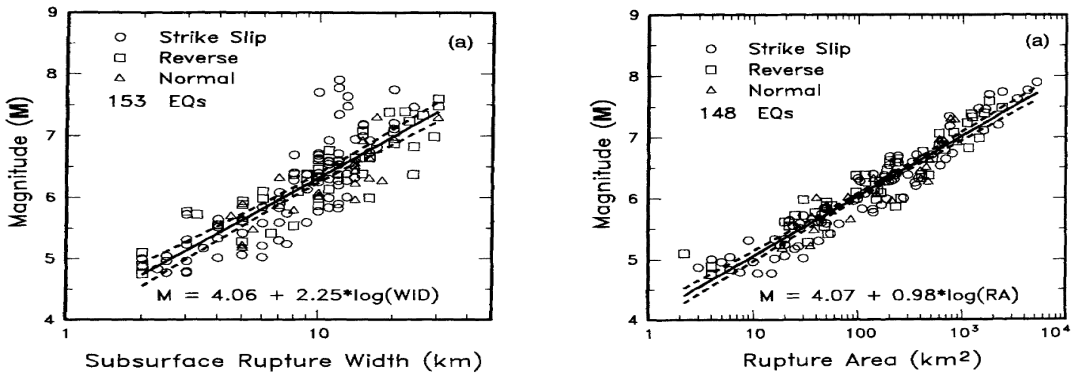

(a) Magnitude and rupture width

(b) Magnitude and rupture area

Figure 5.9: Regression lines for empirical relations between earthquake magnitudes and fault properties. (Source: D. L. Wells and Coppersmith (1994))

Episode	2004 [1]	2009 [1]	2009 [2]	2015 [3]	2016 [3]
Maximum Magnitude (M_w)	4.54	4.54	4.9	3.9	4.1
W (km)	1.63	1.63	2.36	0.84	1.04
A (km^2)	3.02	3.02	7.03	0.67	1.07

Table 5.3: Rupture length and area of the fault corresponding to the maximum earthquake magnitude of the different VLFE catalogs. [1]: Takemura, Matsuzawa, Noda, et al. (2019), [2]: Sugioka et al. (2012), [3]: Masaru Nakano, Hori, et al. (2018),Nakano et al. (2016).

Based on these values, the initial size of 1.5 km in length and width of the boxes is adequate for modelling the VLFEs defined by Masaru Nakano, Hori, et al. (2018) and Nakano et al. (2016), is slightly small for the events defined by Takemura, Matsuzawa, Noda, et al. (2019), and will not reflect the entire fault area used for the VLFEs by Sugioka et al. (2012) due to some large events here. Initially, the same box size was used for all events, however an additional case is modelled for the Sugioka et al. (2012) catalog with a size of 2.4×2.4 km to account for the higher magnitude events here.

The time-lapse analysis for each scenario uses an average seawater density of $\rho_w = 1030$ kg/m^3 (Young and Freedman 2016) for the volume alterations. This value is chosen as it is a common mean value used for water. However, the estimated densities for the ocean layer in the density map lie around 1040 kg/m^3. Therefore, an additional test is conducted to see how much this change in density affects the resulting time-lapse gravity values, to make sure the mean value of 1030 kgm^3 does not underestimate the results. How much the increased density affects the gravity solution varies depending on the areal extent of the modelling region, and the number of events used in scenario 2. Generally, the change in density leads to an increase of around 0.05μGal in the computed time-lapse gravity compared to the computations

with water densities of 1030 kg/m^3, implying that using the mean value by Young and Freedman (2016) has little impact on the resulting time-lapse gravity value. This is however a source of uncertainty in the time-lapse analysis.

The threshold given for gravity detection is determined to an absolute value of 5 μGal, defined by various uncertainties that arise through seafloor gravimetry, as discussed in Chapter 2.4.2. This threshold is therefore assumed to be the lowest gravity value possible to detect with this level of accuracy in the measurements.

5.4.1 Scenario 1: Fluid increase on the plate interface

For the first scenario, alterations are made along the surface of the subducting plate, below the accretionary prism. The model assumes that the surface is defined by the basalt layer of the Philippine plate, assuming that all sediment sections above correspond to the décollement zone and the accretionary prism. The aim is to model fluid increase along the surface of the basalt layer, assuming that fluid is expelled from the sediment section above onto this layer. The VLFEs defined by Masaru Nakano, Hori, et al. (2018) and Nakano et al. (2016) are used to constrain the horizontal extent of the plate interface area used for the modelling, and the boxes are located within the subducting basalt layer (layer 8 in Figure 4.2b of Chapter 4.2). The choice of making the basalt layer the plate interface is based on difficulties in separating velocities of the overlying sediment sections with the low velocities along the surface of this layer.

First, all boxes corresponding to this basalt layer are isolated, and the topmost boxes are chosen for the analysis. Next, the boxes within the horizontal extent given by the slow earthquake locations are analyzed further, and alterations are made to them. The area includes only boxes with a minimum z-coordinate of $\leq$10 km along the interface, based on the fact that underthrust sediments have been located around this depth (G. F. Moore et al. 2015). The defined area is given in Figure 5.10.

The modelling is done by increasing the volume of the boxes, reflecting an indirect increase in porosity and therefore water volume within the rock. The volume increase, dV, and the density of the new volume, ρ_w, are needed to compute the mass change generating the time-lapse signal, and the rest remains constant. The modelling follows the steps given in Chapter 3.2.2. The vertical extent of the original boxes are between 100 and 6000 m, with an average height of 1300 m, and cover a total area of 2711.3 km^2, extending a length of 38.2 km landward from the trough.

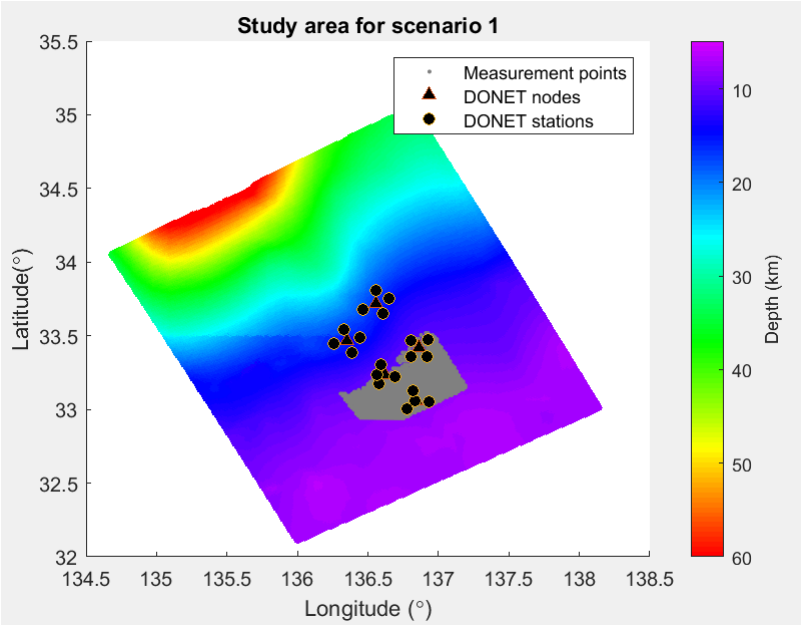

Figure 5.10: Extent of study area along the basalt layer of the descending plate. The locations of the DONET1 observatories are included to give a reference to the location of the study area. The color bar indicates the depth from sea level to the surface of the basalt layer.

5.4.2 Scenario 2: Fluid increase at slow earthquake locations

The boxes chosen in this scenario are constrained by using the exact coordinates of the VLFE events, by finding which boxes those coordinates are located within. In doing so, the number of boxes do not necessarily reflect the number of VLFE events used, as some of them are closely spaced. Several events can be located within one box, and this box then reflects only one "fault area" for all these events. This scenario therefore treats the boxes as fault locations for earthquakes, and alterations reflecting water increase is made for each box. The assumption is that closely spaced VLFEs occurred due to an increase in water volume along one fault plane, implying that the same water volume causes all the events on the individual fault plane. The time-lapse modelling in this scenario follows the same analysis as scenario 1 with an added volume section corresponding to the increased water volume. In contrast to the first scenario, the boxes used in the VLFE analysis can be quite spread out, as illustrated in Figure 5.11.

For the 2015 and 2016 events, a test is conducted to see how much the deeper events, which have a higher uncertainty in the depth locations, affect the total gravity signal at the surface. The events below 15 km are chosen as outliers, based on the normal distribution of Figure 5.12, so the deepest events included in the analysis lie above 15 km. The shallow case includes earthquakes down to 10 km, as these have a known

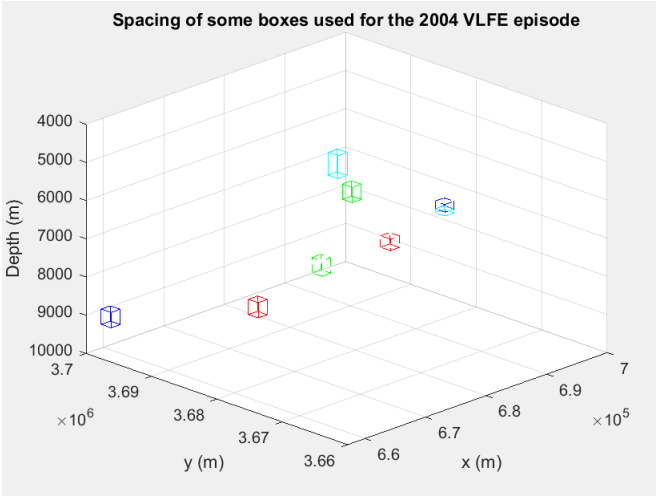

Figure 5.11: Locations of some of the boxes used in the analysis of the 2004 episode by Takemura, Matsuzawa, Noda, et al. 2019. Within each box, a set of earthquakes are located, corresponding to the grid size used by Takemura, Matsuzawa, Noda, et al. 2019 to locate these events.

uncertainty in depth of 2 km. The results for the analysis on the episode with events down to 10 km will be referred to as the "shallow" episode, while the episode including events down to around 15 km will be referred to as the "deep" episode. The following Figures of the extent of the two episodes includes all earthquakes down to $z < 15$ km. A few events have hypocenters below 15 km depths, and one is located at 30 km depth. Some of the deeper events indicate strike-slip mechanisms, and Masaru Nakano, Hori, et al. (2018) discuss that these events might be caused by different processes than the shallower, more constrained VLFEs. Thus, these events have been defined as outliers when considering the modelling of the episodes.

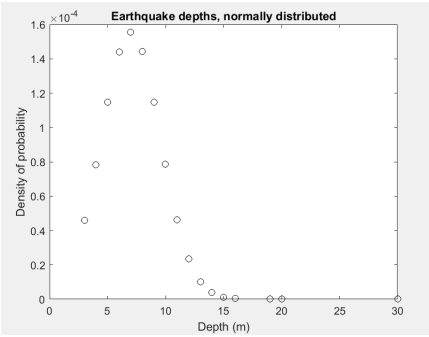

Figure 5.12: Normal distribution of VLFE depths for the 2015 and 2016 events. The distribution indicates the number of events at the given depths. Events deeper than 10 km have a larger uncertainty than ±2 km, and the events below 15 km have few occurrences.

Figure 5.12 is produced by a probability density function for the normal distribution of the depths of events for both the 2015 and 2016 episodes. The normal probability

density function is defined by Eq. 5.3.

$$y = f(x; \mu, \sigma) = \frac{1}{\sigma\sqrt{2\phi}} e^{\frac{-(x-\mu)^2}{2\sigma^2}} \tag{5.3}$$

For the probability density function of the VLFE depths, the mean value is μ=7.032 km and the standard deviation is σ=2.56 km. The plot therefore gives the probability density of the depths of the events.

The 2015 and 2016 VLFE episodes are presented in Figures 5.13 and 5.14, respectively.

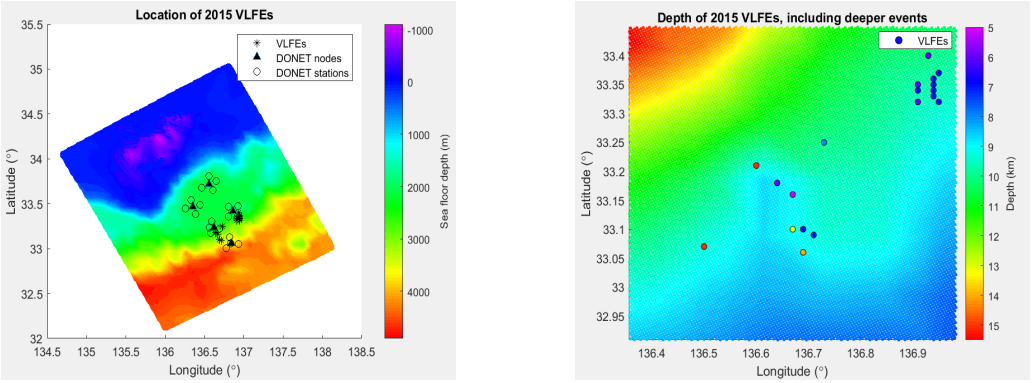

(a) Location of VLFEs and DONET1 network.

(b) Depth of VLFEs relative to the descending slab.

Figure 5.13: Location of the 2015 VLFE episode, given both in depth and in horizontal extent. a) The epicenters of VLFEs are indicated by stars along the seafloor, where depths are given relative to the sea level. The DONET1 observatories are used as a reference for the location of the VLFE events. b) The location of VLFEs are gives as points, where the color of the point corresponds to the depth relative to sea level. The depth of the events are compared to the depth of the descending basalt layer, defined as the plate interface in the model. The VLFEs include the deeper events down to 15 km.

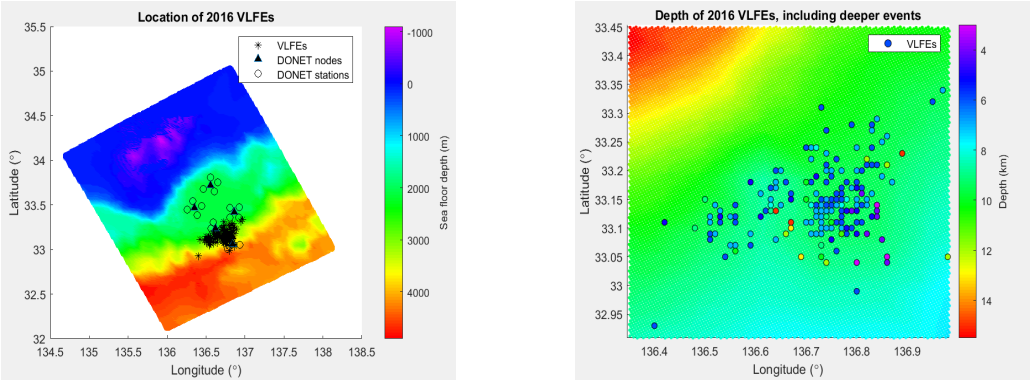

(a) Location relative to seafloor and DONET1 stations.

(b) Depth relative to the descending slab.

Figure 5.14: Location of the 2016 VLFE episode, given both in depth and in horizontal extent. a) The epicenters of VLFEs are indicated by stars along the seafloor, where depths are given relative to the sea level. The DONET1 observatories are used as a reference for the location of the VLFE events. b) The location of VLFEs are gives as points, where the color of the point corresponds to the depth relative to sea level. The depth of the events are compared to the depth of the descending basalt layer, defined as the plate interface in the model. The VLFEs include the deeper events down to 15 km.

The boxes chosen for the VLFE events reflect a variety of different rocks. The 2015 episode include rock sections within the sandstone and limestone layer, including additional boxes from the gabbro layer of the descending plate when deeper events are used. For the shallower events, the boxes have a height range of 400-600 m, reflecting fairly uniform box extents. The events within the gabbro layer correspond to boxes with a maximum height of 3900 m, caused by the small variation between density values within this layer.

The boxes chosen for the 2016 episode are located within a larger range of rock types, including all three sediment sections discussed in Chapter 4.2.1, and some events in the basalt and gabbro layer of the Philippine plate both for the shallower and deeper events. Five of the events included in the 2016 episode are located within the ocean layer of the model, which might be caused by the uncertainties in depths of the events given in the catalog, or by the uncertainties of 5 km in the depths of the 3D velocity model. The events located within the ocean layer are therefore not used in the analysis.

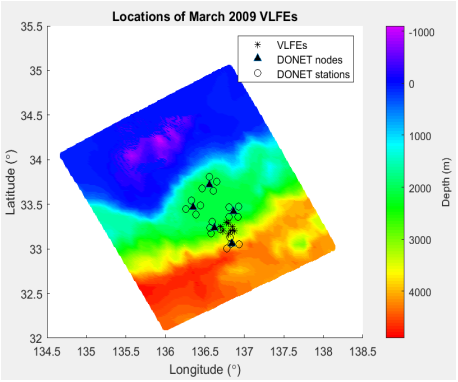

(a) Location relative to the seafloor

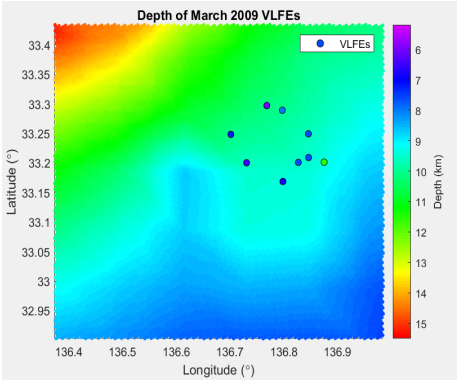

(b) Depth relative to the descending slab.

Figure 5.15: Location of the March 2009 VLFEs defined by Sugioka et al. (2012), given both in depth and in horizontal extent. a) The epicenters of VLFEs are indicated by stars along the seafloor, where depths are given relative to the sea level. The DONET1 observatories are used as a reference for the location of the VLFE events. b) The location of VLFEs are gives as points, where the color of the point corresponds to the depth relative to sea level. The depth of the events are compared to the depth of the descending basalt layer, defined as the plate interface in the model.

The locations of the 12 VLFEs as defined by Sugioka et al. (2012) are shown in Figure 5.15. The boxes chosen include rocks from the sandstone, limestone and descending basalt layer.

For the catalog defined by Takemura, Matsuzawa, Noda, et al. (2019), the spacing of the events are much larger than the two previous catalogs, which is shown in Figure 5.16, relating them to the locations of the DONET1 observatories on the seafloor.

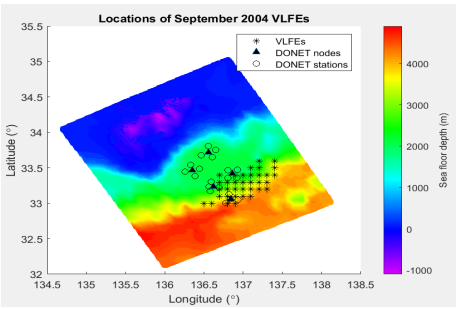

(a) Location of the 2004 VLFE episode.

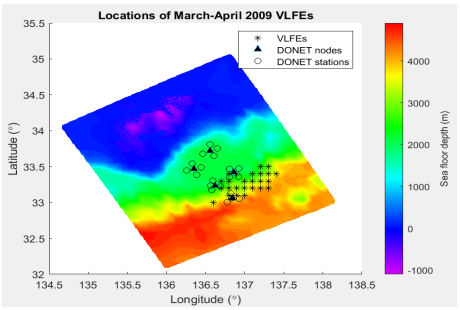

(b) Location of the 2009 VLFE episode.

Figure 5.16: Locations of the 2004 and 2009 events defined by Takemura, Matsuzawa, Noda, et al. (2019), relative to the seafloor and the DONET1 stations. The epicenters of VLFEs are indicated by stars along the seafloor, where depths are given relative to the sea level. The DONET1 observatories are used as a reference for the location of the VLFE events.

Figure 5.17a,b give the depths of the September 2004 and March - April 2009 episodes defined by Takemura, Matsuzawa, Noda, et al. (2019). The plots indicate that the grid chosen for the CMT inversion of the events is slightly shallower near the trough than the interface of the descending basalt layer. This suggests that

the fault model used for locating the VLFE events lies within the sediment layers rather than along the plate interface of the geological model.

Several VLFEs are located to the same coordinates, given by the grid from Figure 4.8 of Chapter 4.4.3. Thus, the VLFE positions shown in Figure 5.17 in reality reflect several VLFE events, but only show the grid locations.

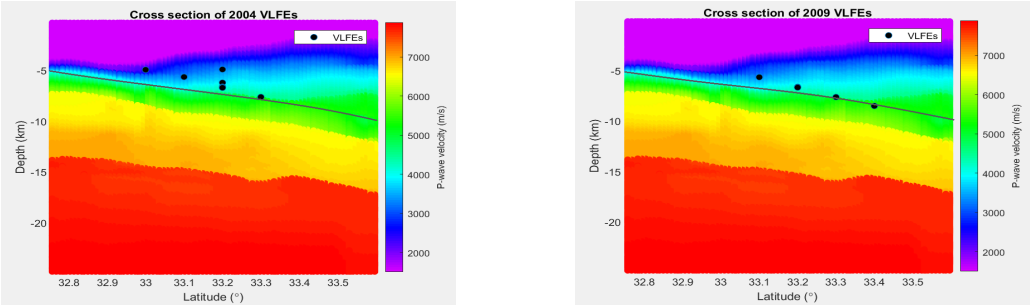

(a) Cross-section of 2004 VLFE events.

(b) Cross-section of 2009 VLFE events.

Figure 5.17: Depth of 2004 and 2009 VLFEs as defined by Takemura, Matsuzawa, Noda, et al. (2019).The cross-sections of the velocity model are found at 136.8°E, and the events are within ±0.001° of this cross-section. The interface of the basalt layer is indicated by a line in the cross-sections. The points reflect the positions of the grids used for locating the events, and several events are located to the same coordinates within this grid.

Based on the coordinates of the events from these two episodes, 43 and 27 boxes are chosen to represent the 2004 and 2009 episodes, respectively. This leads to an average of 7 events in each of the boxes chosen for the 2004 episode, and an average of 5 events in each of the boxes chosen for the 2009 episode. The boxes for both episodes included sections of the mudstone, sandstone and limestone layers, and therefore reflect other locations than the basalt layer of the geological model. Considering the large spacing between the grids used for locating the events, additional boxes are chosen for these two episodes, attempting to see if the additional boxes give clearer results in the time-lapse gravity signal plots. For each box in which slow earthquakes are located, boxes on either side of this box are included in the modelling. The results are shown in Figure B.4a,b of Appendix B.2.

5.4.3 Scenario 3: Compression within accretionary prism sediments

This scenario aims to model compaction within a section of sediments following the dip of the plate interface. As the geological model does not directly include a layer corresponding to the underthrust sediments on the plate interface (Following the discussion in Chapter 4.2.2), the sandstone layer at the base of the accretionary prism is chosen for the modelling. This assumes that velocities that could correspond to the underthrust sediment package are included in the sandstone layer.

The seafloor depth coordinates along the surface of the accretionary prism are chosen to constrain the area used for the analysis in this scenario. Here, coordinates within an area between 1500 m and 4200 m depths below the seafloor are chosen on the surface of the accretionary prism. Figure 5.18 shows the extent of these seafloor coordinates. Boxes below these points corresponding to the sandstone layer are extracted, and the boxes at the bottom of this layer are used for the analysis, following the dip of the subducting plate down to a depth of 9 km. After this depth, the descending basalt slab comes into contact with the limestone layer rather than the sandstone, and is therefore not used for the analysis. The underthrust sediment section off the Kii Peninsula is assumed to have an approximate thickness of 200 m (Tsuji, Minato, et al. 2017). Based on this, only the lower boxes of the sandstone layer along the surface of the descending basalt slab are chosen for the analysis, assuming that most of the compression and fluid expulsion occurs at the bottom of the accretionary prism.

The modelling of this scenario follows two cases, based on assumptions of how a rock behaves under compression:

- The volume is reduced due to pore space reduction and thus compaction of the entire rock, modelled as a constant water volume decrease within each box

- The volume remains constant, but some of the pore space is replaced with solid rock

The first case follows the method for decreasing the volume of the rock as presented in Chapter 3.2.2. This change in volume is assumed to be the result of expelling water from the rock. A constant height of dh is used for all the volume elements dV, to compare the changes across the whole section more accurately. The entire trench area is reduced to only study the signal in the region used for the previous scenarios, shown in Figure 5.18.

For the second case, the gravity computation is done using the original extent of the chosen boxes, but with a new density. This density is given by Eq. 3.18, which implies that the change in density are a result of replacing some of the volume previously comprised of water with solid rock. The change is solely caused by a porosity decrease, which is equal for all the boxes.

The final section covers a length of 34.9 km landward from the trough axis, and a total area of 21 965 km^2, and is therefore the largest area used for time-lapse analysis. The boxes used for the analysis have thicknesses ranging from 100 m to 900 m, with a mean thickness of 237.5 m. The size of the altered boxes are therefore reasonable to represent the subducted sediment section.

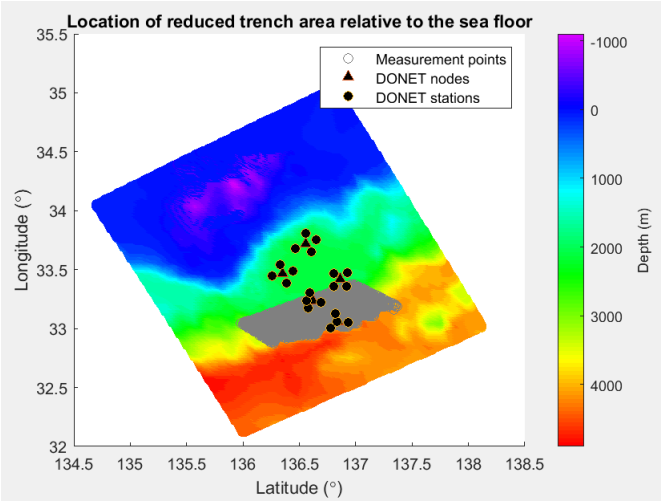

Figure 5.18: Extent of area used for compression analysis. The area is given as measurement points along the seafloor, and boxes below this are included in the analysis. The depth of the seafloor is given relative to sea level.

5.4.4 Uncertainties in time-lapse modelling

One uncertainty considering the time-lapse modelling is that volume alteration assumes that no horizontal changes are made within the boxes. Only the vertical extent of each box is altered. In addition to this, altering the top of the box rather than the bottom is a source of uncertainty. However, this uncertainty is a result of the depth uncertainty in the VLFEs. If the depth could be constrained with a lower uncertainty than around 2 km, or 0.8 km for the 2009 events defined by Sugioka et al. (2012), the exact locations of the added volume element could reflect the exact depth of the VLFE. This is not an issue in scenario 1, as the fault is assumed to be at the top of the boxes, and therefore a volume increase at the top is reasonable.

Since scenario 3 does not account for compression caused by differences in overburden pressure, an uncertainty in the modelling of this scenario is that the assumed porosity loss is the same over the whole region. For the deeper regions, the porosity after compaction may therefore be overestimated, which may lead to an underestimation of time-lapse gravity values.

In addition to the uncertainties posed by the data and the assumptions made through the modelling, the time-lapse gravity modelling does not account for any large scale temporal density variations within the subsurface. These variations can for instance be caused by steady convergence of the Philippine plate, tidal variations or alterations deeper in the model.

Chapter 6

Results

The results presented in this chapter are obtained by first creating a density map from a 3D velocity model. The density map is discretized in separate filled rectangular prisms, and the gravitational influence of each of the boxes chosen for the modelling are computed for each measurement point at the seafloor. For the Bouguer anomaly computation, the entire area is used for the modelling of absolute gravity values, while the time-lapse analysis is conducted over a reduced area, only computing gravity for small regions within this area. Volume or density alterations are applied to each individual box, in order to represent changes in fluid along fault planes or within the pore-space of the rocks.

6.1 Bouguer anomaly maps

The computed Bouguer anomalies are compared to the Bouguer anomaly maps in Figure 6.1.

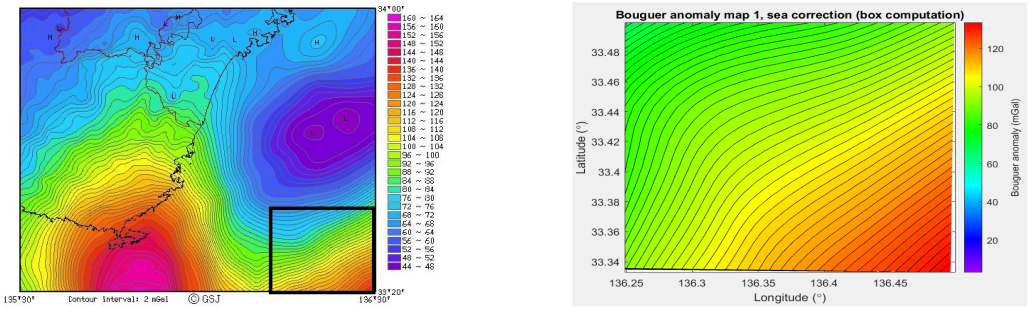

(a) Bouguer anomalies, Map 1

(b) Modelled Bouguer anomalies, Map 1

Figure 6.1: Comparison of the estimated Bouguer anomalies and Map 1 provided by the GALILEO database (Geological Survey of Japan 2019). The square in a) indicates which region is compared to the modelled anomaly results in b).

An offset is added to the computed values to obtain the same range of values as the maps allow for direct comparison of the maps. Due to issues with large boundary effects in the resulting modelled Bouguer anomalies, and some difficulties in resolving the onshore region in the conversion of the 3D velocity model to the density map, only Map 1 provided by the GALILEO database (Geological Survey of Japan 2019) has been considered in the results.

6.2 Time-lapse gravity

To describe the time-lapse results, the size of the area involved in the analysis is given, along with the total water volume added or subtracted from the area, or the new mass added in the case of constant volume. The maximum gravity value of δg is also included, along with the amount of change in mass per square kilometer and the average porosity change ($\overline{\Delta\phi}$) corresponding to the obtained gravity value. $\overline{\Delta\phi}$ is the porosity change from the original porosity, and is given as percentage. This effective porosity as a function of a given volume increase can vary depending on the volume of the initial box chosen for the analysis, but a mean value is given here to represent the whole area. The threshold for absolute time-lapse gravity is defined as 5 μGal, and values have been computed to obtain a maximum of this value. Therefore, the results reflect the minimum amount of fluid volume needed to produce an absolute gravity change of 5 μGal at any of the measurement points. For the scenario modelling fluid volume reduction, a decrease in gravity is observed and the values are modelled for a minimum time-lapse gravity value of -5 μGal.

The new porosity computed is based on the initial porosity of the rock type within the box, and the relation between the original volume of the box and the height of the altered volume section, dV. The volume fraction corresponding to the pore space is then compared to the new volume. The relation between the original porosity and the new porosity, ϕ_{new}, is given by Eq. 6.1:

$$\phi_{new} = \frac{h_0\phi_0 \pm dh}{h_0 \pm dh} \tag{6.1}$$

Where h_0 is the original height of the box, ϕ_0 is the original porosity within the box, and dh is the height of the altered volume element dV on the box. Since the horizontal extent of the boxes remains constant, the only effect on the volume of the box is the change in height. The equation thus relates the pore volume of the original box to the altered fluid volume. For an increase of volume, 6.1 leads to an estimate of the increased porosity of the rock that is needed to sustain the added fluid volume. For a decrease in volume, the height change is negative and the equation states how the porosity must be reduced to expel the relevant amount of

fluid. Hence, the volume reduction of the rock section is only related to a reduction of pore space.

For the plots visualizing the distributions of the mass change with depth, the depth is based on the center of the added or removed volume section dV. Generally, the thickness of these boxes are below 1 m, hence the center is a good representation of the depth of each box. The time-lapse plots include locations of some of the DONET observatories, to indicate the location of the anomalies.

6.2.1 Scenario 1

For each box used for this analysis, a mass increase of $33{\times}10^7$ kg is added to the box. Figure 6.2 shows the distribution of the added mass with depth. All markers are of equal size, representing the equal mass distributed in all the locations, and the colors correspond to the depths relative to sea level of the sections dV added to each box in the interface model. The resulting time-lapse gravity for this scenario is given in Figure 6.3.

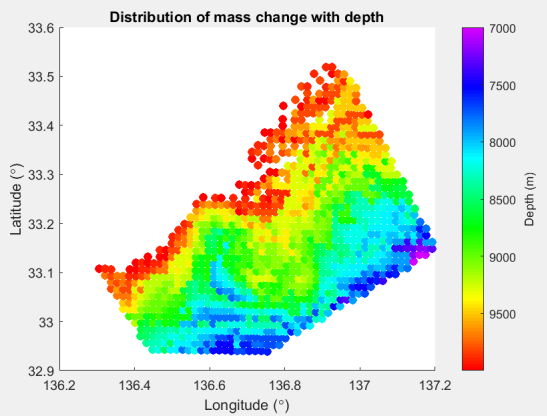

Figure 6.2: Distribution of increased mass with depth.

Table 6.1 gives the results of the variables used to define the changes applied to the boxes. The increase in mass per area indicates that 1.46×10^8 liters of water is needed per square kilometer to obtain a gravity signal of 5 μGal somewhere on the surface of this region. An average porosity increase of approximately 0.026% can sustain this amount of water within the rock sections. Thus, the porosity of the sections of basalt used for the analysis are on average increased from 15% to 15.026%.

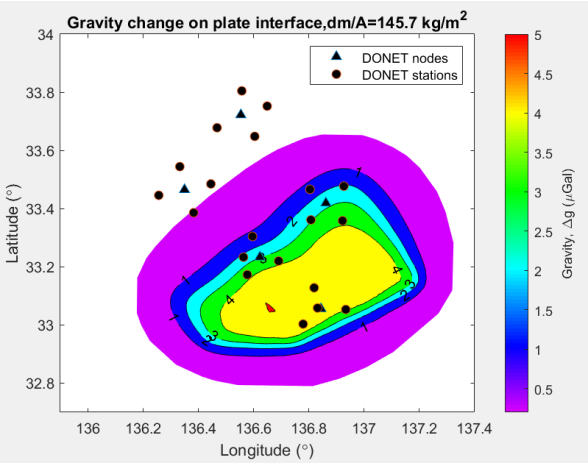

Figure 6.3: δg for plate interface model.

	Area (km^2)	Gravity, δg_{max} (μGal)	Volume increase (km^3)	Mass increase per area (kg/km^2)	$\overline{\Delta\phi}(\%)$
Interface	2711.3	5.01	0.38	1.46×10^8	0.0262

Table 6.1: Results for plate interface time-lapse modelling with a gravity threshold of 5μGal.

6.2.2 Scenario 2

The results for scenario 2 will be presented by first considering the 2004 and 2009 episodes, then the 2015 and 2016 episodes. The latter includes a table for comparison of the deep and shallow events.

The results for the 12 events between March 24.-28., 2009 are given in Table 6.2. The analysis has been done both for horizontal extents of 1.5×1.5 km for the boxes, and for extents of 2.4×2.4 km. The mass added to each box is 2.05×10^9 kg and 2.49×10^9 kg, respectively, and the mass distributions are given in Figure 6.4a,b.

Some of the boxes are not present in the mass distribution plots due to boxes placed at the same latitude and longitude coordinates. Figure 6.5 is added to show how the depths of these boxes relate to the boxes shown in the mass distribution plots in Figure 6.4a,b.

Box size	Area (km^2)	Gravity, δg_{max} (μGal)	Volume increase (km^3)	Mass increase per area (kg/km^2)	$\overline{\Delta\phi}(\%)$
1.5×1.5 km	27	5.02	0.024	3.56×10^8	0.21
2.4×2.4 km	63.4	5.02	0.025	4.06×10^8	0.077

Table 6.2: Results for the March 2009 events located by Sugioka et al. (2012), with grid spacing indicated in the first column.

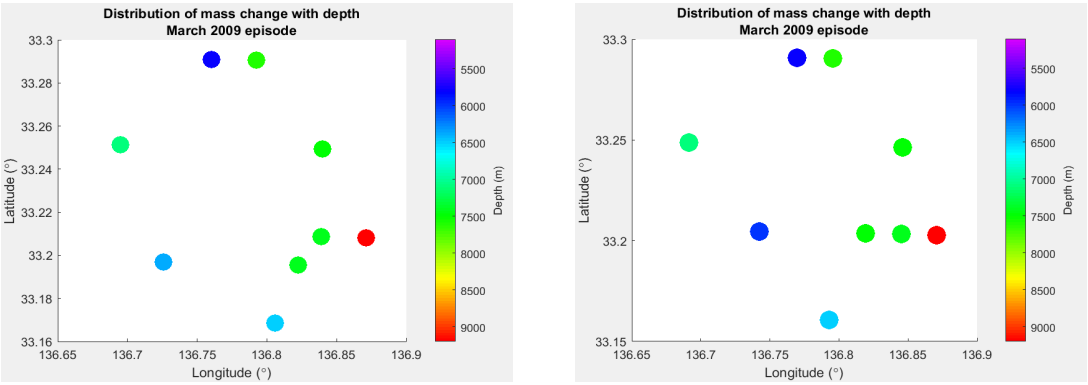

(a) Boxes with 1.5×1.5 km horizontal extent.

(b) Boxes with 2.4×2.4 km horizontal extent.

Figure 6.4: Mass distribution with depth for the two cases of the March 2009 VLFEs.

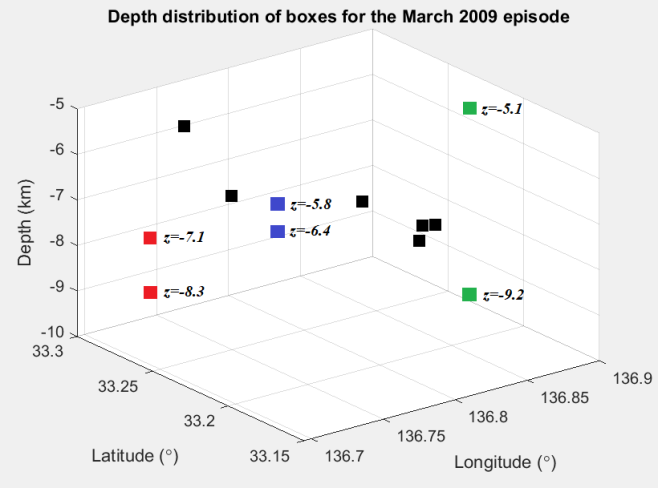

Figure 6.5: Depth of overlapping boxes. The boxes are colored to indicate which boxes are placed at the same coordinates. The red boxes correspond to (136.69,33.25) in longitude and latitude coordinates. Blue boxes are at (136.72, 33.19), and green boxes are at (136.87, 33.21). The depths of the overlapping boxes are indicated in the figure.

The gravity signal for the VLFEs of March 2009 is shown in Figure 6.6. The signal is fairly localized, and more water increase would be needed to obtain a signal of $\geq 5\mu$Gal to able to detect it at a wider range within the area. The results of the test on box size shows fairly similar signals. The results of the larger box size is determined to give a better representation of the larger magnitude events, considering that nearly half the events have a magnitude of $M_w \geq 4.5$. Therefore, this Figure has been included in the results, while a comparison of the two plots can be seen in Figure B.3a,b in Appendix B.

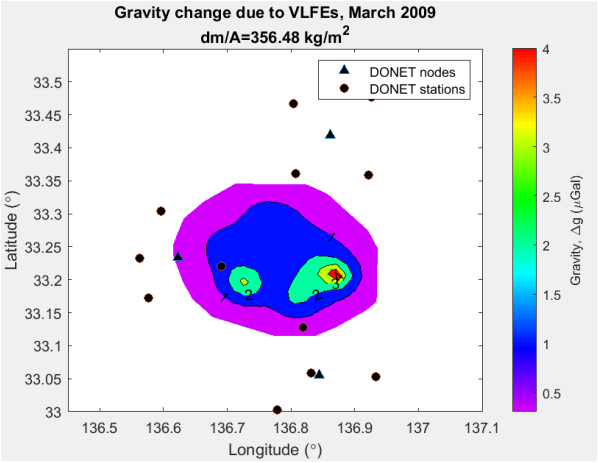

Figure 6.6: δg for March 2009 VLFE episode with larger box size

Table 6.3 gives the results of the analysis on the 2004 and 2009 episodes located by Takemura, Matsuzawa, Noda, et al. (2019). The resulting time-lapse gravity signal for both episodes are given Figure 6.7.

VLFE episode	Area (km^2)	Gravity, δg_{max} (μGal)	Volume increase (km^3)	Mass increase per area (kg/km^2)	$\overline{\Delta\phi}(\%)$
2004	96.7	5.02	0.021	2.26×10^8	0.047
2009	60.7	5.02	0.017	2.86×10^8	0.065

Table 6.3: Results for VLFEs from 2004 and 2009 episodes, located by Takemura, Matsuzawa, Noda, et al. (2019).

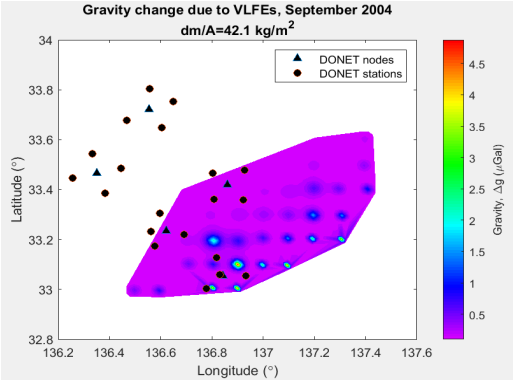

(a) δg for 2004 episode.

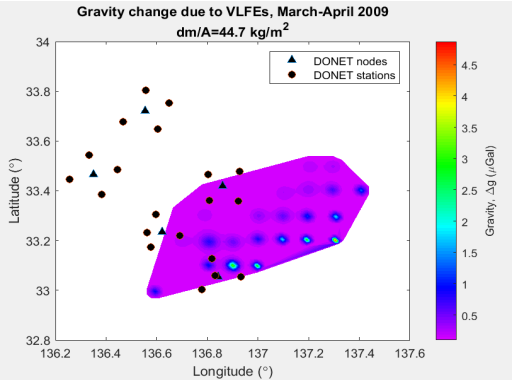

(b) δg for 2009 episode.

Figure 6.7: Time-lapse results for the 2004 and 2009 episodes as defined by Takemura, Matsuzawa, Noda, et al. (2019)

Due to the grid spacing used by Takemura, Matsuzawa, Noda, et al. (2019) to locate these two episodes, the boxes are highly spaced out and several events are located within each box. This therefore gives a concentrated signal in each position, as seen in Figure 6.7a,b.

The results of the 2015 and 2016 events are given in Table 6.4. The shallow and deep episodes have been analyzed to an equal maximum gravity signal of 5.02 μGal to be able to compare the resulting volume change. The time-lapse signals for the events down to 10 km depths are presented in Figure 6.8. The time-lapse gravity signals for the test of deeper and shallower events are given in Appendix B Figure B.1 and B.2 for comparison.

VLFE episodes	Area (km^2)	Gravity $\delta g_{max}(\mu$Gal)	Total volume change (km^3)	Mass change per area (kg/km^2)	$\overline{\Delta\phi}(\%)$
2015 ($z \leq 10$ km)	31.5	5.02	0.033	1.086×10^9	0.16
2015 ($z < 15$ km)	36	5.02	0.038	1.086×10^9	0.14
2016 ($z \leq 10$ km)	375.7	5.02	0.03	8.26×10^7	0.014
2016 ($z < 15$ km)	398.3	5.02	0.032	8.19×10^7	0.013

Table 6.4: Results from the 2015 and 2016 episodes, showing differences between the deep and shallow events.

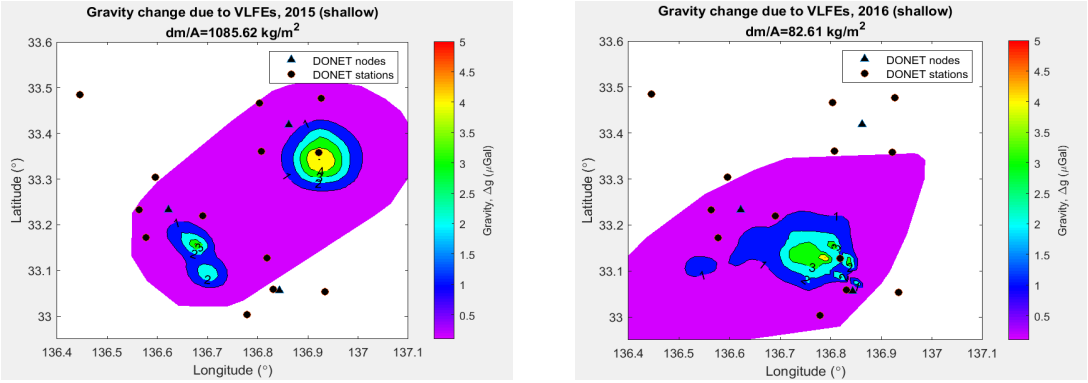

(a) δg for 2015 episode.

(b) δg for 2016 episode.

Figure 6.8: Time-lapse results for the 2015 and 2016 VLFE episodes.

The distribution of mass change with depth for these two episodes are presented in Figure 6.9a,b:

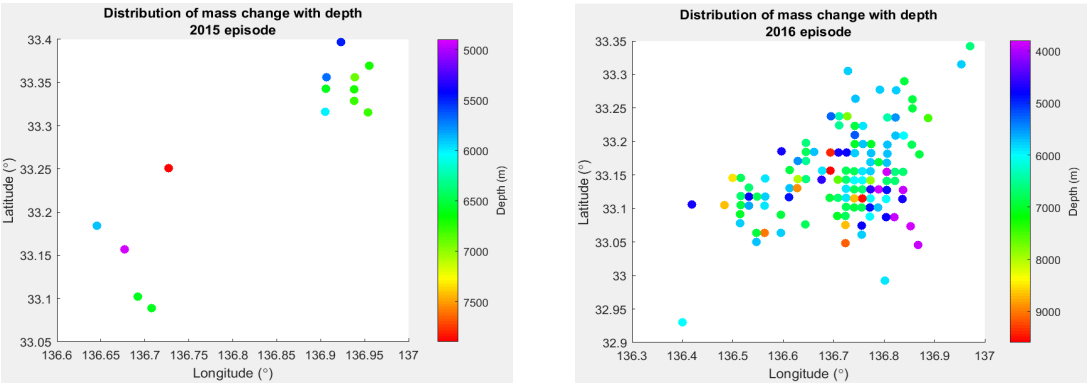

(a) Added mass distribution for 2015 episode.

(b) Added mass distribution for 2016 episode.

Figure 6.9: Depth distribution of mass change for the 2015 and 2016 VLFE episodes.

6.2.3 Scenario 3

The two cases modelling compression along the base of the accretionary prism will be presented separately. Both cases account for porosity loss within the rock, however this affects the rock differently in the two scenarios.

Table 6.5 gives the results of the compression modelled through a volume decrease. Since this case implies that mass is removed from the area, the resulting time-lapse gravity signal is negative. Hence, the maximum value obtained is an absolute value of 5 μGal. To show that the time-lapse gravity is negative, the minimum gravity value has been presented in Table 6.5. The results imply that a decrease in porosity from 25% to 24.9918% in the sandstone section could cause removal of the volume of water that would be possible to detect over the large area given for the analysis.

	Area (km^2)	Gravity δg_{min} (μGal)	Total volume change (km^3)	Mass change per area (kg/km^2)	$\overline{\Delta\phi}$ (%)
Prism base	21965	-5.02	-0.404	-1.89×10^5	-0.0082

Table 6.5: Results for compression modelling of the lower accretionary prism by volume decrease.

A mass of 4.26×10^7 kg has been removed from each box, and the depth distribution of the removed mass is given in Figure 6.10. This mass distribution results in the gravity signal shown in Figure 6.11.

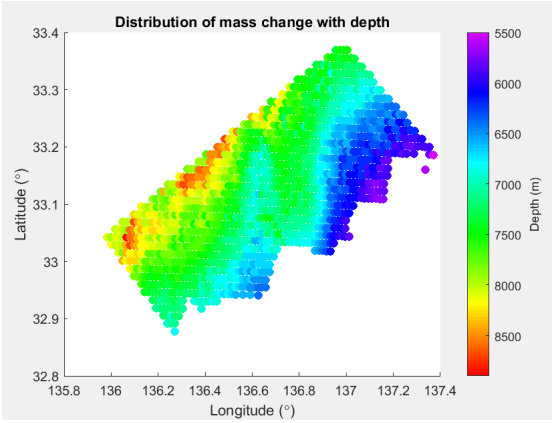

Figure 6.10: Depth distribution of the removed mass in the case of a volume decrease.

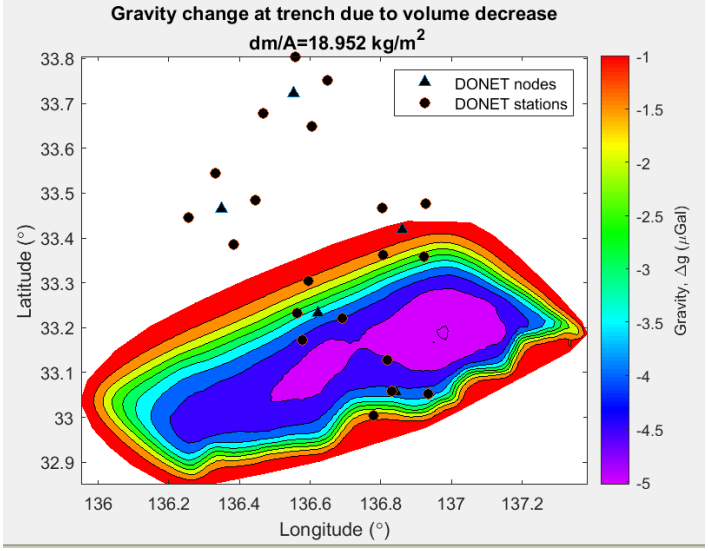

Figure 6.11: δg from volume decrease

The results of the reduced porosity and constant volume is given in Table 6.6. Since the volume is constant, the table gives the total increase of mass across the whole area caused by replacing fluid with solid rock. The porosity given in this case implies a reduction of 0.0049% in each rock section, and not an average over the whole area. This results in the gravity signal shown in Figure 6.12.

	Area (km^2)	Gravity, δg_{max}, (μGal)	Total mass change (kg)	Mass change per area (kg/km^2)	$\Delta\phi$ (%)
Prism base	21965	5.02	3.76×10^{11}	1.71×10^{5}	-0.0049

Table 6.6: Results for compression modelling of the lower accretionary prism by density increase.

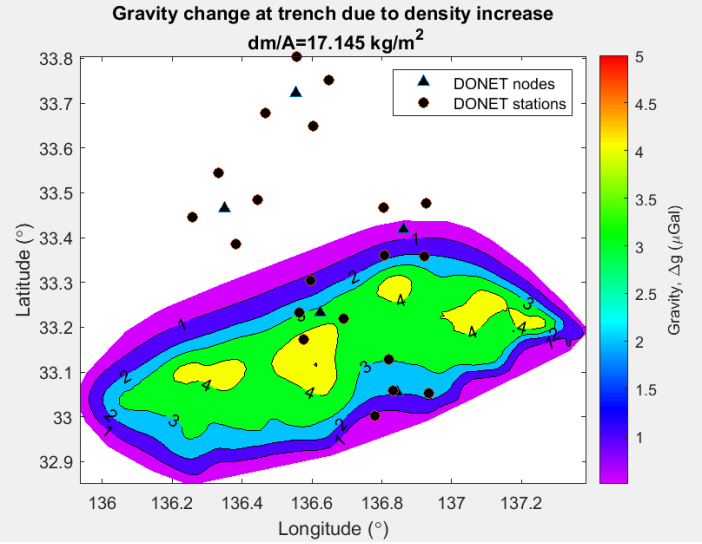

Figure 6.12: δg from density change and constant volume.

Since the boxes used for case of constant volume are the original boxes chosen for the sandstone layer, the center of the boxes give a slightly deeper signal than the removed volume boxes of the first case. In addition to this, the boxes have a variable mass added to them due to the constant porosity decrease applied to boxes of variable heights. The depth distribution of the mass change is presented in Figure 6.13 with various marker sizes, to reflect where the largest mass increase is applied.

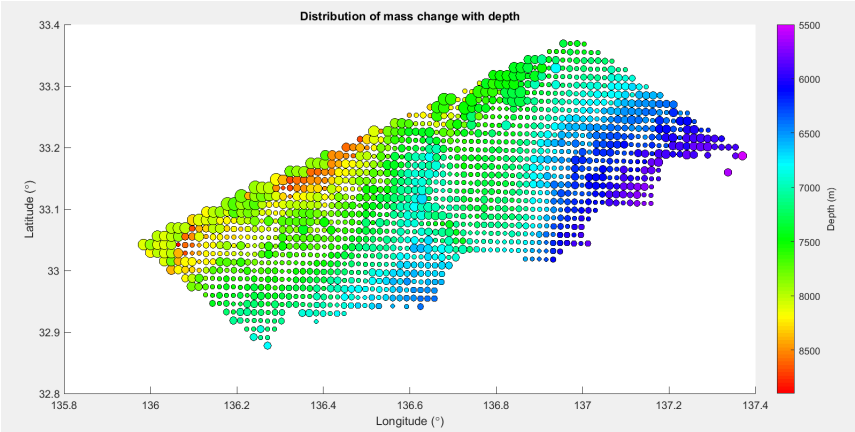

Figure 6.13: Altered mass distribution with depth across the base of the accretionary prism. The size of the marker represents where the larger mass change is applied.

Chapter 7

Discussion

A study on the shallow reaches of the Nankai trough subduction zone has been conducted through this thesis. Temporal variations in the gravity field have been modelled to study the feasibility of conducting a relative gravity survey along the seafloor, above the accretionary prism. Such a survey may improve the knowledge of processes creating earthquakes near the trough, highlighting the importance of evaluating how well seafloor gravimetry can constrain density changes near the trough.

The results shown in Chapter 6 aim to represent variations in fluid flow within fault rocks. The results are obtained by modelling fluid alterations within individual boxes from the 3D distribution of boxes covering the modelled region. The boxes represent fault planes where VLFE episodes occur, and rock sections where pore-space reduction occurs. The Bouguer anomalies are obtained through forward modelling of absolute gravity values. These values are computed to validate the density map used for the gravity modelling. Hence, the Bouguer anomaly maps reflect where a good representation of the modelled region is obtained.

The time-lapse modelling is based on several assumptions. First, the detected VLFEs are assumed to occur as a result of fluid migration along the fault plane where the VLFEs occur, either located at the plate interface or within the accretionary prism. This fluid migration is assumed to trigger the individual VLFE episodes by reducing the frictional strength along the fault surface, thereby reducing the coupling of the fault plane and causing rupture. The fluids are mainly assumed to be from ocean water within the pore-space of a subducting sediment package, which is carried downdip along the surface of the Philippine plate as it subducts. The fluid which triggers these VLFE episodes is assumed to cause density variations within the subsurface, expected to result in detectable gravity changes at the seafloor.

Based on the previous assumptions, the fluid migration within the rocks pore-space or along the fault surface is thought to cause temporal changes in the gravity field

that may be observed using proper gravity measurement techniques. The time-lapse gravity measurement is assumed to reveal temporal changes in the fluid migration within the fault sections defined by VLFE episodes. Hence, the water volume is assumed to be stored within the pore-space of rocks accommodating VLFE episode.

Considering these assumptions, the time-lapse modelling indicates the change in volume of water within a rock volume that is needed to reach a minimum level of detectable gravity change at the seafloor. These results form the following hypothesis:

If a seafloor time-lapse gravity measurement reveals detectable signals to an absolute value of around 5 μGal, it is possible to estimate the minimum fluid volume needed to cause this signal, and the extent of the corresponding slip area related to this detected fluid migration pattern.

The hypothesis can then be tested through a time-lapse gravity measurement experiment at the Nankai trough off the Kii Peninsula.

7.1 Bouguer anomaly map comparison

After studying the details of the estimated Bouguer anomalies, it is seen that the low anomalies in the provided Bouguer anomaly maps are not well resolved in the model. Considering the comparison of the velocity cross section with the density map in Figure 5.2 of Chapter 5.1, a section of the velocity model within the sedimentary layers is not completely resolved in the density mapping. A structural high is found in the assumed sandstone layer of the velocity model, where the density mapping shows a smooth layer. Therefore, the density map cannot replicate exact Bouguer anomaly Maps at this location. The low anomaly regions seen in both Map 1 and Map 2 (Figures 4.5a,b) are likely related to this structure seen in the velocity model. Since this structure is not as obvious in the density map, the low anomalies or not as apparent.

The high anomaly in Map 1 is not seen in the computed Bouguer anomalies, which might be related to the absence of an igneous dome included in the density map. A structure that could relate to this anomaly was not seen in the velocity model at this location either, indicating that the structure is difficult to resolve through seismic surveys. It is also more difficult to distinguish between the separate layers seen in the velocities of the 3D model, as the velocities are generally higher and the layers are less obvious in the velocity profiles.

The boundary effects in the modelled absolute gravity make it difficult to observe anomalies across the whole area covered by the Bouguer anomaly maps from the GALILEO database. Even with removing the higher density layers below 35 km depths, the boundary effect is still prominent in the maps. The area that reflects

the Bouguer anomaly maps best is reduced based on both the absence of the structural high in the density model within the sandstone section, and the dominating boundary effects in the modelled absolute gravity.

Given that some variations within the sedimentary layers are not well constrained by the density map, the gravity values closer to the Kii Peninsula may result in underestimations of the modelled gravity. For the time-lapse modelling scenarios, the area does not cross this structural high within the lower sedimentary layers. Hence, this structure missing from the density map should have little impact on the boxes and their corresponding rock types that are chosen for the time-lapse modelling. The approximate location of the area used in the time-lapse analysis within the cross-section of the velocity model is given in Figure 7.1.

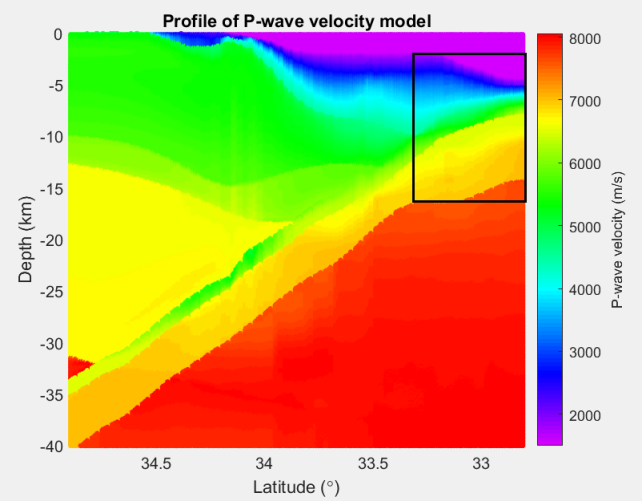

Figure 7.1: Cross-section of the velocity model at 136.5° longitude. The approximate extent region used for the time-lapse gravity modelling relative to this cross-section is indicated by the black square.

The maps used for the comparison are chosen because they covered most of the offshore region of the Kii Peninsula. Since no maps covering the trough were found, it is difficult to determine if the area closer to the trough is replicated better. However, considering that the section of the map that was replicated best is located closer to the trough region, it may be assumed that the density map resolves the structures within the 3D velocity model better in this region. A gravity survey near the trough may then lead to increased information on the gravity variations closer to the trough, thus improving the coverage of gravity anomalies here.

7.2 Time-lapse results

Through forward modelling of gravity, it is possible to obtain unique values for time-lapse gravity fields based on a mass with a known depth, size and location

(Jacoby and Smilde 2009). Thus, it is an important tool in determining exact density changes needed to observe certain variations in the resulting gravity field. Through this project, this is evaluated by fluid volume alterations in the subsurface. The time-lapse gravity scenarios are chosen to model fluid variations within the shallow regions of the Nankai trough. The results therefore reflect the amount of fluid volume that is possible to detect to an absolute value of 5 μGal at the measurement points along the modelled seafloor. The assumed fluid variations occur either along the plate interface or within sedimentary layers of the accretionary prism. The results are used to propose hypotheses on how much fluid volume would be needed within each area to be able to detect any variations in the temporal gravity field.

For some areas used in the time-lapse modelling, in particular when modelling VLFE locations, the maximum time-lapse gravity value in the figures is below 5μGal in the gravity plots. This implies that this maximum gravity value is observed in a highly localized region, with horizontal extents too small to observe in the plots. However, the time-lapse gravity changes linearly as a function of mass change, implying for instance that a doubling of the increased volume results in a doubling of the measured gravity value at the surface. Thus, a measured time-lapse gravity value can be used to estimate the mass change within the subsurface based on these initial values.

The VLFEs from the two episodes obtained from the catalog defined by Takemura, Matsuzawa, Noda, et al. (2019) are located in largely spaced clusters compared to the VLFEs from the other two catalogs. Therefore, a clear difference is seen between the plots of figures 6.7a,b and the results of the other analyses. The location of individual VLFE clusters have a larger extent than the boxes of the model, leading to a spacing of nearly 10 km between each box used in the analysis. The resulting time-lapse gravity signals reflect this large spacing, and leads to concentrations of high-gravity areas where these boxes are located. Even when choosing several boxes around the VLFE coordinates, the gravity signal appears highly spaced out in the plot, as seen in Figure B.4a,b of Appendix B.2. This leads to uncertainties in interpreting the results from these VLFE locations.

As the modelled fluid volume is less spread out, the results of the 2004 and 2009 VLFE episodes obtained through the Takemura, Matsuzawa, Noda, et al. (2019) catalog may not reflect actual fluid increase within the fault plane on which these VLFEs are assumed to occur. The computations on these regions reflect how much fluid increase along discrete faults of 1.5×1.5 km size with 10 km spacing between them would need to produce the gravity signal. The large spacing will lead to small effects on each individual surface measurement point, and more volume would be needed in each box to obtain a 5 μGal gravity change. These results will therefore be excluded from further interpretation to avoid bringing these uncertainties into the final results. Hence, the hypotheses will be based on the results from scenario

1 and 3, and from the VLFE episodes of 2009, 2015 and 2016 from the catalogs defined by Sugioka et al. (2012), Masaru Nakano, Hori, et al. (2018) and Nakano et al. (2016) studied in scenario 2.

For the 2009 episode from the catalog by Sugioka et al. 2012, the boxes with an area of 2.4×2.4 km^2 are determined to give a better representation of the VLFEs. This is due to the large magnitude of the events, which were assumed to cause a wider rupture area along the fault than 1.5 km based on the empirical relations by D. L. Wells and Coppersmith (1994). The results from the larger boxes shows that less porosity increase is needed to sustain the increased fluid volume related to these VLFEs than the smaller boxes, or smaller fault extents.

The case of fluid alterations along the descending plate and within the base of the accretionary prism are both related to VLFE initiation at or near the plate interface. These scenarios therefore indicate the volume of water that would be needed to detect fluid alterations either during or prior to VLFEs along the interface. For the March 2009 and the 2015 and 2016 episodes, the events are located more within the accretionary prism. Although they are located near or around the plate interface, the depth uncertainties of the events make it difficult to determine if the VLFEs occur at the plate interface, or within faults in the accretionary prism. Therefore, these events more closely model a situation where VLFEs do not necessarily occur along the boundary of the interface, but on faults of various extent within the accretionary prism.

From the various regions used in the analysis, the obtained results are based on the size of the area, how spread out each event is and how deep the areas are located. Thus, following the hypothesis introduced in the beginning of this chapter, the following formulations summarize the results of the time-lapse gravity analysis:

- For faults located around 5-11 km depths near the prism toe, a 5 μGal signal would be observed from a total water volume increase of 4.06×10^8 liters per square kilometer.
- For larger VLFE clusters, such as the 2016 episode, a water volume increase of 8.26×10^7 liters is needed per square kilometer to obtain an observable gravity signal.
- Considering the 2015 VLFE episode, where fewer events are located within two clusters, a volume of around 1.09×10^9 liters of water is required per square kilometer to observe the gravity signal.
- For alterations along the plate interface, an area of 4099.5 km^2 would need an average water volume increase of approximately 1.46×10^8 liters of water per square kilometer to reach the threshold for detectable gravity at the surface.
- Assuming compression causes a decrease of water volume in the rock section,

a loss of 1.89×10^5 liters of water per square kilometer is required along an area of nearly 22000 km^2 to be able to detect a change of 5 μGal.

- Assuming compression causes a density increase as pore water is replaced by solid rock, the same large area requires a loss of 1.71×10^5 liters of water per square kilometer to be able to detect a change of 5 μGal at the surface.

The results found here can be used as a base for comparing measured gravity, considering the linear relation between measured gravity and volume change. The exact volume and mass changes observed through this study can be related to studies on fluid flow through porous media. However, this is beyond the scope of this thesis, and the scale of these fluid volume changes have not been related to real values of fluid volumes within rocks.

The results are obviously affected by uncertainties based on the data used for the analysis, and the assumptions made during the modelling. For instance, since gravity measurements are sensitive to the depth of the mass, the volume needed to obtain a signal of 5μGal is changed when the source is shifted closer to or further away from the measurement points. This leads to uncertainties in the modelled time-lapse gravity caused by the depth uncertainties of VLFE events used for the modelling.

The uncertainties in depth of both the VLFE locations and the velocity model could have an affect on the time-lapse gravity. The largest sensitivity of the model is thus the depth of the modelled region compared to the measurement stations. These uncertainties must therefore be considered in the resulting time-lapse gravity signal and the fluid volume needed to obtain this signal. The test of the 2015 and 2016 events are conducted to study depth uncertainties. The tests show that for the 2015 episode, no considerable change in mass is needed per square kilometer when including the deeper events. Only two additional VLFE events are added within the gabbro layer for this episode.

The same test for the 2016 episode shows that inclusion of the deeper VLFE events result in a mass reduction of 70 000 kg needed per km^2 to obtain the same gravity signal of 5.02 μGal. The fault area is slightly increased with the addition of these events since the deeper events correspond to 10 additional faults in the basalt and gabbro layer of the Philippine plate. The difference in average porosity increase is however minimal, while the total mass change on each fault section is 1.66×10^6 kg. The results of these test suggest that for VLFEs occurring within the gabbro layer, little effect is seen on the surface time-lapse gravity. However, by including more events within the basalt layer, less fluid is needed per square kilometer to observe differences in the gravity field. The results of this test suggest that events deeper than the basalt layer of the Philippine plate may not influence the temporal gravity field as much, while events within the basalt layer may have an impact on the measured gravity values. This could introduce uncertainties in determining the

depth of regions where fluid variations occur, given that a time-lapse gravity signal is observed during a survey.

Another source of uncertainties is the porosity value chosen for the rock. If the original porosity value is too high or low compared to real values, the estimated porosity change supporting the change in fluid volume may not reflect real values. The mass change used to compute the time-lapse gravity values is however not directly based on the porosity of the rock section, and therefore reflects changes in fluid volume independent of original porosity. The porosity variations are included to indicate how reasonable the values obtained for the fluid volume are, considering if the rock sections can support this fluid volume change. The estimated porosity changes reflect quite small variations from the original porosity, indicating that the modelled fluid volume variations may be reasonable for the chosen rock sections.

7.3 Implications for subduction zone research

The time-lapse modelling results presented in chapter 6.2 aim to represent pore pressure alterations within the shallow regions of the Nankai trough. Through time-lapse gravity measurements, fluid alterations within fault rocks can be observed. The implications of this is that the depths and horizontal extents of pore pressure alterations can be constrained further. With this, a better understanding of the coupling of the plate within the shallow regions of the Nankai trough would be obtained. Considering the importance of locating asperities in the shallow regions of the subduction zone, information obtained through a gravity survey could be crucial in locating these strongly coupled regions. This is especially important considering the difficulties of obtaining accurate information on the coupling near the trough. If temporal changes in the gravity field are observed, the relations found in the previous section can be used to determine approximate changes in fluid volume along the region, and areas where these changes occur.

Considering the fact that shallower pore pressure variations would be simpler to detect through gravity measurements than deeper alterations, a gravity survey could be beneficial in determining the extent of asperities near the trough. The results from a gravity survey in this region could therefore be complimentary to areas of observed pore pressure variations and low-velocity zones (Araki et al. 2017; Tonegawa et al. 2017). Following the asperity model discussed in chapter 2.3.2, rupture on a larger asperity could trigger subsequent asperities, thus allowing for rupture migration near the trough if larger asperities are located here.

The slip-deficit distribution off the Kii Peninsula region is shown in figure 7.2. Although the slip-deficit rates estimated by Yokota et al. 2016 do not cover the entire region used for the modelling, they can be used to compare the regions of low slip-deficits with regions of VLFE activity in the Nankai trough. The DONET1

observatories shown with the slip-deficit rates in figure 7.2 can be used to spatially compare with the results of the time-lapse analysis.

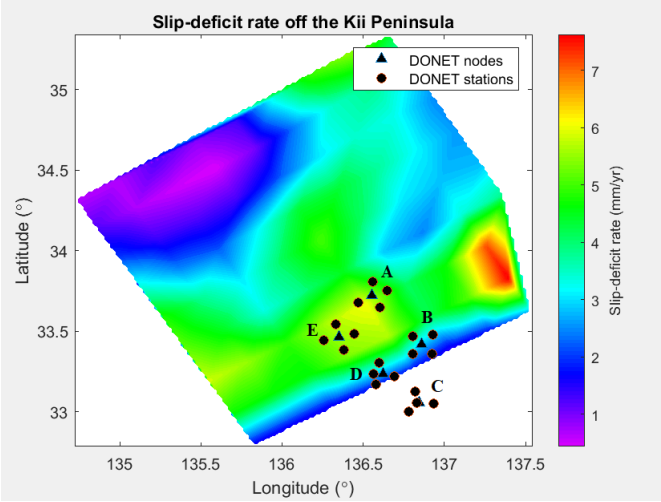

Figure 7.2: Locations of slip deficit rates estimated by Yokota et al. 2016 near the trough off the Kii Peninsula. The DONET1 observatories are indicated by black circles. The DONET1 nodes are labeled from A-E.

The regions below the A and E DONET1 observatories closest to the Kii Peninsula lie above an asperity on the plate interface, indicated by figure 7.2. The modelled regions lie along the edge of this region of high slip-deficit rates, and extend from the trough axis to below the three DONET1 observatories in the trough region, B-D. Thus, the results indicate how strong the gravity signal near these stations would be for various areas within the accretionary prism. The strongest time-lapse gravity signal is located between observatories B-D for almost all the modelled regions, indicating that the gravity measurement would be valuable in locating variations in the shallow regions closer to the trough. Even for the regions of scenario 1 and 3 that both extend below the B and D nodes, the gravity results show weaker signals at these locations. This is caused by the dip of the interface due to regions extending deeper here. Since deeper density variations have less effect on the measured gravity values, it would be more likely to detect variations in the shallower regions near the prism toe.

Based on the results found through the time-lapse modelling, a detected change in gravity at the subduction zone could give valuable information on the processes at work within the accretionary prism. For instance, if temporal changes in the gravity field are observed and can be linked to VLFEs detected by the OBSs within the DONET network, it is possible to test if these changes are related to the VLFE events. However, if temporal changes are detected unrelated to VLFE episodes, the changes could reflect continuous creep. This could then be important in determining the coupling characteristics along the shallow reaches of the Nankai trough, which

may in turn indirectly affect the expected slip during a megathrust earthquake further downdip along the plate interface.

7.4 Further work

7.4.1 Background model

A possible modification to the density map could be to add a variable bulk and shear modulus within each layer, and a decreasing porosity. This would lead to a non-linear velocity-density relation, and could give a better representation of the densities within each layer. Further constraining the décollement zone within the model could give more accurate locations of the modelling scenarios. Hence, a layer corresponding to the thickness and velocities within the décollement, which typically has lower seismic velocities than the overlying accretionary prism, could give a better representation of the deformation area at the base of the accretionary prism.

Refining the rocks within the model could lead to a better constraint on the density distribution of the layers, and the resulting boxes discretizing the density map may represent a more detailed structure. Through this, a more detailed analysis of time-lapse gravity can be studied. In addition to this, the velocity range of each layer can be refined further to replicate the layer interfaces better, including the variable structures seen in the sedimentary layers, discussed in Section 7.1.

By including studies on fluid flow within porous rocks, the volume alterations made to the modelled regions can be better defined. This would lead to more knowledge on how much fluid volume change is expected along this region, and indicate if the resulting gravity value caused by these density changes could be higher of lower than the threshold used for this study. This could be valuable if a gravity survey at the Nankai trough measures changes related to slow earthquake activity. By obtaining more knowledge on the volume variation, a gravity survey could possibly be used to estimate how much fluid change could cause rupture on the involved fault planes.

The absolute gravity can be modelled further by extending the study area using larger parts of the 3D velocity model. If the area is extended, the 3D distribution of boxes will cover a larger area. If the absolute gravity modelling is conducted using measurement points within the same region as studied for the Bouguer anomaly estimation, the layers outside of the measurement points will also contribute to the surface gravity. Hence, the solid angle effect will not cause such large underestimations at the edge of measurement grid. By modelling the absolute gravity values, the trench-parallel Bouguer anomaly, discussed in section 2.4.3, could be computed and contribute to more detailed anomaly mapping near the trough. Through this, possible locations of asperities can be observed, adding to the information on asperities located along the shallower regions of the plate interface.

7.4.2 Time-lapse gravity surveying

Through seafloor gravity surveys, density variations caused by fluid migration in the shallow regions of the Nankai trough can be studied. Using the proposed hypotheses, an estimation of the volume of fluid change can be made based on the measured time-lapse gravity field. The hypotheses can be tested through a gravity survey experiment at the Nankai trough, given that time-lapse gravity value is detected.

For a gravity survey over the Nankai trough, CP locations along the seafloor need to be determined. Of particular importance are the base stations, where the time-lapse gravity needs to be stable. Considering the distribution of areas with high slip-deficit rates given in Figure 7.2, the A and E nodes are possible locations for base stations to use for drift correction. However, even though the plate interface below these observatories may be locked, alterations could occur within the rocks above. The modelling does not account for shallower density variations within the Kumano basin or rock sections below these two observatories. Therefore, it might be safer to assume base stations on the descending Philippine plate, seaward of the trough. For placements of base stations on the descending plate, the convergence rate of between 2-4 cm/yr of the Philippine plate must be accounted for. To test the hypotheses listed in Section 7.2, proposed layouts for a survey are outlined as follows:

Scenario 1: plate interface analysis

The results from the analysis show that a fluid volume of 1.46×10^8 liters of water is needed per square kilometer to observe a gravity signal at the seafloor, with lateral extents of the resulting gravity signal shown in Figure 6.3. A fairly wide distribution of CPs is needed to cover the area that might be involved in the deformation. As deformation along the interface might extend quite deep (around 10 km depths), the CPs should cover these deeper regions as well to obtain good coverage for the test. Therefore, following the DONET1 nodes shown in Figure 2.8 and Figure 7.2, the best coverage would be obtained for CPs extending from node C at the trough to node D, and additionally to node B to obtain a wider coverage over the interface parallel to the trough axis. The distance between the C and D nodes is a little over 25 km, and this distance is approximately the same between the D and B nodes, giving an indication of the size of this area. While the entire modelled interface extends 38.5 km landward, the strongest signal is seen within the locations of these three nodes. This indicates that deformation in the deepest regions of the plate interface will give lower gravity signals. For this scenario, the best coverage would be obtained for CPs between these three nodes, especially near the C node at the trough axis.

Scenario 2: analysis of VLFE episodes

If the aim is to measure over regions where VLFEs have been located, with the

possibility of detecting fluid changes directly related to VLFEs, the areas are much smaller than the previous scenario. Considering only the gravity signal plots obtained by studying the 2009, 2015 and 2016 episodes, survey set-ups can be based on Figures 6.6 and 6.8a,b.

The 2009 episode covers the smallest area, and therefore needs a smaller coverage for CP positions. For these events, it was determined that a fluid volume of 4.06×10^8 liters per square kilometer is needed to obtain measurable values. The entire fluid volume is spread out over an area of 63.4 km^2, while Figure 6.6 indicates that the strongest gravity signal is located within a smaller region than this. Based on the time-lapse signal of this episode, CPs should be located between the three DONET1 nodes discussed in the previous scenario. In this case, the observatories given in Figure 2.8 can be compared to the observatories within the plot. Placing CPs near the C-12 observatory and near the trough would be the best chance to detect fluid migration within this location.

For the 2015 episode, the strongest signal is observed just below the B-6 observatory and near the D-13 observatory, indicating that the best locations for CPs in this case would be near and around these locations.

The lateral extent of the gravity signal from the 2016 episode is fairly similar to the 2009 episode, but located closer to the C node of the DONET1 network. Specifically, the highest gravity values are obtained near the C-12 observatory, indicating that CPs placed around this location will be able to detect fluid changes related to the faults involved in this episode off the Kii Peninsula.

Scenario 3: compression of décollement sediments

This scenario has a similar extent as scenario 1, implying that the CPs need to extend over a similar area to observe signals here as well. However, it appears that the strongest signal is observed for an area extending from the C to D nodes, parallel to the trough. Generally low time-lapse changes are observed at the B node for this scenario. Therefore, variations caused by compressing sediments could likely be detected between the C and D nodes.

Following the discussion of the modelling scenarios above, the results indicate that the optimal region for placing CPs is between the B-6, C-12 and D-13 observatories. CPs placed within this region cover various deformation scenarios, and will therefore have a better chance of detecting temporal gravity changes. Base stations can then be placed on the Philippine plate near the C node, close to the C-10 and C-11 observatories located at the trough axis. Locations for base stations on the accretionary prism are slightly more difficult to determine, considering that the modelling does not cover this area. Further studies of these regions, and shallow earthquakes, could determine more suitable locations for base stations to cover a larger gravity range.

The location of the DONET2 network, shown in Figure 4.13, coincides well with the slow earthquakes outside of the modelled region given in Figure 4.7 of Chapter 4.4. Even though modelling has not yet been conducted over this region, it is a possible area to extend measurements if survey results over the DONET1 regions are positive. Further work could then be to extend the forward modelling analysis of the time-lapse gravity to this region, in order to obtain wider coverage for gravity measurements of the Nankai trough.

Chapter 8

Conclusion

The aim of this thesis is to determine the feasibility of achieving observable time-lapse gravity variations through a survey at the Nankai trough subduction zone, and to evaluate the extent of such a gravity signal. This has been achieved by forward modelling of time-lapse gravity on various regions where density changes caused by fluid migration are likely to occur. By forward modelling of gravity, it is possible to obtain unique values for how much change in fluid volume is needed to detect changes in the temporal gravity field. The analysis indicates various scenarios within the Nankai trough accretionary prism that may lead to changes in water volume along fault planes and within the pore space of rocks.

Several steps are taken to conduct the modelling, including defining a geological model based on the 3D P-wave velocity distribution and known geological features within the region off the Kii Peninsula. Once the density map is created by using the velocity model and the geological model, the density distribution is used to create a 3D distribution of discrete rectangular prisms. Changes are made to sections of these prisms, as a result of various fluid alterations assumed to occur in the modelled regions. The changes to the model are then used directly to model the resulting time-lapse gravity signal. The Bouguer anomaly maps indicate where the density map is able to give a good replication of structures found in the velocity model. By studying the maps, it is determined that some regions closer to the Kii Peninsula are difficult to constrain in the density map due to more variable geological features. However, the regions closer to the trough are simpler to define and likely better replicated in the density map.

Then time-lapse gravity modelling follows three scenarios in which variations in fluid migration are likely to occur. The scenarios model fluid variations along fault planes corresponding to VLFE events or within sedimentary rock sections. All three studied scenarios model variations of water migration that might occur within the

shallow regions of the Nankai trough. These results therefore reflect fluid variations at various depths and extents within the subsurface rocks, leading to observable time-lapse gravity signals at the seafloor.

Hypotheses have been set up following the results of the modelling, assuming that a survey off the Kii Peninsula will likely be able to detect gravity changes caused by fluid migration. By testing these hypotheses through a seafloor gravimetric survey at the Nankai trough, observable changes can be related to processes within the shallow regions of the subduction zone.

Following the discussion in Chapter 7, conducting a time-lapse gravity survey at the seafloor will improve our knowledge of fluid variations occurring within the shallow regions of the subduction zone. Specifically, such a survey will give increased information on the fluid processes triggering slow earthquakes, and may lead to increased information on the location and extent of the fault planes involved in the events. This will improve our knowledge on the asperity distribution within the Nankai trough, as well as stress accumulation along the plate interface. Results of such a survey could therefore have very important implications for earthquake research at the Nankai trough.

Bibliography

(USGS), United Stated Geological Survey (2019). *Earthquake Glossary: Ring of Fire*. URL: https://earthquake.usgs.gov/learn/glossary/?term=Ring%5C%20of%5C%20Fire (visited on 11/06/2019).

Agersborg, R et al. (2017). "Density Changes and Reservoir Compaction from In-situ Calibrated 4D Gravity and Subsidence Measured at the Seafloor". In: *SPE Annual Technical Conference and Exhibition*. Society of Petroleum Engineers.

Agersborg, Remy et al. (2017). "Mapping water influx and hydrocarbon depletion in offshore reservoirs using gravimetry: Requirements on gravimeter calibration". In: *SEG Technical Program Expanded Abstracts 2017*. Society of Exploration Geophysicists, pp. 1803–1807.

Ando, Masataka (1975). "Source mechanisms and tectonic significance of historical earthquakes along the Nankai Trough, Japan". In: *Tectonophysics* 27.2, pp. 119–140.

Araki, Eiichiro et al. (2017). "Recurring and triggered slow-slip events near the trench at the Nankai Trough subduction megathrust". In: *Science* 356.6343, pp. 1157–1160.

Ariyoshi, Keisuke et al. (2014). "The detectability of shallow slow earthquakes by the Dense Oceanfloor Network system for Earthquakes and Tsunamis (DONET) in Tonankai district, Japan". In: *Marine Geophysical Research* 35.3, pp. 295–310.

Ashi, Jun'ichirō, Timothy Byrne, and Asahiko Taira (1992). *Photographic Atlas of an Accretionary Prism: Geologic Structures of the Shimanto Belt, Japan*. Springer.

Audet, Pascal et al. (2010). "Slab morphology in the Cascadia fore arc and its relation to episodic tremor and slip". In: *Journal of Geophysical Research: Solid Earth* 115.B4.

Ballu, Valérie et al. (2009). "A seafloor experiment to monitor vertical deformation at the Lucky Strike volcano, Mid-Atlantic Ridge". In: *Journal of Geodesy* 83.2, p. 147.

Barcheck, C Grace et al. (2012). "The relationship of intermediate-and deep-focus seismicity to the hydration and dehydration of subducting slabs". In: *Earth and Planetary Science Letters* 349, pp. 153–160.

Beroza, Gregory C and Satoshi Ide (2011). "Slow earthquakes and nonvolcanic tremor". In: *Annual review of Earth and planetary sciences* 39, pp. 271–296.

Boggs, Sam (2009). *Petrology of sedimentary rocks*. Cambridge: Cambridge University Press. ISBN: 9780511626487.

Bray, CJ and DE Karig (1985). "Porosity of sediments in accretionary prisms and some implications for dewatering processes". In: *Journal of Geophysical Research: Solid Earth* 90.B1, pp. 768–778.

Brown, KM et al. (2003). "Compositional and fluid pressure controls on the state of stress on the Nankai subduction thrust: A weak plate boundary". In: *Earth and Planetary Science Letters* 214.3-4, pp. 589–603.

Byrne, Daniel E, Dan M Davis, and Lynn R Sykes (1988). "Loci and maximum size of thrust earthquakes and the mechanics of the shallow region of subduction zones". In: *Tectonics* 7.4, pp. 833–857.

Calvert, AJ (2011). "The seismic structure of island arc crust". In: *Arc-continent collision*. Springer, pp. 87–119.

Carlson, RL and CN Herrick (1990). "Densities and porosities in the oceanic crust and their variations with depth and age". In: *Journal of Geophysical Research: Solid Earth* 95.B6, pp. 9153–9170.

Chouet, Bernard A (1996). "Long-period volcano seismicity: its source and use in eruption forecasting". In: *Nature* 380.6572, p. 309.

Clift, Peter and Paola Vannucchi (2004). "Controls on tectonic accretion versus erosion in subduction zones: Implications for the origin and recycling of the continental crust". In: *Reviews of Geophysics* 42.2.

D-map (2019). *D-map, userfriendly GIS*. URL: `https://dmap.no/index.html` (visited on 11/18/2019).

Ding, Min and Jian Lin (2016). "Deformation and faulting of subduction overriding plate caused by a subducted seamount". In: *Geophysical Research Letters* 43.17, pp. 8936–8944.

Douglas, A et al. (2005). "Slow slip on the northern Hikurangi subduction interface, New Zealand". In: *Geophysical Research Letters* 32.16.

Engelder, Terry and NJ Price (1993). "Stress Regimes in the Lithosphere". In: *Engineering Geology* 36.3, pp. 311–311.

Fujiwara, Toshiya, Shusaku Goto, and Kazuo Kobayashi (1998). "Bathymetric and gravity survey of the eastern Nankai Trough". In: *JAMSTEC Journal of Deep Sea Research* 14, pp. 357–361.

Geological Survey of Japan, AIST (2019). *Gravity Database (GALILEO)*. URL: `http://gbank.gsj.jp/gravdb` (visited on 10/18/2019).

Gravitude, OCTIO (2019). *OCTIO Gravitude obtains unprecedented data quality at the Snøhvit, Albatross and Askeladd fields*. URL: `https://www.octio.com/octio-gravitude-obtains-unprecedented-data-quality-at-the-snohvit-albatross-and-askeladd-fields/` (visited on 10/18/2019).

Hashimoto, Mitsuo (1991). *Geology of Japan*. Vol. 8. Springer Science & Business Media.

Hinze, William J, Ralph RB Von Frese, and Afif H Saad (2013). *Gravity and magnetic exploration: Principles, practices, and applications*. Cambridge University Press.

Hirai, Takashi and Takeshi Sagiya (2013). "Biased geodetic inference on asperity distribution on a subducted plate interface: a quantitative study". In: *Earth, Planets and Space* 65.4, pp. 311–321.

Hyndman, RD, K Wang, and M Yamano (1995). "Thermal constraints on the seismogenic portion of the southwestern Japan subduction thrust". In: *Journal of Geophysical Research: Solid Earth* 100.B8, pp. 15373–15392.

Ide, Satoshi et al. (2007). "A scaling law for slow earthquakes". In: *Nature* 447.7140, p. 76.

Ike, Toshihiro et al. (2008). "Variations in sediment thickness and type along the northern Philippine Sea Plate at the Nankai Trough". In: *Island Arc* 17.3, pp. 342–357.

Imanishi, Yuichi et al. (2004). "A network of superconducting gravimeters detects submicrogal coseismic gravity changes". In: *Science* 306.5695, pp. 476–478.

Imbt, William C, Samuel P Ellison, et al. (1946). "Porosity In Limestone And Dolomite Petroleum Reservoir". In: *Drilling and Production Practice*. American Petroleum Institute.

Ito, Takeo, Shoichi Yoshioka, and Shin'ichi Miyazaki (1999). "Interplate coupling in southwest Japan deduced from inversion analysis of GPS data". In: *Physics of the Earth and Planetary Interiors* 115.1, pp. 17–34.

Ito, Yoshihiro and Kazushige Obara (2006). "Very low frequency earthquakes within accretionary prisms are very low stress-drop earthquakes". In: *Geophysical Research Letters* 33.9.

Ito, Yoshihiro, Kazushige Obara, et al. (2007). "Slow earthquakes coincident with episodic tremors and slow slip events". In: *Science* 315.5811, pp. 503–506.

Jacoby, Wolfgang and Peter L Smilde (2009). *Gravity interpretation: fundamentals and application of gravity inversion and geological interpretation*. Springer Science & Business Media.

JAMSTEC (2012). *DONET: Cable information*. URL: `https://www.jamstec.go.jp/donet/e/cable/` (visited on 11/16/2019).

– (2016). *DONET2 installation has been completed and the management of DONET has been transferred from JAMSTEC to NIED*. URL: `http://www.jamstec.go.jp/ceat/e/topics/20160428.html` (visited on 10/18/2019).

– (2019a). *Nankai Trough Seismogenic Zone Experiment*. URL: `https://www.jamstec.go.jp/chikyu/e/nantroseize/` (visited on 10/18/2019).

– (2019b). *DONET system concept*. URL: `https://www.jamstec.go.jp/donet/e/` (visited on 10/18/2019).

Kanamori, Hiroo (1971). "Great earthquakes at island arcs and the lithosphere". In: *Tectonophysics* 12.3, pp. 187–198.

– (1972a). "Mechanism of tsunami earthquakes". In: *Physics of the earth and planetary interiors* 6.5, pp. 346–359.

– (1972b). "Tectonic implications of the 1944 Tonankai and the 1946 Nankaido earthquakes". In: *Physics of the earth and planetary interiors* 5, pp. 129–139.

Kanamori, Hiroo and John J Cipar (1974). "Focal process of the great Chilean earthquake May 22, 1960". In: *Physics of the Earth and Planetary Interiors* 9.2, pp. 128–136.

Kaneda, Yoshiyuki (2014). *Introduction to ocean floor networks and their scientific application.*

Karig, Daniel E (1974). "Evolution of arc systems in the western Pacific". In: *Annual Review of Earth and Planetary Sciences* 2.1, pp. 51–75.

Kato, Teruyuki et al. (2005). "Tsunami due to the 2004 September 5th off the Kii peninsula earthquake, Japan, recorded by a new GPS buoy". In: *Earth, planets and space* 57.4, pp. 297–301.

Katsumata, Akio and Noriko Kamaya (2003). "Low-frequency continuous tremor around the Moho discontinuity away from volcanoes in the southwest Japan". In: *Geophysical Research Letters* 30.1, pp. 20–1.

Kawaguchi, Katsuyoshi et al. (2015). "Construction of the DONET real-time seafloor observatory for earthquakes and tsunami monitoring". In: *SEAFLOOR OBSERVATORIES: A New Vision of the Earth from the Abyss.* Ed. by Paolo Favali, Laura Beranzoli, and Angelo De Santis. Springer Science & Business Media. Chap. 10, pp. 211–228.

Kearey, Philip, Keith A Klepeis, and Frederick J Vine (2009). *Global tectonics.* John Wiley & Sons.

Kehew, Alan E. (Dec. 1994). *Geology For Engineers and Environmental Scientists (2nd Edition).* Prentice Hall. ISBN: 0133035387. URL: `https://www.xarg.org/ref/a/0133035387/`.

Kimura, Gaku, Yujin Kitamura, et al. (2007). "Transition of accretionary wedge structures around the up-dip limit of the seismogenic subduction zone". In: *Earth and Planetary Science Letters* 255.3-4, pp. 471–484.

Kimura, Gaku, Asuka Yamaguchi, et al. (2012). "Tectonic mélange as fault rock of subduction plate boundary". In: *Tectonophysics* 568, pp. 25–38.

Kinoshita, M et al. (2009). "Expedition 314 summary". In: *Proc. IODP— Volume.* Vol. 314. 315/316, p. 2.

– (2012). "Data report: clay mineral assemblages from the Nankai Trough accretionary prism and the Kumano Basin, IODP Expeditions 315 and 316, NanTroSEIZE Stage 1". In: *Proc. IODP— Volume.* Vol. 314. 315/316, p. 2.

Kodaira, Shuichi, Takashi Iidaka, et al. (2004). "High pore fluid pressure may cause silent slip in the Nankai Trough". In: *Science* 304.5675, pp. 1295–1298.

Kodaira, Shuichi, Eiji Kurashimo, et al. (2002). "Structural factors controlling the rupture process of a megathrust earthquake at the Nankai trough seismogenic zone". In: *Geophysical Journal International* 149.3, pp. 815–835.

Kodaira, Shuichi, Narumi Takahashi, et al. (2000). "Western Nankai Trough seismogenic zone: Results from a wide-angle ocean bottom seismic survey". In: *Journal of Geophysical Research: Solid Earth* 105.B3, pp. 5887–5905.

Koike, Nobuaki et al. (2005). "Tsunami run-up heights of the 2004 off the Kii peninsula earthquakes". In: *Earth, planets and space* 57.3, pp. 157–160.

Koketsu, Kazuki, Hiroe Miyake, and Haruhiko Suzuki (2012). "Japan integrated velocity structure model version 1". In: *Proceedings of the 15th World Conference on Earthquake Engineering*. 1773. Lisbon.

Lay, Thorne and Hiroo Kanamori (1981). "An asperity model of large earthquake sequences". In:

Linde, Alan T and I Selwyn Sacks (2002). "Slow earthquakes and great earthquakes along the Nankai trough". In: *Earth and Planetary Science Letters* 203.1, pp. 265–275.

Liu, Xin et al. (2017). "Age of the subducting Pacific slab beneath East Asia and its geodynamic implications". In: *Earth and Planetary Science Letters* 464, pp. 166–174.

Lomnitz, Cinna (2004). "Major earthquakes of Chile: a historical survey, 1535-1960". In: *Seismological Research Letters* 75.3, pp. 368–378.

MathWorks inc. (2018). *MATLAB*. Version R2018a.

Mavko, Gary, Tapan Mukerji, and Jack Dvorkin (2009). *The rock physics handbook: Tools for seismic analysis of porous media*. Cambridge university press.

Miyakawa, A et al. (2015). "Introduction to the Gravity Database (GALILEO) Compiled by the Geological Survey of Japan, AIST". In: *International Symposium on Geodesy for Earthquake and Natural Hazards (GENAH)*. Springer, pp. 135–143.

Moore, Gregory F et al. (2015). "Evolution of tectono-sedimentary systems in the Kumano Basin, Nankai Trough forearc". In: *Marine and Petroleum Geology* 67, pp. 604–616.

Moore, J Casey and Daniel E Karig (1976). "Sedimentology, structural geology, and tectonics of the Shikoku subduction zone, southwestern Japan". In: *Geological Society of America Bulletin* 87.9, pp. 1259–1268.

Moore, J Casey and Demian Saffer (2001). "Updip limit of the seismogenic zone beneath the accretionary prism of southwest Japan: An effect of diagenetic to low-grade metamorphic processes and increasing effective stress". In: *Geology* 29.2, pp. 183–186.

Moore, J Casey and Peter Vrolijk (1992). "Fluids in accretionary prisms". In: *Reviews of Geophysics* 30.2, pp. 113–135.

Mori, Nobuhito et al. (2011). "Survey of 2011 Tohoku earthquake tsunami inundation and run-up". In: *Geophysical research letters* 38.7.

Mulder, Thierry and Heiko Hüneke (2013). "Turbidite". In: *Encyclopedia of Marine Geosciences*, pp. 1–7.

Müller, R Dietmar et al. (2008). "Age, spreading rates, and spreading asymmetry of the world's ocean crust". In: *Geochemistry, Geophysics, Geosystems* 9.4.

Mussett, Alan E and M Aftab Khan (2000). *Looking into the earth: an introduction to geological geophysics*. Cambridge University Press.

Nadeau, Robert M and David Dolenc (2005). "Nonvolcanic tremors deep beneath the San Andreas Fault". In: *Science* 307.5708, pp. 389–389.

Nagy, Dezso, Gabor Papp, and Judit Benedek (2000). "The gravitational potential and its derivatives for the prism". In: *Journal of Geodesy* 74.7-8, pp. 552–560.

Nakanishi, Ayako, Shuichi Kodaira, Seiichi Miura, et al. (2008). "Detailed structural image around splay-fault branching in the Nankai subduction seismogenic zone: Results from a high-density ocean bottom seismic survey". In: *Journal of Geophysical Research: Solid Earth* 113.B3.

Nakanishi, Ayako, Shuichi Kodaira, Jin-Oh Park, et al. (2002). "Deformable backstop as seaward end of coseismic slip in the Nankai Trough seismogenic zone". In: *Earth and Planetary Science Letters* 203.1, pp. 255–263.

Nakanishi, Ayako, Narumi Takahashi, Jin-Oh Park, et al. (2002). "Crustal structure across the coseismic rupture zone of the 1944 Tonankai earthquake, the central Nankai Trough seismogenic zone". In: *Journal of Geophysical Research: Solid Earth* 107.B1, EPM–2.

Nakanishi, Ayako, Narumi Takahashi, Yojiro Yamamoto, et al. (2018). "Three-dimensional plate geometry and P-wave velocity models of the subduction zone in SW Japan: Implications for seismogenesis". In: *Geology and Tectonics of Subduction Zones: A Tribute to Gaku Kimura* 534, p. 69.

Nakano, Masaru, Takane Hori, et al. (2018). "Shallow very-low-frequency earthquakes accompany slow slip events in the Nankai subduction zone". In: *Nature communications* 9.1, p. 984.

Nakano, Masaru, Takeshi Nakamura, et al. (2013). "Intensive seismic activity around the Nankai trough revealed by DONET ocean-floor seismic observations". In: *Earth, Planets and Space* 65.1, pp. 5–15.

Nakano, M et al. (2016). "Ocean floor networks capture low-frequency earthquake event". In: *Eos* 97.

Nawa, Kazunari et al. (2009). "Coseismic change and precipitation effect in temporal gravity variation at Inuyama, Japan: A case of the 2004 off the Kii peninsula earthquakes observed with a superconducting gravimeter". In: *Journal of Geodynamics* 48.1, pp. 1–5.

Noda, Akemi, Tatsuhiko Saito, and Eiichi Fukuyama (2018). "Slip-deficit rate distribution along the Nankai trough, southwest Japan, with elastic lithosphere and viscoelastic asthenosphere". In: *Journal of Geophysical Research: Solid Earth* 123.9, pp. 8125–8142.

Obara, Kazushige (2002). "Nonvolcanic deep tremor associated with subduction in southwest Japan". In: *Science* 296.5573, pp. 1679–1681.

Obara, Kazushige, Hitoshi Hirose, et al. (2004). "Episodic slow slip events accompanied by non-volcanic tremors in southwest Japan subduction zone". In: *Geophysical Research Letters* 31.23.

Obara, Kazushige and Yoshihiro Ito (2005). "Very low frequency earthquakes excited by the 2004 off the Kii peninsula earthquakes: A dynamic deformation process in the large accretionary prism". In: *Earth, Planets and Space* 57.4, pp. 321–326.

Obara, Kazushige and Aitaro Kato (2016). "Connecting slow earthquakes to huge earthquakes". In: *Science* 353.6296, pp. 253–257.

OCTIO Gravitude (2014). *GravMod*.

Okada, Y (2013). "Recent progress of seismic observation networks in Japan". In: *Journal of Physics: Conference Series*. Vol. 433. 1. IOP Publishing, p. 012039.

Okino, Kyoko, Yasue Shimakawa, and Shinji Nagaoka (1994). "Evolution of the Shikoku basin". In: *Journal of geomagnetism and geoelectricity* 46.6, pp. 463–479.

Panet, Isabelle et al. (2018). "Migrating pattern of deformation prior to the Tohoku-Oki earthquake revealed by GRACE data". In: *Nature Geoscience* 11.5, p. 367.

Park, Jin-Oh et al. (2004). "A subducted oceanic ridge influencing the Nankai megathrust earthquake rupture". In: *Earth and Planetary Science Letters* 217.1-2, pp. 77–84.

Pruis, Matthew J and H Paul Johnson (2002). "Age dependent porosity of young upper oceanic crust: Insights from seafloor gravity studies of recent volcanic eruptions". In: *Geophysical Research Letters* 29.5, pp. 20–1.

Radford, Collin (2016). *Japanese Encyclopedia: Kansai Region*. URL: `https://matcha-jp.com/en/1365` (visited on 10/06/2019).

Raeesi, M and K Atakan (2009). "On the deformation cycle of a strongly coupled plate interface: The triple earthquakes of 16 March 1963, 15 November 2006, and 13 January 2007 along the Kurile subduction zone". In: *Journal of Geophysical Research: Solid Earth* 114.B10.

Raimbourg, Hugues et al. (2014). "Long-term evolution of an accretionary prism: The case study of the Shimanto Belt, Kyushu, Japan". In: *Tectonics* 33.6, pp. 936–959.

Ringwood, Alfred Edward (1974). "The petrological evolution of island arc systems: Twenty-seventh William Smith Lecture". In: *Journal of the Geological Society* 130.3, pp. 183–204.

Rogers, Garry and Herb Dragert (2003). "Episodic tremor and slip on the Cascadia subduction zone: The chatter of silent slip". In: *Science* 300.5627, pp. 1942–1943.

Ruff, Larry and Hiroo Kanamori (1983). "Seismic coupling and uncoupling at subduction zones". In: *Tectonophysics* 99.2-4, pp. 99–117.

Ruiz, Hugo et al. (2016). "Monitoring offshore reservoirs using 4D gravity and subsidence with improved tide corrections". In: *SEG Technical Program Expanded Abstracts 2016*. Society of Exploration Geophysicists, pp. 2946–2950.

Sacks, I Selwyn et al. (1978). "Slow earthquakes and stress redistribution". In: *Nature* 275.5681, p. 599.

Saffer, Demian M and Barbara A Bekins (2006). "An evaluation of factors influencing pore pressure in accretionary complexes: Implications for taper angle and wedge mechanics". In: *Journal of Geophysical Research: Solid Earth* 111.B4.

Saffer, Demian M and Laura M Wallace (2015). "The frictional, hydrologic, metamorphic and thermal habitat of shallow slow earthquakes". In: *Nature Geoscience* 8.8, p. 594.

Saito, Tatsuhiko, Kenji Satake, and Takashi Furumura (2010). "Tsunami waveform inversion including dispersive waves: the 2004 earthquake off Kii Peninsula, Japan". In: *Journal of Geophysical Research: Solid Earth* 115.B6.

Satake, Kenji (2015). "Geological and historical evidence of irregular recurrent earthquakes in Japan". In: *Philosophical Transactions of the Royal Society A: Mathematical, Physical and Engineering Sciences* 373.2053, p. 20140375.

Schön, Jürgen H (2015). *Physical properties of rocks: Fundamentals and principles of petrophysics*. Vol. 65. Elsevier.

Schwartz, Susan Y and Juliana M Rokosky (2007). "Slow slip events and seismic tremor at circum-Pacific subduction zones". In: *Reviews of Geophysics* 45.3.

Screaton, E et al. (2009). "Interactions between deformation and fluids in the frontal thrust region of the NanTroSEIZE transect offshore the Kii Peninsula, Japan: Results from IODP Expedition 316 Sites C0006 and C0007". In: *Geochemistry, Geophysics, Geosystems* 10.12.

Seno, Tetsuzo, Seth Stein, and Alice E Gripp (1993). "A model for the motion of the Philippine Sea plate consistent with NUVEL-1 and geological data". In: *Journal of Geophysical Research: Solid Earth* 98.B10, pp. 17941–17948.

Shelly, David R et al. (2006). "Low-frequency earthquakes in Shikoku, Japan, and their relationship to episodic tremor and slip". In: *Nature* 442.7099, p. 188.

Song, Teh-Ru Alex and Mark Simons (2003). "Large trench-parallel gravity variations predict seismogenic behavior in subduction zones". In: *Science* 301.5633, pp. 630–633.

Stein, S, M Wysession, and H Houston (2003). "Books-An Introduction to Seismology, Earthquakes, and Earth Structure". In: *Physics Today* 56.10, pp. 65–72.

Sugimura, A and S Uyeda (1973). "Developments in Geotectonics 3: Island Arcs, Japan and its Environs". In:

Sugioka, Hiroko et al. (2012). "Tsunamigenic potential of the shallow subduction plate boundary inferred from slow seismic slip". In: *Nature Geoscience* 5.6, p. 414.

Taira, A, I Hill, et al. (1992). "Sediment deformation and hydrogeology of the Nankai Trough accretionary prism: Synthesis of shipboard results of ODP Leg 131". In: *Earth and Planetary Science Letters* 109.3-4, pp. 431–450.

Taira, A, H Okada, et al. (1982). "The Shimanto Belt of Japan: cretaceous-lower Miocene active-margin sedimentation". In: *Geological Society, London, Special Publications* 10.1, pp. 5–26.

Taira, Asahiko (2001). "Tectonic evolution of the Japanese island arc system". In: *Annual Review of Earth and Planetary Sciences* 29.1, pp. 109–134.

Takemura, Shunsuke, Hisahiko Kubo, et al. (2019). "Modeling of long-period ground motions in the Nankai subduction zone: model simulation using the accretionary prism derived from oceanfloor local S-wave velocity structures". In: *Pure and Applied Geophysics* 176.2, pp. 627–647.

Takemura, Shunsuke, Takanori Matsuzawa, Takeshi Kimura, et al. (2018). "Centroid Moment Tensor Inversion of Shallow Very Low Frequency Earthquakes Off the Kii Peninsula, Japan, Using a Three-Dimensional Velocity Structure Model". In: *Geophysical Research Letters* 45.13, pp. 6450–6458.

Takemura, Shunsuke, Takanori Matsuzawa, Akemi Noda, et al. (2019). "Structural Characteristics of the Nankai Trough Shallow Plate Boundary Inferred From Shallow Very Low Frequency Earthquakes". In: *Geophysical Research Letters* 46.8, pp. 4192–4201.

To, Akiko et al. (2015). "Small size very low frequency earthquakes in the Nankai accretionary prism, following the 2011 Tohoku-Oki earthquake". In: *Physics of the Earth and Planetary Interiors* 245, pp. 40–51.

Tomoda, Yoshibumi (2010). "Gravity at sea—A memoir of a marine geophysicist—". In: *Proceedings of the Japan Academy, Series B* 86.8, pp. 769–787.

Tonegawa, Takashi et al. (2017). "Sporadic low-velocity volumes spatially correlate with shallow very low frequency earthquake clusters". In: *Nature communications* 8.1, p. 2048.

Tsuboi, Seiji and Takeshi Nakamura (2013). "Sea surface gravity changes observed prior to March 11, 2011 Tohoku earthquake". In: *Physics of the Earth and Planetary Interiors* 221, pp. 60–65.

Tsuji, Takeshi, Juichiro Ashi, et al. (2015). "Identification of the static backstop and its influence on the evolution of the accretionary prism in the Nankai Trough". In: *Earth and Planetary Science Letters* 431, pp. 15–25.

Tsuji, Takeshi, Shohei Minato, et al. (2017). "3D geometry of a plate boundary fault related to the 2016 Off-Mie earthquake in the Nankai subduction zone, Japan". In: *Earth and Planetary Science Letters* 478, pp. 234–244.

Underwood, Michael B and Kevin T Pickering (1996). "Clay-mineral provenance, sediment dispersal patterns, and mudrock diagenesis in the Nankai accretionary prism, southwest Japan". In: *Clays and Clay Minerals* 44.3, pp. 339–356.

Underwood, Michael B and Chen Song (2016). "Data report: Clay mineral assemblages in cuttings from Hole C0002F, IODP Expedition 338, upper Nankai Trough accretionary prism". In: *Strasser, M., Dugan, B., Kanagawa, K., Moore, GF, Toczko, S., Maeda, L. and the Expedition 338 Scientists, Proc. IODP* 338.

Uyeda, Seiya and Hiroo Kanamori (1979). "Back-arc opening and the mode of subduction". In: *Journal of Geophysical Research: Solid Earth* 84.B3, pp. 1049–1061.

Wells, Donald L and Kevin J Coppersmith (1994). "New empirical relationships among magnitude, rupture length, rupture width, rupture area, and surface dis-

placement". In: *Bulletin of the seismological Society of America* 84.4, pp. 974–1002.

Wells, Ray E et al. (2003). "Basin-centered asperities in great subduction zone earthquakes: A link between slip, subsidence, and subduction erosion?" In: *Journal of Geophysical Research: Solid Earth* 108.B10.

Yamamoto, Yojiro et al. (2013). "Imaging of the subducted Kyushu-Palau Ridge in the Hyuga-nada region, western Nankai Trough subduction zone". In: *Tectonophysics* 589, pp. 90–102.

– (2014). "Seismicity and structural heterogeneities around the western Nankai Trough subduction zone, southwestern Japan". In: *Earth and Planetary Science Letters* 396, pp. 34–45.

Yamashita, Y et al. (2015). "Migrating tremor off southern Kyushu as evidence for slow slip of a shallow subduction interface". In: *Science* 348.6235, pp. 676–679.

Yokota, Yusuke et al. (2016). "Seafloor geodetic constraints on interplate coupling of the Nankai Trough megathrust zone". In: *Nature* 534.7607, p. 374.

Young, Hugh and Roger A Freedman (2016). *Sears and Zemansky's university physics : with modern physics*. Boston: Pearson. ISBN: 1292100311.

Zumberge, Mark et al. (2008). "Precision of seafloor gravity and pressure measurements for reservoir monitoring". In: *Geophysics* 73.6, WA133–WA141.

Appendices

Appendix A

Matlab code

A.1 Implementing the geological model

The function below shows how the geological model has been implemented in a simple way for use through the modelling.

```
%% Creating structure with properties for each layer
% The properties include:
%     - Location of layer in the geological model
%     - Predefined velocity intervals for the layers
%     - Effective bulk and shear modulus for each rock within
    a layer
%     - Porosity values for the rocks
%     - Conversion factor to use in density mapping
%     - Velocity indices corresponding to each layer
%     - Mineral bulk and shear modulus (for rock layers)

% Function input:
%     - Vp: P-wave velocity array
%     - depth: depth array correspnding to P-wave velocities
%     - latitude: Latitude array, for use in finding rock
   indices

% Output:
% rocks: Structure with rock properties

function [rocks] = RockStructure(Vp, depth, latitude)
% Location of layers in the model
```

```
21 locations = {'Air','Sea','Top sediment layer', 'Second
     sediment layer',...
22     'Bottom sediment layer','Old accretionary prism','Lower
         crust 1',...
23     'Lower crust 2','Upper mantle','Ocean layer 2','Ocean
         layer 3','Upper mantle'};
24
25 % Velocity range (m/s) of all layers:
26 velocities =
     {[0,1400],[1400,1600],[1600,2046],[2046,3115],[3115,4700],...

27         [4700,5700],[5700,6349],[6349,7200],[7200,8177],...
28         [4520,6349],[6349,7200],[7200,8177]};
29
30 % Finding velocities corresponding to each layer in the 3D
     velocity model:
31 groupInds = find_rock_type_indices(Vp, velocities, depth,
     latitude);
32
33 % Porosity (fraction) of rocks:
34 phi = [0.7, 0.55, 0.25, 0.25, 0.05, 0.1, 0.1, 0.15, 0.1,
     0.1];
35
36 % Mineral bulk and shear modulus (GPa):
37 S_m = {6.85, [15.6, 11.7], 15, 32, [15, 57], 57, 80,[15,
     57], 57, 80};
38 K_m = {20.9, [12.3,39.4], 37.5, 76.8, [35.7, 94.1],
     94.1,130,[35.7, 94.1], 94.1,130};
39
40 % Bulk and shear moduli of the pore fluid and air (GPa):
41 K_f = 2.34;
42 K_air = K_f/1e12;
43
44 S_f = 0;
45 S_air = 0;
46
47 % Using Hashin-Shtrikman upper bound to calculate effective
     bulk modulus
48 K_eff = zeros(1,length(K_m));
49 S_eff = zeros(1,length(K_m));
50 for i=1:length(K_m)
51     if length(K_m{i})==1
```

```
52          % Hashin-Shtrikman upper bounds, one dominant
                mineral
53          [K_eff(i), S_eff(i)] = upperHS(K_m{i}, S_m{i}, 1,
                K_f, S_f, phi(i));
54      else
55          % Hashin-Shtrikman upper bounds, two dominant
                minerals
56          [K_eff(i), S_eff(i)] = upperHS(K_m{i}, S_m{i}, 2,
                K_f, S_f, phi(i));
57      end
58  end
59
60  % Effective bulk and shear modulus for all layers:
61  K_eff = [K_air, K_f, K_eff].*1e9; % Pa
62  S_eff = [S_air, S_f, S_eff].*1e9; % Pa
63
64  % Porosity for all layers (defined as 1 for air and sea
        layers):
65  phi = [1, 1, phi];                  % Fraction
66
67  % Creating structure of layers and their properties:
68  rocks = struct();
69  for r=1:length(velocities)
70      rocks(r).Location = locations{r};
71      rocks(r).Velocity = velocities{r};
72      rocks(r).Shear = S_eff(r);
73      rocks(r).Bulk = K_eff(r);
74      rocks(r).Porosity = phi(r);
75      rocks(r).alpha = (rocks(r).Bulk + (4/3)*rocks(r).Shear)
            /(((rocks(r).Velocity(1)+rocks(r).Velocity(2))/2)^3);
76      rocks(r).groupInds = groupInds{r};
77      % Add mineral bulk and shear modulus corresponding to
            rock layers:
78      if r>2
79          rocks(r).minBulk = K_m{r-2};
80          rocks(r).minShear = S_m{r-2};
81      end
82  end
83  end
```

A.2 Computing densities

The following function computes densities for each layer, given the rock structure with known velocity indices for each layer, the conversion factor (α) and the velocity ranges.

```
%% Creating the density map:
% Input:
%     - Vp: array of all velocity values to convert
%     - rockstruct: structure with rock properties

% Output:
%     - densities: converted densities

function [densities] = vp2Density(Vp, rockstruct)

% Applying velocity-to-density conversion for all layers:
densities = zeros(size(Vp));
for j = 1:length(rockstruct)
    densities(rockstruct(j).groupInds) = rockstruct(j).alpha
       *Vp(rockstruct(j).groupInds);
end
end
```

Appendix B

Additional results

B.1 Comparison of deep and shallow VLFE events

The Figures added in this section show the results of the test on the 2015 and 2016 VLFE episodes, where the deeper events down to < 15 km are included to show how much it affects the results.

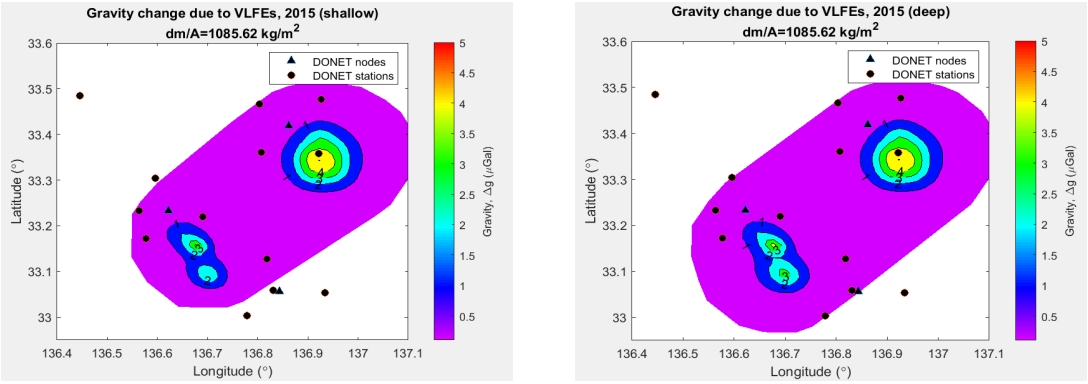

(a) 2015 episode with events above $10km$

(b) 2015 episode with events above $15km$.

Figure B.1: Gravity signal for 2015 episode as defined by Masaru Nakano, Hori, et al. (2018) and Nakano et al. (2016).

For the 2015 episode, the mass added per square kilometer is no different when adding the deeper events. The gravity signal, however, extends over a slightly larger area between the C and D nodes. The gravity signal from the 2016 episode is similar when adding the deeper events, suggesting that inclusion of the deeper events leads to a similar gravity signal at the surface.

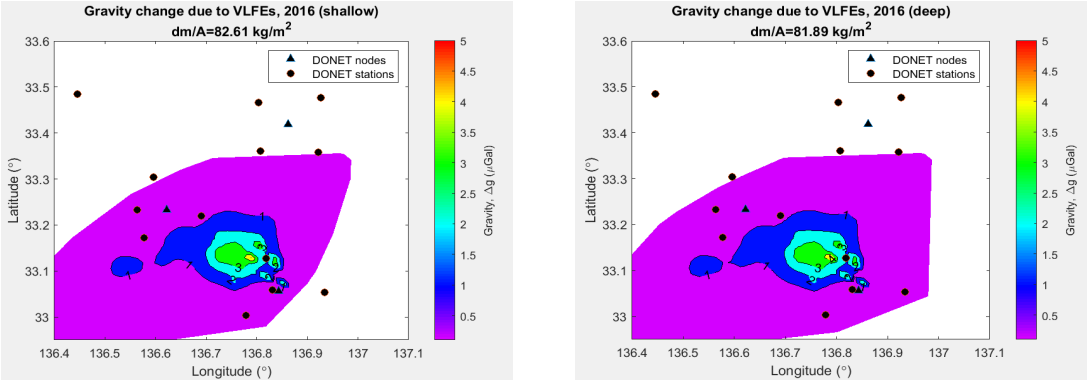

(a) Including only events above $10km$ (b) Including events above $15km$.

Figure B.2: Gravity signal for 2016 episode as defined by Masaru Nakano, Hori, et al. (2018) and Nakano et al. (2016).

B.2 Comparison of various box size, March 2009 episode

For the 2009 episode defined by Sugioka et al. (2012), the additional results include the gravity signal from the boxes with a 1.5×1.5 km size and the boxes with 2.4×2.4 km size, and are shown in Figure B.3. The signals are fairly similar, however more volume is needed for the larger boxes to observe a gravity signal.

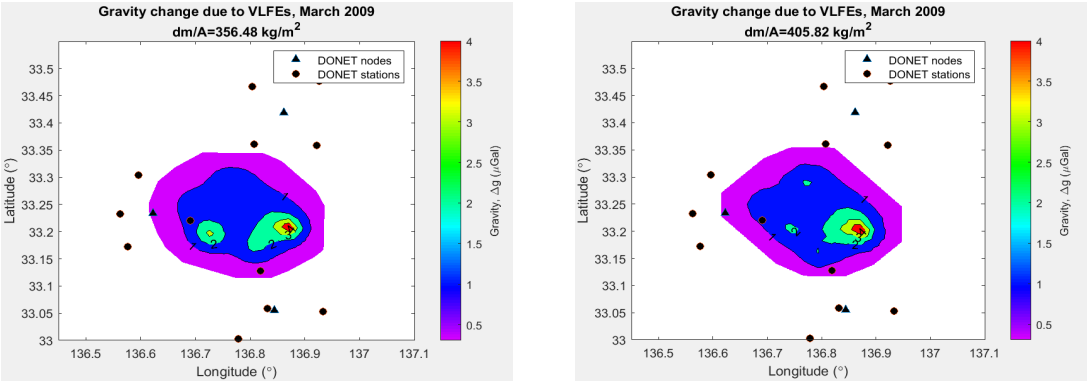

(a) 1.5×1.5 km boxes. (b) 2.4×2.4 km boxes.

Figure B.3: Gravity signal for the two different box sizes used for the 2009 episode as defined by Sugioka et al. (2012).

B.3 Increasing boxes for 2004 and 2009 episodes

The results for the 2004 and 2009 episodes defined by Takemura, Matsuzawa, Noda, et al. (2019) are given here, showing how the gravity signal is affected by increasing the number of boxes used to represent each VLFE location. Increasing the boxes for

the two episodes gives a slightly broader signal for the time-lapse gravity, however it is still difficult to interpret the results from these events.

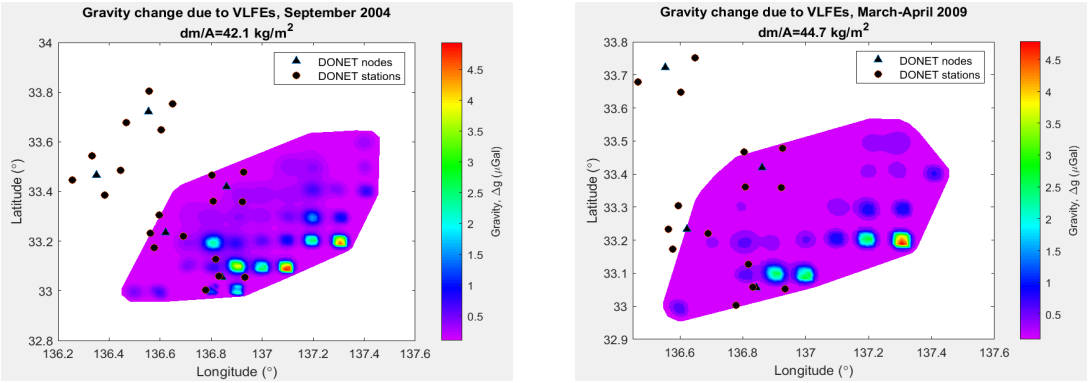

(a) Results for 2004 episode.

(b) Results for 2009 episode

Figure B.4: Results for 2004 and 2009 episodes, as defined by Takemura, Matsuzawa, Noda, et al. (2019), with increased boxes around the separate VLFE coordinates.

Appendix C

Extended data

C.1 VLFE episodes

Table C.1: 2015 episode as defined by Masaru Nakano, Hori, et al. (2018) and Nakano et al. (2016)

Date (dd.mm.yyyy)			Latitude (°)	Longitude (°)	Depth (kmbsl)	M_w
27	10	2015	33.16	136.67	5	3.3
25	10	2015	33.06	136.69	14	3.5
25	10	2015	33.18	136.64	6	3.3
25	10	2015	33.09	136.71	7	3.1
25	10	2015	33.1	136.69	7	3
24	10	2015	33.21	136.6	15	3.4
24	10	2015	33.37	136.95	7	3
24	10	2015	33.4	136.93	6	3.2
24	10	2015	33.1	136.67	13	3
24	10	2015	33.07	136.5	15	3.9
24	10	2015	33.08	136.71	30	3.6
24	10	2015	33.35	136.91	6	3.4
24	10	2015	33.34	136.94	7	3.2
24	10	2015	33.35	136.94	7	3.1
24	10	2015	33.34	136.94	7	3.1
24	10	2015	33.34	136.94	7	3.1
24	10	2015	33.36	136.94	7	3
24	10	2015	33.34	136.94	7	3.2
24	10	2015	33.32	136.95	7	3.1
24	10	2015	33.32	136.95	7	3.3
24	10	2015	33.33	136.94	7	3.1
24	10	2015	33.32	136.91	6	3.2

Table C.1 continued from previous page

24	10	2015	33.34	136.91	7	3.2
21	10	2015	33.29	137.09	20	4.1
21	10	2015	33.25	136.73	8	3.9
20	10	2015	33.16	136.67	5	3.3
20	10	2015	33.18	136.64	6	3.2
25	9	2015	32.82	135.19	7	3.8
25	9	2015	32.83	135.19	6	3.6
21	9	2015	32.78	135.07	9	3.4
15	9	2015	32.85	135.11	10	3
13	9	2015	32.85	135.27	7	3.2
12	9	2015	32.87	135.15	7	3.6
12	9	2015	32.82	135.24	11	3.7
12	9	2015	32.82	135.24	11	3.5
9	9	2015	32.8	135.21	11	4.3
9	9	2015	32.83	135.08	10	4.1
9	9	2015	32.83	135.22	6	3.8
5	9	2015	32.85	135.13	10	3.3
5	9	2015	32.88	135.16	7	3.5
5	9	2015	32.6	135.19	13	4
5	9	2015	32.88	135.15	7	3.8
5	9	2015	32.86	135.13	9	3.7
4	9	2015	32.82	135.13	13	3.2
4	9	2015	32.87	135.21	7	3.6
2	9	2015	32.83	135.14	9	3.5
1	9	2015	32.87	135.12	5	4.2
1	9	2015	32.82	135.24	8	3.9
1	9	2015	32.83	135.21	11	4
1	9	2015	32.86	135.24	7	3.4
1	9	2015	32.86	135.24	7	3.6
1	9	2015	32.87	135.18	7	3.6
1	9	2015	32.83	135.18	6	3.8
1	9	2015	32.85	135.13	9	4.1
25	8	2015	32.9	135.15	7	3.6
10	8	2015	32.88	135.16	7	3.5

Table C.2: 2016 episode as defined by Masaru Nakano, Hori, et al. (2018) and Nakano et al. (2016)

Date (dd.mm.yyyy)			Latitude (°)	Longitude (°)	Depth (kmbsl)	M_w
28	4	2016	32.64	134.52	7	2.8
28	4	2016	32.62	134.53	7	3.2

Table C.2 continued from previous page

26	4	2016	32.63	134.42	11	3.4
26	4	2016	32.62	134.49	11	3.4
26	4	2016	32.61	134.49	12	3.5
25	4	2016	32.64	134.43	11	3.3
25	4	2016	32.66	134.49	7	2.7
25	4	2016	32.63	134.53	9	3.1
25	4	2016	32.66	134.52	9	2.8
25	4	2016	32.62	134.51	10	2.9
24	4	2016	32.66	134.47	7	2.9
24	4	2016	32.66	134.49	7	2.9
24	4	2016	32.67	134.5	6	2.8
24	4	2016	32.67	134.5	7	2.6
24	4	2016	32.66	134.49	7	2.6
24	4	2016	32.61	134.47	12	2.9
24	4	2016	32.66	134.52	15	3.3
24	4	2016	32.61	134.52	9	3.2
24	4	2016	32.68	134.51	6	3
24	4	2016	32.67	134.48	8	3.1
24	4	2016	32.61	134.49	11	3
24	4	2016	32.67	134.5	8	2.9
24	4	2016	32.63	134.54	7	3.4
24	4	2016	32.62	134.48	9	2.6
24	4	2016	32.68	134.46	10	3.4
24	4	2016	32.66	134.48	6	3
24	4	2016	32.68	134.41	8	3.3
23	4	2016	32.67	134.48	6	2.9
23	4	2016	32.67	134.48	7	2.9
23	4	2016	32.66	134.48	6	2.9
21	4	2016	32.99	136.8	6	2.8
17	4	2016	33.1	136.74	3	2.4
17	4	2016	33.12	136.83	7	3.1
17	4	2016	33.09	136.82	4	2.2
17	4	2016	33.08	136.85	4	2.5
16	4	2016	33.1	136.74	7	3
16	4	2016	33.13	136.74	6	2.9
16	4	2016	33.13	136.74	6	2.6
16	4	2016	33.18	136.87	7	3.6
16	4	2016	33.19	136.85	7	3.2
16	4	2016	33.19	136.85	7	3.1
16	4	2016	33.14	136.76	7	3.3

Table C.2 continued from previous page

16	4	2016	33.16	136.76	5	4
16	4	2016	33.12	136.84	4	2.6
16	4	2016	33.15	136.8	7	3.3
16	4	2016	33.14	136.81	6	3.4
16	4	2016	33.13	136.79	5	2.5
16	4	2016	33.13	136.79	5	2.2
16	4	2016	33.21	136.83	6	3.1
16	4	2016	33.25	136.85	7	3.6
16	4	2016	33.1	136.77	7	2.8
16	4	2016	33.23	136.89	8	3.3
16	4	2016	33.1	136.74	7	2.9
16	4	2016	33.18	136.8	6	2.8
16	4	2016	33.05	136.98	12	3.5
16	4	2016	33.2	136.8	7	3
16	4	2016	33.23	136.89	15	3
16	4	2016	33.24	136.83	6	3.2
16	4	2016	33.2	136.81	6	3.1
16	4	2016	33.2	136.81	6	2.7
16	4	2016	33.17	136.8	5	3
16	4	2016	33.17	136.81	6	3.2
16	4	2016	33.29	136.84	7	3.5
16	4	2016	33.15	136.78	8	3.8
16	4	2016	33.24	136.8	7	3.6
16	4	2016	33.15	136.73	6	3
16	4	2016	33.26	136.86	7	3.6
16	4	2016	33.18	136.8	6	3
16	4	2016	33.18	136.8	6	2.9
13	4	2016	33.21	136.84	6	3.5
13	4	2016	33.21	136.82	6	3.1
13	4	2016	33.22	136.82	12	3.7
12	4	2016	33.21	136.82	6	3
12	4	2016	33.13	136.74	6	2.8
12	4	2016	33.14	136.72	5	3
11	4	2016	33.14	136.84	3	2.8
11	4	2016	33.14	136.52	7	2.9
11	4	2016	33.13	136.78	6	2.5
11	4	2016	33.13	136.77	6	3
11	4	2016	33.12	136.73	7	3.1
11	4	2016	33.13	136.72	7	3.3
11	4	2016	33.11	136.81	6	3.4

Table C.2 continued from previous page

11	4	2016	33.14	136.75	6	2.8
11	4	2016	33.1	136.75	6	2.6
11	4	2016	33.05	136.86	3	2.3
11	4	2016	33.1	136.9	19	3.6
11	4	2016	33.18	136.71	6	3.5
11	4	2016	33.14	136.75	6	3.2
11	4	2016	33.16	136.76	8	3.4
11	4	2016	33.15	136.74	6	2.6
11	4	2016	33.15	136.74	7	3
11	4	2016	33.17	136.77	6	3.3
11	4	2016	33.15	136.77	6	3.6
11	4	2016	33.12	136.77	6	2.8
11	4	2016	33.13	136.63	8	3.3
11	4	2016	33.13	136.79	4	2.4
11	4	2016	33.17	136.79	6	2.9
11	4	2016	33.14	136.77	8	2.9
11	4	2016	33.15	136.74	15	3.8
11	4	2016	33.11	136.76	7	3.3
11	4	2016	33.11	136.76	7	3.1
11	4	2016	33.17	136.79	7	3.6
11	4	2016	33.09	136.78	6	3
11	4	2016	33.14	136.75	6	2.9
11	4	2016	33.15	136.74	6	3
11	4	2016	33.18	136.78	6	2.8
11	4	2016	33.16	136.83	7	3.3
11	4	2016	33.15	136.75	6	2.9
11	4	2016	33.15	136.73	6	3.1
11	4	2016	33.16	136.77	6	2.9
11	4	2016	33.06	136.76	6	3.3
11	4	2016	33.08	136.75	5	3.1
11	4	2016	33.13	136.84	4	2.8
11	4	2016	33.15	136.76	6	3.1
10	4	2016	33.15	136.82	7	3.3
10	4	2016	33.13	136.8	5	2.8
10	4	2016	33.11	136.81	6	3.3
10	4	2016	33.11	136.81	6	2.6
10	4	2016	33.16	136.76	6	3.2
10	4	2016	33.13	136.78	3	2.3
10	4	2016	33.2	136.77	7	3.2
10	4	2016	33.2	136.77	7	3

Table C.2 continued from previous page

10	4	2016	33.15	136.77	6	3.1
10	4	2016	33.15	136.76	6	2.8
10	4	2016	33.13	136.62	6	3.1
10	4	2016	33.12	136.83	5	2.9
10	4	2016	33.15	136.77	6	3.3
10	4	2016	33.19	136.72	7	3.5
10	4	2016	33.17	136.77	6	3.6
10	4	2016	33.14	136.72	6	3
10	4	2016	33.14	136.65	7	3.1
10	4	2016	33.13	136.72	5	3
10	4	2016	33.11	136.42	5	2.9
10	4	2016	33.1	136.73	7	3.3
10	4	2016	33.14	136.82	7	3.1
10	4	2016	33.16	136.76	6	3
10	4	2016	33.13	136.75	7	2.6
10	4	2016	33.13	136.75	7	2.5
10	4	2016	33.1	136.78	5	3
10	4	2016	33.2	136.75	7	3.3
10	4	2016	33.12	136.77	6	2.7
10	4	2016	33.15	136.73	6	3.3
10	4	2016	33.11	136.76	7	2.4
10	4	2016	33.14	136.76	7	3.1
10	4	2016	33.11	136.75	7	2.8
10	4	2016	33.11	136.75	7	2.5
10	4	2016	33.1	136.75	6	3.1
10	4	2016	33.27	136.83	7	3.6
10	4	2016	33.27	136.83	7	3.8
10	4	2016	33.28	136.83	6	3.5
10	4	2016	33.28	136.79	6	3.7
10	4	2016	33.22	136.71	7	3.5
10	4	2016	33.22	136.71	7	3.6
10	4	2016	33.11	136.76	6	2.9
10	4	2016	33.14	136.72	7	3
10	4	2016	33.13	136.73	7	3.1
10	4	2016	33.11	136.73	7	3.1
10	4	2016	33.16	136.81	4	3.2
10	4	2016	33.14	136.74	7	2.6
10	4	2016	33.22	136.76	6	3.1
10	4	2016	33.14	136.73	7	3
10	4	2016	33.17	136.77	6	2.4

Table C.2 continued from previous page

10	4	2016	33.27	136.74	6	3.7
10	4	2016	33.23	136.74	7	4
10	4	2016	33.14	136.76	7	3.5
10	4	2016	33.11	136.76	7	2.9
10	4	2016	33.15	136.74	7	3.1
10	4	2016	33.24	136.71	7	3.5
10	4	2016	33.19	136.75	6	2.8
10	4	2016	33.19	136.72	5	3
10	4	2016	33.24	136.72	8	3.5
10	4	2016	33.14	136.76	7	3.1
10	4	2016	33.14	136.76	7	2.8
10	4	2016	33.11	136.8	6	2.6
10	4	2016	33.09	136.8	5	2.4
10	4	2016	33.11	136.7	7	2.8
10	4	2016	33.09	136.73	7	3
10	4	2016	33.09	136.73	7	2.3
9	4	2016	33.09	136.08	6	2.8
9	4	2016	33.12	136.77	6	2.6
9	4	2016	33.13	136.73	6	3
9	4	2016	33.12	136.77	6	2.8
9	4	2016	33.13	136.74	7	2.8
9	4	2016	33.12	136.72	7	3.1
9	4	2016	33.13	136.74	7	3
9	4	2016	33.14	136.8	7	2.8
9	4	2016	33.07	136.73	12	3.1
9	4	2016	33.15	136.5	9	3.7
9	4	2016	33.08	136.08	7	3.2
9	4	2016	33.15	136.09	4	3.1
9	4	2016	33.14	136.72	6	3.1
9	4	2016	33.13	136.74	7	2.7
9	4	2016	33.1	136.75	7	3
9	4	2016	33.15	136.73	6	3
9	4	2016	33.12	136.72	7	3
9	4	2016	33.12	136.72	7	2.9
9	4	2016	33.1	136.79	6	2.6
9	4	2016	33.14	136.74	6	2.8
9	4	2016	33.11	136.7	7	3.3
9	4	2016	33.15	136.73	6	2.9
9	4	2016	33.13	136.78	5	2.4
9	4	2016	33.16	136.83	7	3.2

Table C.2 continued from previous page

9	4	2016	33.13	136.74	7	2.9
9	4	2016	33.12	136.73	6	3.2
9	4	2016	33.11	136.76	6	2.6
9	4	2016	33.14	136.72	6	3.2
8	4	2016	33.14	136.73	7	3.2
8	4	2016	33.14	136.74	6	2.9
8	4	2016	33.11	136.71	6	3.1
8	4	2016	33.04	136.74	12	3.3
8	4	2016	33.11	136.51	7	3.1
8	4	2016	33.21	136.86	12	3.3
8	4	2016	33.15	136.7	10	3.1
8	4	2016	33.13	136.63	9	3.4
8	4	2016	33.09	136.59	7	3.2
8	4	2016	33.09	136.59	7	3.4
8	4	2016	33.14	136.74	6	2.8
8	4	2016	33.13	136.73	7	2.8
8	4	2016	33.13	136.72	7	2.8
8	4	2016	33.18	136.64	6	3
8	4	2016	33.16	136.67	6	3.6
8	4	2016	33.17	136.64	7	2.8
8	4	2016	33.17	136.64	7	3.1
8	4	2016	33.09	136.77	6	2.7
8	4	2016	33.07	136.68	16	3.3
8	4	2016	33.12	136.73	7	2.9
8	4	2016	33.13	136.74	7	2.6
8	4	2016	33.13	136.74	7	2.9
8	4	2016	33.11	136.77	6	2.4
8	4	2016	33.1	136.75	7	2.4
8	4	2016	33.1	136.75	7	2.6
8	4	2016	33.15	136.73	6	2.8
8	4	2016	33.09	136.73	7	2.9
8	4	2016	33.15	136.73	6	2.9
8	4	2016	33.13	136.72	7	2.9
8	4	2016	33.14	136.72	6	3.4
8	4	2016	33.14	136.73	7	2.9
8	4	2016	33.24	136.7	6	3.7
8	4	2016	33.2	136.74	7	3.3
8	4	2016	33.2	136.74	7	3.2
8	4	2016	33.16	136.72	7	3.1
8	4	2016	33.13	136.73	7	2.8

Table C.2 continued from previous page

8	4	2016	33.1	136.74	7	3.2
8	4	2016	33.12	136.72	7	3.2
8	4	2016	33.04	136.86	4	2.9
8	4	2016	33.14	136.72	6	3.4
8	4	2016	33.11	136.75	10	3.1
7	4	2016	33.14	136.72	6	3.2
7	4	2016	33.14	136.72	6	2.9
7	4	2016	33.17	136.63	6	3.1
7	4	2016	33.14	136.74	6	2.9
7	4	2016	33.09	136.77	11	3.3
7	4	2016	33.12	136.72	7	3.1
7	4	2016	33.05	136.73	10	3.3
7	4	2016	33.18	136.74	6	2.9
7	4	2016	33.12	136.74	9	2.7
7	4	2016	33.18	136.59	5	2.9
7	4	2016	33.1	136.67	13	3.2
7	4	2016	33.18	136.7	10	3.3
7	4	2016	33.09	136.66	12	3.3
7	4	2016	33.04	136.8	3	2.6
7	4	2016	33.11	136.71	7	2.7
7	4	2016	33.14	136.71	8	3.2
7	4	2016	33.09	136.72	7	2.8
7	4	2016	33.09	136.72	7	3.2
7	4	2016	33.09	136.71	7	2.9
7	4	2016	33.1	136.73	7	2.8
7	4	2016	33.14	136.63	6	3.1
7	4	2016	33.1	136.74	7	2.8
7	4	2016	33.05	136.69	13	3.5
7	4	2016	33.16	136.67	6	3.2
7	4	2016	33.11	136.67	15	3.5
7	4	2016	33.15	136.63	7	3.4
6	4	2016	33.14	136.56	6	2.8
6	4	2016	33.12	136.53	7	3.2
6	4	2016	33.07	136.59	6	3.3
6	4	2016	33.07	136.73	9	3.2
6	4	2016	33.12	136.56	6	3.3
6	4	2016	33.12	136.56	6	3
6	4	2016	33.09	136.71	7	3.3
6	4	2016	33.07	136.56	7	3.5
6	4	2016	33.08	136.51	6	3.1

Table C.2 continued from previous page

6	4	2016	33.08	136.64	7	3.1
6	4	2016	33.14	136.56	6	3.1
6	4	2016	33.09	136.51	6	3.4
6	4	2016	33.12	136.61	5	2.7
6	4	2016	33.18	136.64	6	3
6	4	2016	32.93	136.4	6	3.5
6	4	2016	32.93	136.4	6	3.3
6	4	2016	33.14	136.56	6	2.7
6	4	2016	33.11	136.56	7	2.9
5	4	2016	33.13	136.53	7	3.1
5	4	2016	33.12	136.56	6	3
5	4	2016	33.05	136.54	6	3.4
5	4	2016	33.12	136.53	5	3
5	4	2016	33.12	136.55	6	3
5	4	2016	33.21	136.74	6	3.7
4	4	2016	33.09	136.52	7	3.3
4	4	2016	33.06	136.56	10	3.6
4	4	2016	33.12	136.51	7	3.3
4	4	2016	33.07	136.55	7	3.5
4	4	2016	33.13	136.64	11	3.6
4	4	2016	33.11	136.53	6	3.1
4	4	2016	33.18	136.64	6	3.3
4	4	2016	33.2	136.64	6	3.2
4	4	2016	33.18	136.66	6	3.3
4	4	2016	33.11	136.56	6	3.5
4	4	2016	33.14	136.63	8	3.4
4	4	2016	33.12	136.55	7	3.3
4	4	2016	33.16	136.61	7	3.1
4	4	2016	33.15	136.67	5	3.3
3	4	2016	33.13	136.64	15	3.9
3	4	2016	33.31	136.73	6	4.1
3	4	2016	33.1	136.48	9	3.5
3	4	2016	33.2	136.65	7	3.5
3	4	2016	33.18	136.64	7	3.3
1	4	2016	33.34	136.97	7	2.6
1	4	2016	33.32	136.95	6	3.7

Table C.3: 2009 VLFEs as defined by Sugioka et al. (2012)

Date (dd.mm.yyyy)			Latitude (°)	Longitude (°)	Depth (kmbsl)	M_w
28	3	2009	33.24858	136.7011	8.4	4.4
28	3	2009	33.2495	136.8453	7.6	4.7
27	3	2009	33.28941	136.7968	8	4.3
26	3	2009	33.20142	136.8746	5.2	4.9
25	3	2009	33.20142	136.8746	11.6	4.7
25	3	2009	33.20928	136.8456	7.6	4.4
25	3	2009	33.20112	136.8265	7.6	4.7
25	3	2009	33.29727	136.7679	6	4.6
25	3	2009	33.24858	136.7011	7.2	3.8
25	3	2009	33.16876	136.7979	6.8	4
24	3	2009	33.20051	136.7304	6.4	4.3
24	3	2009	33.20051	136.7304	6.4	4.1

Table C.4: 2004 episode as defined by

Date			Latitude (°)	Longitude (°)	Depth (kmbsl)	M_w
7	5	2004	32.8	135.9	6.66	3.82
9	5	2004	32.9	135.7	8.44	3.65
9	5	2004	33	135.8	9.27	3.36
9	5	2004	32.8	136	6.31	3.76
9	5	2004	32.8	136	6.31	3.57
6	9	2004	33.1	136.9	5.2	4.19
6	9	2004	33.1	136.8	5.64	4.25
7	9	2004	33.2	136.8	6.66	3.97
7	9	2004	33.1	136.9	5.2	4.54
7	9	2004	33.4	136.7	9.03	4.4
8	9	2004	33.2	136.8	6.66	4.05
8	9	2004	33.2	136.7	7.19	3.67
8	9	2004	33.3	137	6.62	3.51
8	9	2004	33.4	137.1	7	3.9
8	9	2004	33.2	136.9	6.15	3.85
8	9	2004	33.2	136.9	6.15	3.9
8	9	2004	33.1	136.9	5.2	4.18
8	9	2004	33.1	136.9	5.2	3.95
8	9	2004	33.2	137	5.6	3.83
8	9	2004	33.1	137	4.93	4.15
8	9	2004	33.4	137.3	5.97	3.83

Table C.4 continued from previous page

8	9	2004	33.3	137.3	5.11	4.4
9	9	2004	33.1	137	4.93	3.96
9	9	2004	33.2	136.8	6.66	3.6
9	9	2004	33.2	136.9	6.7	4
9	9	2004	33.2	137.1	5.16	4.22
9	9	2004	33.2	136.9	6.15	3.72
9	9	2004	33.2	136.9	6.15	3.8
9	9	2004	33.1	136.9	5.2	4.02
9	9	2004	33.1	136.9	5.2	4.15
9	9	2004	33.2	136.8	6.2	3.99
9	9	2004	33.2	137	5.6	3.76
9	9	2004	33.4	136.9	7.97	3.41
9	9	2004	33.4	136.9	7.97	3.41
9	9	2004	33.3	137	6.6	3.71
9	9	2004	33.1	136.9	5.2	3.96
9	9	2004	33.4	137.2	6.51	3.75
9	9	2004	33.4	137.2	6.51	3.65
9	9	2004	33.4	137.2	6.51	3.73
9	9	2004	33.3	137	6.62	3.61
9	9	2004	33.2	136.8	6.66	3.54
9	9	2004	33.2	136.9	6.15	3.73
9	9	2004	33.1	136.9	5.2	3.71
9	9	2004	33.2	137.1	5.16	4.09
9	9	2004	33.3	137	6.62	3.52
9	9	2004	33.1	136.9	5.2	4.25
9	9	2004	33.1	136.8	5.64	3.98
10	9	2004	33.3	137.2	5.55	3.91
10	9	2004	33.3	137.1	6.07	3.66
10	9	2004	33.4	137.2	6.51	3.76
10	9	2004	33.3	137.1	6.07	3.72
10	9	2004	33.4	137.2	6.51	3.67
10	9	2004	33.3	137.2	5.55	3.78
10	9	2004	33.3	137	6.62	3.67
10	9	2004	33.3	137	6.62	3.86
10	9	2004	33.2	136.9	6.15	3.83
10	9	2004	33.2	136.9	6.15	3.52
10	9	2004	33.1	136.9	5.2	3.69
10	9	2004	33.2	137.1	5.16	3.86
10	9	2004	33.2	137.1	5.16	3.99
10	9	2004	33.3	137	6.62	3.27

Table C.4 continued from previous page

10	9	2004	33.4	137.1	7	3.7
10	9	2004	33.4	137.1	7	3.73
10	9	2004	33.4	137.1	7	3.53
10	9	2004	33.2	136.9	6.15	3.77
10	9	2004	33.1	136.9	5.2	4.3
10	9	2004	33.1	136.9	4.9	4.19
10	9	2004	33.2	136.8	4.9	3.8
10	9	2004	33.2	137	5.6	3.67
10	9	2004	33.1	136.9	5.2	3.96
10	9	2004	33.2	136.9	6.2	4.13
10	9	2004	33.1	137	4.93	4.04
11	9	2004	33.4	137.3	5.97	3.87
11	9	2004	33.4	137.1	7	3.51
11	9	2004	33.3	137.3	5.11	4.17
11	9	2004	33.3	137.2	5.6	4.18
11	9	2004	33.1	137.1	4.88	3.71
11	9	2004	33.3	137.1	6.07	3.54
11	9	2004	33.1	137	4.93	4.21
11	9	2004	33.1	136.9	5.2	3.72
11	9	2004	33.2	136.9	6.15	3.65
11	9	2004	33.3	136.8	7.61	3.43
11	9	2004	33.2	137	5.6	3.52
11	9	2004	33.2	137.1	5.16	4.45
11	9	2004	33.4	137.1	7	3.64
11	9	2004	33.4	137.1	7	3.57
11	9	2004	33.1	137	4.93	4.19
11	9	2004	33.2	137.1	5.16	4.08
11	9	2004	33.2	136.9	6.15	3.8
11	9	2004	33.1	137	4.93	4.01
11	9	2004	33.3	137	6.62	3.56
11	9	2004	33.3	137	6.62	3.81
11	9	2004	33.2	137.2	4.92	4.12
11	9	2004	33.4	137.1	7	3.52
11	9	2004	33.4	137.2	6.5	3.8
11	9	2004	33.4	137.1	7	3.67
11	9	2004	33.1	137	4.93	4.41
11	9	2004	33.4	137.1	7	3.75
11	9	2004	33.3	137.2	5.55	4.07
11	9	2004	33.1	136.9	5.2	4.13
11	9	2004	33.2	136.8	6.6	3.99

Table C.4 continued from previous page

11	9	2004	33.2	136.9	6.15	4.01
11	9	2004	33.1	136.8	5.64	4.14
11	9	2004	33.3	136.8	7.61	3.45
11	9	2004	33.2	136.8	6.66	3.82
11	9	2004	33.4	137.2	6.51	3.61
11	9	2004	33.4	137.2	6.51	3.71
11	9	2004	33.2	137	5.6	3.71
11	9	2004	33.1	136.7	6.21	3.54
11	9	2004	33.3	136.7	8.13	3.54
11	9	2004	33.2	136.9	6.15	3.73
11	9	2004	33.1	136.9	5.2	4.28
12	9	2004	33.2	137	5.6	4.11
12	9	2004	33.4	137.2	6.51	3.63
12	9	2004	33.2	137.1	5.16	4.01
12	9	2004	32.7	135.1	7.03	4.56
12	9	2004	32.6	135.1	6.05	4.21
12	9	2004	32.6	135.1	6.05	4.14
12	9	2004	32.7	135.2	6.86	3.78
12	9	2004	33.2	137	5.6	4.03
12	9	2004	33.1	137	4.93	4.39
12	9	2004	33.2	136.9	6.15	3.55
12	9	2004	33.2	137	5.6	3.96
12	9	2004	33.6	137.4	7.44	3.51
12	9	2004	33.1	136.9	5.2	4.02
12	9	2004	33.1	136.9	5.2	3.88
12	9	2004	32.7	135.1	7.03	3.83
13	9	2004	33.3	137.3	5.11	4.27
13	9	2004	33.2	136.7	7.2	3.79
13	9	2004	33.2	136.7	7.19	3.94
13	9	2004	33.3	137	6.62	3.5
13	9	2004	33.4	137.1	7	3.61
13	9	2004	33.6	137.2	8.37	3.5
13	9	2004	33.3	137.2	5.55	3.62
13	9	2004	33.3	137.1	6.07	3.5
13	9	2004	33.1	136.9	5.2	3.69
13	9	2004	33.1	136.9	5.2	4.03
13	9	2004	33.4	137.3	5.97	3.63
13	9	2004	33	136.6	5.67	4.35
13	9	2004	33.3	137	6.62	3.69
13	9	2004	33.2	136.9	6.15	4

Table C.4 continued from previous page

13	9	2004	33.2	136.7	7.19	3.81
13	9	2004	33.1	137	4.93	4.19
13	9	2004	33.1	137	4.93	4.05
13	9	2004	33.3	137	6.62	3.42
13	9	2004	33.2	137	5.6	3.69
13	9	2004	33.2	137.1	5.16	4
13	9	2004	33.4	137	7.49	3.52
13	9	2004	33.1	136.9	5.2	4.03
13	9	2004	33.3	137.2	5.55	3.93
13	9	2004	33.4	137.2	6.51	3.52
13	9	2004	33.3	137.3	5.11	3.84
13	9	2004	33.1	136.9	5.2	4.04
13	9	2004	33.2	137.2	4.92	3.86
13	9	2004	33.2	137.1	5.16	3.96
13	9	2004	33.4	136.9	7.97	3.33
14	9	2004	33.3	137	6.62	3.56
14	9	2004	33.2	137	5.6	3.85
14	9	2004	33.1	137	4.93	4.23
14	9	2004	33.1	136.9	5.2	4.27
14	9	2004	33.2	137	5.6	3.75
14	9	2004	33.4	137.1	7	3.49
14	9	2004	33.3	137.2	5.55	3.81
14	9	2004	33.1	137	4.93	4.06
14	9	2004	33	136.9	4.88	3.39
14	9	2004	33.2	136.9	6.15	3.7
15	9	2004	33.4	137.1	7	3.48
15	9	2004	33.3	136.9	7.12	3.34
15	9	2004	33.3	137	6.62	3.61
15	9	2004	33.4	137	7.49	3.62
15	9	2004	33.4	137.1	7	3.52
15	9	2004	33.1	137	4.93	4.2
15	9	2004	33.1	136.9	5.2	3.76
15	9	2004	33.4	137.1	7	3.49
15	9	2004	33.4	137.2	6.51	3.82
15	9	2004	33.3	137.3	5.11	4.3
15	9	2004	33.1	136.9	5.2	4.03
15	9	2004	33.4	137.2	6.51	3.53
15	9	2004	33.2	136.8	6.66	3.72
15	9	2004	33.2	136.8	6.66	3.74
15	9	2004	33.3	137	6.62	3.73

Table C.4 continued from previous page

15	9	2004	33.2	137.1	5.16	4.26
15	9	2004	33.2	137.1	5.16	3.9
15	9	2004	33.3	137	6.62	3.5
16	9	2004	33.1	136.9	5.2	3.86
16	9	2004	33.3	137.1	6.07	3.4
16	9	2004	33.2	137	5.6	3.74
16	9	2004	33.2	137.1	5.16	4.03
16	9	2004	33.1	137	4.93	4.04
16	9	2004	33.2	137	5.6	3.91
16	9	2004	33.2	137.1	5.16	4.06
16	9	2004	33.4	137.1	7	3.67
16	9	2004	33.3	137.2	5.55	3.95
16	9	2004	33.2	136.9	6.15	3.67
16	9	2004	33.1	136.9	5.2	3.79
16	9	2004	33.2	137.1	5.16	3.85
16	9	2004	33.1	136.9	5.2	4.12
16	9	2004	33.1	136.9	5.2	3.92
16	9	2004	33.3	136.7	8.13	3.61
16	9	2004	33.2	136.9	6.15	3.84
16	9	2004	33.2	136.9	6.15	3.79
16	9	2004	33.2	136.9	6.15	3.65
16	9	2004	33.1	136.9	5.2	4.16
16	9	2004	33.2	136.9	6.15	3.75
16	9	2004	33.2	137	5.6	3.7
16	9	2004	33.3	137.1	6.07	3.65
16	9	2004	33.3	137.1	6.07	3.54
16	9	2004	33.3	137.1	6.07	3.77
16	9	2004	33.2	137.3	4.88	3.92
17	9	2004	33.4	137.1	7	3.64
17	9	2004	33.2	136.8	6.7	4.06
17	9	2004	33.4	137.2	6.51	3.43
17	9	2004	33.3	137.1	6.07	3.97
17	9	2004	33.4	137.1	7	3.43
17	9	2004	33.1	137	4.93	4.09
18	9	2004	33.1	136.9	5.2	3.75
18	9	2004	33.2	136.9	6.15	3.58
18	9	2004	33.3	137.1	6.07	3.54
18	9	2004	33.3	137.3	5.11	4.28
18	9	2004	33.4	137.2	6.5	3.79
18	9	2004	33.3	137.2	5.55	3.91

Table C.4 continued from previous page

18	9	2004	33.3	137.3	5.11	4.3
18	9	2004	33.4	137.2	6.51	3.45
18	9	2004	33.4	137.3	5.97	3.75
18	9	2004	33.4	137.2	6.51	3.57
19	9	2004	33.3	137	6.62	3.54
19	9	2004	33.3	137	6.62	3.49
19	9	2004	33.2	137	5.6	3.92
20	9	2004	33.2	136.9	6.15	3.91
20	9	2004	33.2	136.9	6.15	3.92
20	9	2004	33.2	136.9	6.15	3.88
20	9	2004	33.2	136.8	6.66	3.72
20	9	2004	33.1	136.9	5.2	3.96
20	9	2004	33.3	137	6.62	3.34
20	9	2004	33.2	136.9	6.15	3.59
20	9	2004	33.2	136.8	6.66	3.77
20	9	2004	32.7	135.2	6.86	4.01
20	9	2004	32.7	135.1	7.03	3.96
20	9	2004	33.3	136.9	7.12	3.42
20	9	2004	33.2	137.1	5.16	3.95
20	9	2004	33.1	136.8	5.64	3.95
20	9	2004	33.1	136.9	5.2	4.13
20	9	2004	32.7	135.1	7.03	4.04
20	9	2004	33.1	136.9	5.2	4.07
20	9	2004	33.3	137	6.62	3.53
20	9	2004	33.3	137.2	5.55	3.67
20	9	2004	33.2	137	5.6	4.09
20	9	2004	33.2	137	5.6	3.72
20	9	2004	33.2	137	5.6	3.71
20	9	2004	33.2	136.9	6.15	3.79
20	9	2004	33.2	136.8	6.7	4.19
20	9	2004	33.1	136.9	5.2	4.36
20	9	2004	33.2	136.9	6.15	4
20	9	2004	33.1	136.9	5.2	4.35
20	9	2004	33.1	136.9	5.2	4.21
20	9	2004	33.1	136.7	6.21	3.76
20	9	2004	33.1	136.7	6.21	3.5
20	9	2004	33	136.8	4.93	3.34
20	9	2004	33.1	136.7	6.21	3.77
21	9	2004	33.1	136.7	6.21	3.87
21	9	2004	33.1	136.8	5.64	4.11

Table C.4 continued from previous page

21	9	2004	33.1	136.8	5.64	4.2
21	9	2004	33.1	136.8	5.64	4.27
21	9	2004	33.2	137.1	5.16	3.96
21	9	2004	33.2	137.1	5.16	4.22
21	9	2004	33.2	136.8	6.66	4.14
21	9	2004	33.3	136.7	8.13	3.87
21	9	2004	33.1	136.9	5.2	4.3
21	9	2004	33.2	136.9	6.15	3.76
21	9	2004	33.2	136.7	7.19	3.45
21	9	2004	33.3	137.2	5.55	3.89
21	9	2004	33.3	137.2	5.55	3.87
21	9	2004	33.3	137.2	5.55	3.44
21	9	2004	33	136.5	6.21	3.77
21	9	2004	33.3	137.3	5.11	3.95
21	9	2004	33.4	137.3	5.97	3.77
21	9	2004	33.4	137.2	6.51	3.66
21	9	2004	33.5	137.2	7.46	3.37
21	9	2004	33.5	137.2	7.46	3.4
21	9	2004	33.4	137.4	5.42	4.06
21	9	2004	33.3	137.2	5.55	4.11
21	9	2004	33.4	137.2	6.51	3.76
22	9	2004	33.1	136.9	5.2	3.94
22	9	2004	32.7	135.2	6.86	3.77
22	9	2004	32.6	135.2	5.87	3.6
23	9	2004	33.1	137.1	4.88	3.47
23	9	2004	33.3	137.2	5.55	3.72
23	9	2004	33.3	137.1	6.07	3.97
23	9	2004	33.2	137.1	5.16	4.05
23	9	2004	33.4	137	7.49	3.41
23	9	2004	33.2	137.1	5.16	4.02
23	9	2004	33.4	137	7.49	3.4
23	9	2004	33.2	137.1	5.16	3.95
23	9	2004	33.3	137	6.62	3.4
23	9	2004	33.2	136.9	6.15	3.74
23	9	2004	33.2	136.9	6.15	3.79
24	9	2004	33.3	137.1	6.07	3.55
24	9	2004	33.3	137.2	5.55	3.98
24	9	2004	33.2	137.2	4.92	3.83
24	9	2004	33.4	137.1	7	3.5
24	9	2004	33.3	137.3	5.11	4.2

Table C.4 continued from previous page

24	9	2004	33.2	137.2	4.92	4.07
24	9	2004	33.2	137	5.6	3.71
24	9	2004	33.3	137.2	5.55	3.85
24	9	2004	33.4	137.1	7	3.51
24	9	2004	33.5	137.4	6.48	3.69
24	9	2004	33.4	137.3	5.97	3.83
24	9	2004	33.3	137.2	5.55	4.29
24	9	2004	33.1	136.9	5.2	3.95
26	9	2004	33.2	136.9	6.15	3.67
26	9	2004	33.2	136.9	6.15	3.75
26	9	2004	33.2	137	5.6	3.92
26	9	2004	33.1	136.9	5.2	3.81
26	9	2004	32.8	135	8.06	3.56
26	9	2004	33.2	136.9	6.2	3.82
26	9	2004	33.2	136.9	6.15	4.03
26	9	2004	33.2	136.9	6.15	3.92
26	9	2004	33.3	137	6.62	3.49
26	9	2004	33.2	136.9	6.15	3.63
26	9	2004	33.2	136.9	6.15	3.99
26	9	2004	33.2	136.8	6.7	4.01
27	9	2004	33.3	137.1	6.07	3.72
27	9	2004	33.2	137.1	5.16	3.92
27	9	2004	33.2	137.1	5.16	3.99
27	9	2004	33.2	137.2	4.92	3.98
27	9	2004	33.3	137	6.62	3.46
27	9	2004	33.3	137.1	6.07	3.68
27	9	2004	33.3	137	6.62	3.63
27	9	2004	33.2	137	5.6	3.77
27	9	2004	33.3	137.2	5.55	3.83
27	9	2004	33.4	137.2	6.51	3.63
27	9	2004	33.4	137.1	7	3.46
27	9	2004	33.3	137.2	5.55	3.81
27	9	2004	33.4	137.2	6.51	3.62
28	9	2004	33.4	137.2	6.51	3.73
28	9	2004	33.4	137.4	5.42	4.03
28	9	2004	33.4	137.2	6.5	3.75
28	9	2004	33.4	137.3	5.97	3.92
28	9	2004	33.5	137.1	7.89	3.33
28	9	2004	33.4	137.3	5.97	3.68
28	9	2004	33.4	137.2	6.51	3.62

Table C.4 continued from previous page

30	9	2004	33.1	137	4.93	4.22
30	9	2004	33.4	137.2	6.51	3.67
30	9	2004	33.4	137.1	7	4.06
30	9	2004	33.4	137.1	7	3.68
30	9	2004	33.2	137	5.6	4.1
30	9	2004	33.1	137.1	4.88	3.97
30	9	2004	32.6	135.1	6.05	4.25
30	9	2004	33.2	137	5.6	4.02
1	10	2004	33.3	136.9	7.12	3.65
1	10	2004	33.3	136.9	7.12	3.7
1	10	2004	33.2	136.9	6.15	4
1	10	2004	33.2	136.9	6.15	3.88
1	10	2004	33.1	136.9	5.2	4.05
1	10	2004	33.2	136.9	6.15	3.98
1	10	2004	33.1	136.9	5.2	4.08
1	10	2004	33.1	136.9	5.2	4.07
1	10	2004	33.2	136.8	6.66	3.87
1	10	2004	33.1	136.9	5.2	4.32
1	10	2004	33.1	136.9	5.2	4.29
1	10	2004	33.1	136.9	5.2	4.18
1	10	2004	33.2	137.1	5.16	4
1	10	2004	33.3	137	6.62	3.62
1	10	2004	33.2	137.1	5.16	3.96
2	10	2004	33.1	137	4.93	3.93
3	10	2004	33.1	136.9	5.2	3.92
3	10	2004	33.1	136.8	5.64	3.76
3	10	2004	33.1	136.9	5.2	4.07
6	10	2004	33.3	137.2	5.55	3.76
6	10	2004	33.3	137.1	6.07	3.82
6	10	2004	33.3	137.1	6.07	3.7
6	10	2004	33.3	137.1	6.07	3.79
6	10	2004	33.3	137	6.62	3.47
6	10	2004	33.3	137	6.62	3.57
6	10	2004	33.4	137.1	7	3.83
6	10	2004	33.3	137.2	5.55	3.93
7	10	2004	33.3	137.2	5.55	4.29
7	10	2004	33.3	137.2	5.55	3.76
7	10	2004	33.4	137.2	6.51	3.48
8	10	2004	33.3	137	6.62	3.5
8	10	2004	33.2	137.1	5.16	4.13

Table C.4 continued from previous page

8	10	2004	33.4	137	7.49	3.53
8	10	2004	33.4	137.1	7	3.37
10	10	2004	33.1	137	4.93	4.21
10	10	2004	33.2	137	5.6	3.66
10	10	2004	33.2	137	5.6	3.99
10	10	2004	33.3	136.9	7.12	3.73
10	10	2004	33.2	137	5.6	3.82
10	10	2004	33.2	137	5.6	4.01
11	10	2004	33.2	136.9	6.15	3.89
11	10	2004	33.2	136.9	6.15	3.96
11	10	2004	33.2	136.9	6.15	3.92
11	10	2004	33.2	136.9	6.15	3.8
11	10	2004	33.2	136.9	6.15	3.98
11	10	2004	33.2	137	5.6	3.91
11	10	2004	33.1	137.1	4.88	3.52
11	10	2004	33.3	136.8	7.61	3.76
11	10	2004	33.2	136.8	6.66	3.49
11	10	2004	33.2	136.8	6.66	3.67
11	10	2004	33.2	136.8	6.66	3.51
11	10	2004	33.1	136.9	5.2	3.96
11	10	2004	33.1	137	4.93	4.19
11	10	2004	33.2	136.9	6.15	3.8
11	10	2004	33.1	136.9	5.2	4.54
11	10	2004	33.2	136.9	6.15	3.63
11	10	2004	33.2	136.8	6.66	3.83
11	10	2004	33.1	136.8	5.64	4.17
11	10	2004	33.1	136.8	5.64	4.39
11	10	2004	33.1	137	4.93	4.13
11	10	2004	33.1	136.8	5.64	4
11	10	2004	33.1	137.1	4.88	3.59
11	10	2004	33.1	136.8	5.64	4.22
11	10	2004	33.3	137	6.62	3.76
11	10	2004	33	136.9	4.88	3.95
11	10	2004	33.2	136.8	6.66	3.89
11	10	2004	33.1	136.9	5.2	4
12	10	2004	33.1	136.7	6.21	3.85
12	10	2004	33.1	136.7	6.21	3.87
12	10	2004	33.1	136.7	6.21	3.84
12	10	2004	33.1	136.7	6.21	3.84
13	10	2004	33.1	136.7	6.21	3.83

Table C.4 continued from previous page

13	10	2004	33.1	136.7	6.21	3.67
14	10	2004	33.4	137.1	7	3.47
14	10	2004	33.4	137.1	7	3.54
14	10	2004	33.4	137.1	7	3.71
15	10	2004	33.1	136.9	5.2	3.89
15	10	2004	33.2	136.8	6.66	3.56
15	10	2004	33.2	136.9	6.15	3.87
15	10	2004	33.1	136.9	5.2	4.1
15	10	2004	33.2	136.9	6.15	3.67
15	10	2004	33.1	136.9	5.2	4.73
15	10	2004	33.2	137.1	5.16	4.06
16	10	2004	33.2	137.1	5.16	4.13
16	10	2004	33.3	137	6.62	3.66
16	10	2004	33.2	137.1	5.16	3.92
16	10	2004	33.2	136.8	6.66	3.88
16	10	2004	33.2	136.9	6.15	4.02
16	10	2004	33.4	137.1	7	3.58
24	10	2004	33.2	137	5.6	3.84
24	10	2004	33.2	137.1	5.16	3.91
24	10	2004	33.3	137	6.62	3.45
24	10	2004	33.4	137.1	7	3.65
24	10	2004	33.4	137.2	6.51	3.61
24	10	2004	33.4	137.1	7	3.47
24	10	2004	33.3	137.1	6.07	3.67
24	10	2004	33.4	137.1	7	3.8
24	10	2004	33.2	137.2	4.92	4.32
24	10	2004	33.4	137.1	7	3.85
24	10	2004	33.4	137.2	6.51	4
24	10	2004	33.4	137.3	5.97	3.85
25	10	2004	33.4	137.2	6.51	3.62
29	10	2004	33.3	137	6.62	3.44
29	10	2004	33.4	137	7.49	3.45
29	10	2004	33.3	137	6.62	3.45
29	10	2004	33.2	137	5.6	3.88
29	10	2004	33.1	136.9	5.2	3.96
29	10	2004	33.2	136.9	6.15	3.76
29	10	2004	33.2	137	5.6	3.83
29	10	2004	33.1	136.9	5.2	4.02
29	10	2004	33.1	136.9	5.2	3.86
29	10	2004	33.1	136.9	5.2	4.01

Table C.4 continued from previous page

29	10	2004	33.2	136.9	6.15	3.7
29	10	2004	33.1	136.8	5.64	3.9
29	10	2004	33.2	136.9	6.15	3.65
29	10	2004	33.2	136.9	6.15	3.67
29	10	2004	33.1	137	4.93	3.96
29	10	2004	33.2	136.9	6.15	3.71
29	10	2004	33.2	136.9	6.15	3.79
29	10	2004	33.3	136.9	7.12	3.54
29	10	2004	33.1	136.9	5.2	4.02
29	10	2004	33.2	136.9	6.15	3.58
29	10	2004	33.3	137.1	6.07	3.55
29	10	2004	33.2	136.9	6.15	3.7
29	10	2004	33.1	136.9	5.2	4.11
29	10	2004	33.4	136.9	7.97	3.43
29	10	2004	33.3	136.9	7.12	3.5
29	10	2004	33.2	136.8	6.66	3.89
29	10	2004	33.1	137	4.93	4.13
29	10	2004	33.1	137	4.93	4.16
30	10	2004	33.1	136.9	5.2	3.98
30	10	2004	33.2	137.1	5.16	3.99
30	10	2004	33.4	137.1	7	3.46
30	10	2004	33.4	137.1	7	3.49
30	10	2004	33.4	137.1	7	3.53
13	11	2004	33.2	137.1	5.16	4.08
13	11	2004	33.2	136.8	6.66	3.79
13	11	2004	33.1	137	4.93	4.17
13	11	2004	33.2	136.9	6.15	3.58
14	11	2004	33.3	137.2	5.55	3.67
14	11	2004	33.3	137.1	6.07	3.54
14	11	2004	33.1	136.8	5.64	3.91
14	11	2004	33.1	136.9	5.2	4.34
14	11	2004	33.2	136.9	6.15	3.85
14	11	2004	33.3	136.9	7.12	3.43
14	11	2004	33.1	136.9	5.2	3.82
14	11	2004	33.1	136.8	5.64	3.9
14	11	2004	33.2	136.8	6.66	4.12
14	11	2004	33.3	136.7	8.13	3.64
14	11	2004	33.3	136.8	7.61	3.47
14	11	2004	33.1	137.1	4.88	3.6
14	11	2004	33.2	137.1	5.16	3.94

Table C.4 continued from previous page

14	11	2004	33.1	136.8	5.64	3.94
14	11	2004	33.2	136.8	6.66	3.53
13	12	2004	33.2	137	5.6	4.01
13	12	2004	33.3	137.2	5.55	3.71
13	12	2004	33.3	137.2	5.55	3.95
13	12	2004	33.4	137.1	7	3.74
13	12	2004	33.4	137.1	7	3.55
13	12	2004	33.3	137.2	5.55	4.08
13	12	2004	33.3	137.2	5.55	3.99
13	12	2004	33.1	137.1	4.88	4.11
13	12	2004	33.4	137.2	6.51	3.43
13	12	2004	33.2	137.2	4.92	4.02
13	12	2004	33.3	137.3	5.11	4.05
13	12	2004	33.4	137.2	6.51	3.69
13	12	2004	33.4	137	7.49	3.55
13	12	2004	33.4	137.2	6.51	3.5
13	12	2004	33.5	137.2	7.46	3.49
13	12	2004	33.4	137.2	6.51	3.71
13	12	2004	33.4	137.2	6.51	3.79
13	12	2004	33.4	137.2	6.51	3.88
13	12	2004	33.4	137.2	6.51	3.66
13	12	2004	33.3	137.1	6.07	3.64
14	12	2004	33.2	137	5.6	3.7
14	12	2004	33.4	137.3	5.97	3.8
14	12	2004	33.2	137.2	4.92	4.09
14	12	2004	33.2	137.1	5.16	3.95
14	12	2004	33.4	137.1	7	3.55
14	12	2004	33.3	137.1	6.07	3.65
14	12	2004	33.4	137.1	7	3.41
14	12	2004	33.3	137.2	5.55	4.04
14	12	2004	33.3	137.2	5.55	3.93
14	12	2004	33.4	137.2	6.51	3.79
14	12	2004	33.4	137.2	6.51	3.8
14	12	2004	33.4	137	7.49	3.37
15	12	2004	33.4	137.2	6.51	3.63
15	12	2004	33.5	137.2	7.46	3.44
15	12	2004	33.5	137.1	7.89	3.51
27	12	2004	33.2	136.8	6.66	3.96

Table C.5: 2009 episode as defined by Takemura, Matsuzawa, Noda, et al. (2019)

Date (dd.mm.yyyy)			Latitude (°)	Longitude (°)	Depth (kmbsl)	M_w
24	3	2009	32.5	134.5	7.92	3.69
24	3	2009	33.2	136.8	6.6	3.85
24	3	2009	33.2	136.8	6.6	3.78
24	3	2009	33.2	136.8	6.66	3.76
24	3	2009	33.1	136.9	5.2	3.8
25	3	2009	33.3	136.7	8.13	3.63
25	3	2009	33.1	136.9	5.2	4.06
25	3	2009	33.2	136.7	7.19	3.35
25	3	2009	33.2	136.7	7.19	3.5
25	3	2009	33.1	136.8	5.64	4.04
25	3	2009	33.2	136.8	6.66	3.6
25	3	2009	33.1	136.9	5.2	4.09
25	3	2009	33.1	137	4.93	4.18
25	3	2009	33.2	136.8	6.66	3.79
25	3	2009	33.2	136.9	6.15	3.99
25	3	2009	33.2	136.9	6.15	4.05
25	3	2009	33.2	136.9	6.2	3.79
25	3	2009	33.1	136.9	5.2	4.44
25	3	2009	33.3	136.8	7.61	3.64
25	3	2009	33.2	136.9	6.15	3.98
25	3	2009	33.2	136.9	6.15	3.68
25	3	2009	33.2	136.9	6.15	3.79
25	3	2009	33.2	136.8	6.66	3.74
25	3	2009	33.2	136.9	6.15	3.72
25	3	2009	33.2	136.9	6.2	3.92
25	3	2009	33.1	136.9	5.2	3.88
26	3	2009	33.2	136.9	6.15	3.79
26	3	2009	33.2	136.8	6.66	3.87
26	3	2009	33.3	136.8	7.61	3.66
26	3	2009	33.2	136.8	6.66	3.94
26	3	2009	33.1	136.9	5.2	4.11
26	3	2009	33.2	137	5.6	4.14
26	3	2009	33.2	137	5.6	4
26	3	2009	33.2	136.9	6.15	3.61
26	3	2009	33.2	137	5.6	3.86
26	3	2009	33.2	137.1	5.16	3.89
26	3	2009	33.1	136.9	5.2	4.29
26	3	2009	33.1	136.8	5.64	3.79
26	3	2009	33.2	137.1	5.16	4.2

Table C.5 continued from previous page

26	3	2009	33.2	136.9	6.15	3.67
26	3	2009	33.2	136.9	6.15	3.74
26	3	2009	33.2	136.9	6.15	4.18
26	3	2009	33.3	136.8	7.61	3.45
27	3	2009	33.2	137	5.6	3.89
27	3	2009	33.1	137	4.93	4.07
27	3	2009	33.3	136.7	8.13	3.49
27	3	2009	33.2	136.9	6.15	3.61
27	3	2009	33.1	137	4.93	4.14
27	3	2009	33.2	136.8	6.66	3.5
27	3	2009	33.1	136.9	5.2	4.32
27	3	2009	33.2	137	5.6	3.91
27	3	2009	33.2	137	5.6	4.01
27	3	2009	33.2	137	5.6	3.77
27	3	2009	33.3	137	6.62	3.55
27	3	2009	33.3	137.1	6.07	3.84
27	3	2009	33.3	136.7	8.13	3.58
28	3	2009	33.1	137	4.93	4.11
28	3	2009	33.1	136.9	5.2	3.83
28	3	2009	33.3	137	6.62	3.57
28	3	2009	33.2	137.3	4.88	3.51
28	3	2009	33.3	137.1	6.07	3.51
28	3	2009	33.2	136.9	6.15	3.74
28	3	2009	33.2	137	5.6	3.81
28	3	2009	33.2	137	5.6	3.9
28	3	2009	33.2	136.9	6.15	3.73
28	3	2009	33.1	137	4.93	4.37
29	3	2009	33.1	136.9	5.2	3.95
29	3	2009	33.3	137	6.62	3.73
29	3	2009	33.2	137	5.6	3.67
29	3	2009	33.2	136.8	6.66	3.59
29	3	2009	33.1	136.9	5.2	4.2
29	3	2009	33.2	136.9	6.2	4.07
29	3	2009	33.2	136.9	6.15	4.02
29	3	2009	33.3	137.2	5.55	3.92
29	3	2009	33.3	137.2	5.55	3.82
29	3	2009	33.3	137.2	5.55	3.86
29	3	2009	33.3	137.2	5.55	3.94
29	3	2009	33.4	137.2	6.51	3.53
29	3	2009	33.3	137.1	6.07	3.73

Table C.5 continued from previous page

29	3	2009	33.3	137	6.62	3.52
29	3	2009	33.4	137.2	6.51	3.71
29	3	2009	33.3	137.2	5.55	4.04
29	3	2009	33.4	136.9	7.97	3.42
29	3	2009	33.4	137.1	7	3.5
29	3	2009	33.3	137.2	5.55	4.13
29	3	2009	33.3	137.3	5.11	4.15
29	3	2009	33.5	137.2	7.46	3.49
29	3	2009	33.3	137.2	5.55	3.88
29	3	2009	33.4	137.2	6.51	3.78
29	3	2009	33.4	137.2	6.51	3.69
29	3	2009	33.4	137.1	7	3.49
29	3	2009	33.4	137.3	5.97	3.71
29	3	2009	33.5	137.2	7.46	3.49
29	3	2009	33.5	137.2	7.46	3.41
29	3	2009	33.3	137.1	6.07	3.7
29	3	2009	33.3	137	6.62	3.72
29	3	2009	33.3	137.3	5.11	4.15
30	3	2009	33.4	137.2	6.51	3.74
30	3	2009	33.4	137.3	5.97	3.68
30	3	2009	33.4	137.1	7	3.45
30	3	2009	33	136.6	5.67	3.84
30	3	2009	33.5	137.2	7.46	3.62
30	3	2009	33.4	137.2	6.51	3.73
30	3	2009	33.4	137.2	6.51	3.55
30	3	2009	33.4	137.2	6.51	3.75
30	3	2009	33.3	137.3	5.11	4.52
30	3	2009	33.3	137.2	5.55	3.94
30	3	2009	33.2	137.2	4.92	3.83
31	3	2009	33	136.6	5.67	3.84
31	3	2009	33.2	137.1	5.16	4.09
1	4	2009	33.2	137	5.6	3.85
3	4	2009	33.4	137.2	6.51	3.6
3	4	2009	33.4	137.1	7	3.72
3	4	2009	33.3	137.2	5.55	3.99
3	4	2009	33.4	137.1	7	3.7
3	4	2009	33.3	137.2	5.55	3.98
3	4	2009	33.4	137.3	5.97	3.9
3	4	2009	33.5	137.3	6.95	3.66
3	4	2009	33.4	137.3	5.97	3.96

Table C.5 continued from previous page

3	4	2009	33.4	137.4	5.42	4.01
3	4	2009	33.5	137.2	7.46	3.57
7	4	2009	32.6	134.6	7.88	3.87
7	4	2009	32.5	134.7	6.77	4.21
7	4	2009	32.7	134.7	8.02	3.79
8	4	2009	32.7	134.7	8.02	3.47
8	4	2009	32.7	134.7	8.02	3.6
8	4	2009	32.7	134.7	8.02	3.58
9	4	2009	33.2	136.8	6.66	3.49
9	4	2009	33.1	137	4.93	3.94
9	4	2009	33.3	136.8	7.61	3.19
9	4	2009	33.1	137	4.93	4.29
9	4	2009	33.2	136.9	6.15	3.63
9	4	2009	33.2	136.9	6.15	3.76
9	4	2009	33.2	136.9	6.15	3.82
9	4	2009	33.2	136.8	6.66	3.59
9	4	2009	33.2	137	5.6	3.73
9	4	2009	33.3	136.8	7.61	3.36
9	4	2009	33.4	136.8	8.49	3.84
9	4	2009	33.2	137	5.6	3.94
9	4	2009	33.2	136.8	6.66	3.67
9	4	2009	33.2	137	5.6	3.94
9	4	2009	33.2	136.9	6.15	3.77
9	4	2009	33.2	136.8	6.66	3.77
9	4	2009	33.1	136.9	5.2	3.8
9	4	2009	33.1	136.9	5.2	3.93
9	4	2009	32.7	134.7	8.02	3.54
9	4	2009	32.7	134.8	7.7	3.97
9	4	2009	32.5	134.7	6.77	3.84
9	4	2009	32.6	134.7	7.42	3.54
12	4	2009	32.6	134.8	6.95	3.74
12	4	2009	32.7	134.7	8.02	3.66
12	4	2009	32.6	134.8	6.95	4
12	4	2009	32.6	134.7	7.42	3.76
20	4	2009	32.8	134.8	8.34	3.42
20	4	2009	32.8	134.8	8.34	3.45
28	4	2009	32.6	134.7	7.42	3.58
28	4	2009	32.7	134.8	7.7	3.68
28	4	2009	32.7	134.7	8.02	3.64
28	4	2009	33.3	137.3	5.11	4.19

Table C.5 continued from previous page

28	4	2009	33.4	137.3	5.97	3.88
28	4	2009	33.4	137.3	5.97	3.8
1	5	2009	32.6	134.8	6.95	3.58
1	5	2009	32.6	134.8	6.95	3.67
3	5	2009	32.6	135	6.33	3.8
5	5	2009	32.6	134.6	7.88	3.34
7	5	2009	32.8	134.8	8.34	3.42
11	5	2009	32.7	134.7	8.02	3.76
11	5	2009	32.7	134.7	8.02	3.85
11	5	2009	32.7	134.7	8.02	3.65
12	5	2009	32.6	134.8	6.95	3.98
12	5	2009	32.6	134.7	7.42	3.66
22	5	2009	32.7	135.2	6.86	3.7
27	5	2009	32.7	135.2	6.86	3.55
1	6	2009	32.6	134.8	6.95	3.73
13	6	2009	32.7	135.3	6.74	3.73
13	6	2009	32.8	135.2	7.92	3.92
14	6	2009	32.8	135.2	7.92	3.98
17	6	2009	32.7	135.2	6.86	4.2
17	6	2009	32.7	135.2	6.86	4.05
17	6	2009	32.8	135.2	7.92	3.72
23	6	2009	32.7	135.3	6.74	4.15
23	6	2009	32.7	135.3	6.74	3.97
27	6	2009	32.7	135.3	6.74	3.95
27	6	2009	32.7	135.2	6.86	3.93
27	6	2009	32.7	135.2	6.86	4.03
2	7	2009	32.7	135.3	6.74	3.81
2	7	2009	32.7	135.4	6.62	3.85
2	7	2009	32.7	135.3	6.74	3.65
6	7	2009	32.8	135.2	7.92	3.67
6	7	2009	32.7	135.2	6.86	4.33
6	7	2009	32.8	135.3	7.85	3.47
8	7	2009	32.7	135.4	6.62	3.82
11	7	2009	32.7	135.3	6.74	3.89
11	7	2009	32.8	135.2	7.92	3.61
11	7	2009	32.7	135.3	6.74	3.81
11	7	2009	32.7	135.2	6.86	3.99
11	7	2009	32.9	134.9	8.9	3.57

C.2 DONET network coordinates

Table C.6: Coordinates of DONET nodes (Source: JAMSTEC (2012))

Node	Latitude ($D^{\circ}M.M'$)	Longitude ($D^{\circ}M.M'$)	Depth (mbsl)
A	33° 43.349'	136° 33.215'	2009
B	33° 25.150'	136° 51.683'	1859
C	33° 03.331'	136° 50.624'	3593
D	33° 13.998'	136° 37.350'	2080
E	33° 27.909'	136° 20.971'	1979

Table C.7: Coordinates for DONET observatories (Source: JAMSTEC (2012))

Node	Observatory		Latitude ($D°M.M'$)	Longitude ($D°M.M'$)	Depth (mbsl)
A	A-1	KMA01	33° 48.287'	136° 33.421'	2,039
	A-2	KMA02	33° 45.144'	136° 38.930'	2,011
	A-3	KMA03	33° 38.905'	136° 36.220'	2,063
	A-4	KMA04	33° 40.684'	136° 28.043'	2,054
B	B-5	KMB05	33° 28.633'	136° 55.586'	1,998
	B-6	KMB06	33° 21.506'	136° 55.295'	2,499
	B-7	KMB07	33° 21.680'	136° 48.433'	1,980
	B-8	KMB08	33° 27.985'	136° 48.231'	1,924
C	C-9	KMC09	33° 03.503'	136° 49.879'	3,511
	C-10	KMC10	33° 03.200'	136° 56.009'	4,247
	C-11	KMC11	33° 00.195'	136° 46.739'	4,378
	C-12	KMC12	33° 07.671'	136° 49.129'	3,784
D	D-13	KMD13	33° 13.203'	136° 41.420'	2,441
	D-14	KMD14	33° 10.360'	136° 34.617'	2,350
	D-15	KMD15	33° 13.986'	136° 33.783'	1,909
	D-16	KMD16	33° 18.270'	136° 35.748'	1,970
E	E-17	KME17	33° 29.098'	136° 26.703'	2,054
	E-18	KME18	33° 23.159'	136° 22.967'	2,052
	E-19	KME19	33° 26.754'	136° 15.386'	1,909
	E-20	KME20	33° 32.664'	136° 19.948'	1,977

C.3 Slip-deficit rates

Table C.8: Absolute slip-deficit rates for the Nankai trough estimated by Yokota et al. (2016). The angle is counter-clockwise from the east.

Latitude (°)	Longitude (°)	Slip angle (°)	Slip-deficit rate (m/yr)
31.041	132.511	-143.373	0.0077
31.169	132.743	-133.469	0.0077
31.296	132.976	-135.328	0.0083
31.422	133.21	-150.873	0.0121
31.549	133.445	-161.94	0.0189
31.675	133.68	-168.515	0.0233
31.8	133.916	-175.832	0.022
31.925	134.153	170.747	0.0162

Table C.8 continued from previous page

32.049	134.39	153.338	0.0117
32.173	134.628	145.007	0.0097
32.297	134.866	150.987	0.0089
32.42	135.106	165.316	0.0087
32.542	135.346	171.046	0.0099
32.664	135.586	162.653	0.0131
32.785	135.828	160.316	0.0153
32.906	136.07	160.591	0.0153
33.027	136.313	157.388	0.0154
33.146	136.557	160.04	0.0182
33.266	136.801	164.781	0.0191
33.384	137.046	170.011	0.0143
33.503	137.292	179.921	0.0178
33.62	137.539	-176.997	0.0265
33.737	137.786	-177.636	0.0278
33.854	138.035	176.539	0.0256
33.97	138.284	169.738	0.0225
34.085	138.533	168.921	0.017
34.2	138.784	164.725	0.0084
34.314	139.035	90.647	0.0014
34.427	139.288	-3.338	0.0033
31.24	132.362	-145.816	0.0255
31.368	132.595	-135.005	0.0245
31.496	132.829	-135.665	0.025
31.623	133.063	-151.855	0.036
31.749	133.298	-163.251	0.0567
31.876	133.533	-170.083	0.0705
32.001	133.769	-177.902	0.0674
32.126	134.006	168.09	0.051
32.251	134.244	151.463	0.0383
32.375	134.482	144.659	0.0324
32.499	134.721	150.978	0.0298
32.622	134.961	165.319	0.0281
32.745	135.201	171.167	0.0311
32.866	135.443	161.839	0.0408
32.988	135.685	159.047	0.0474
33.108	135.927	159.828	0.047
33.229	136.171	157.805	0.0461
33.349	136.415	160.505	0.0543
33.468	136.66	164.631	0.0571

Table C.8 continued from previous page

33.588	136.905	169.406	0.042
33.707	137.151	179.176	0.0518
33.825	137.398	-177.917	0.0774
33.942	137.646	-178.735	0.0816
34.059	137.894	175.611	0.0757
34.175	138.144	169.234	0.067
34.291	138.394	168.515	0.0508
34.406	138.645	164.35	0.0255
34.52	138.897	96.337	0.004
34.634	139.149	-8.721	0.0094
31.439	132.214	-153.706	0.04
31.567	132.447	-141.557	0.0327
31.695	132.681	-138.542	0.0266
31.822	132.915	-158.056	0.036
31.949	133.15	-170.29	0.0598
32.076	133.386	-177.761	0.078
32.202	133.622	172.861	0.0794
32.327	133.86	158.047	0.0679
32.452	134.098	145.644	0.0581
32.576	134.336	143.731	0.0517
32.7	134.576	150.75	0.0472
32.823	134.816	164.68	0.041
32.946	135.057	170.857	0.0404
33.068	135.299	158.148	0.0512
33.189	135.542	153.699	0.0591
33.309	135.785	156.285	0.0557
33.429	136.029	159.336	0.0492
33.549	136.274	162.093	0.0571
33.669	136.519	163.043	0.0607
33.79	136.764	165.244	0.0412
33.91	137.01	173.97	0.0471
34.029	137.257	176.406	0.0723
34.146	137.505	174.91	0.0782
34.263	137.754	170.37	0.0753
34.379	138.004	166.309	0.0687
34.496	138.255	166.463	0.0536
34.611	138.506	162.994	0.0286
34.726	138.758	135.172	0.0047
34.841	139.01	-42.067	0.0083
31.637	132.065	-166.816	0.0475

Table C.8 continued from previous page

31.766	132.298	-163.192	0.0323
31.894	132.532	-174.867	0.0177
32.021	132.767	162.834	0.0238
32.149	133.002	162.798	0.0403
32.275	133.238	160.74	0.0568
32.401	133.475	154.144	0.0671
32.527	133.713	145.565	0.0698
32.652	133.952	142.409	0.068
32.776	134.191	145.242	0.064
32.9	134.43	150.023	0.0586
33.023	134.671	158.777	0.047
33.146	134.913	162.578	0.0396
33.267	135.156	148.687	0.047
33.387	135.4	143.108	0.0526
33.507	135.644	148.163	0.0448
33.627	135.889	163.769	0.0336
33.748	136.134	167.969	0.0395
33.869	136.379	161.226	0.0449
33.99	136.624	156.246	0.029
34.112	136.869	154.455	0.0247
34.232	137.116	155.292	0.0343
34.349	137.365	153.674	0.0389
34.465	137.615	155.544	0.0412
34.581	137.866	160.16	0.042
34.697	138.117	163.817	0.0386
34.814	138.368	162.392	0.0294
34.93	138.619	165.36	0.0186
35.047	138.871	-160.699	0.0152
31.835	131.916	179.363	0.0513
31.965	132.148	167.627	0.0404
32.093	132.383	142.174	0.0344
32.221	132.618	132.343	0.041
32.348	132.854	137.297	0.0452
32.474	133.091	142.562	0.0539
32.6	133.328	143.852	0.0654
32.726	133.566	144.357	0.0729
32.851	133.805	147.184	0.0753
32.975	134.045	149.871	0.0739
33.1	134.285	148.929	0.0686
33.223	134.526	148.905	0.0559

Table C.8 continued from previous page

33.344	134.769	147.982	0.0456
33.464	135.014	141.284	0.0482
33.583	135.259	137.763	0.0485
33.703	135.504	144.268	0.0387
33.823	135.75	170.472	0.0309
33.944	135.995	175.116	0.0412
34.066	136.24	165.232	0.0507
34.188	136.484	160.814	0.041
34.312	136.729	156.037	0.0311
34.433	136.975	149.24	0.0284
34.55	137.225	145.077	0.028
34.664	137.477	152.655	0.0305
34.779	137.729	163.814	0.0369
34.895	137.981	168.361	0.0438
35.012	138.232	164.854	0.0475
35.129	138.484	162.993	0.0483
35.248	138.735	172.213	0.0476
32.028	131.769	173.113	0.0446
32.162	131.999	156.953	0.0492
32.292	132.233	141.669	0.0558
32.42	132.468	137.858	0.0604
32.547	132.704	142.42	0.0532
32.674	132.942	146.413	0.0522
32.799	133.18	146.988	0.0606
32.924	133.419	148.962	0.0699
33.049	133.659	151.73	0.0753
33.174	133.899	152.055	0.0752
33.298	134.139	147.88	0.0698
33.422	134.381	145.399	0.0579
33.542	134.625	147.418	0.0458
33.659	134.872	150.995	0.0407
33.776	135.12	152.511	0.0341
33.894	135.367	161.331	0.0244
34.014	135.613	-169.428	0.0221
34.135	135.858	-174.42	0.0322
34.258	136.103	170.717	0.0436
34.383	136.347	166.917	0.0435
34.51	136.589	164.585	0.038
34.634	136.834	158.084	0.0317
34.75	137.085	151.575	0.0257

Table C.8 continued from previous page

34.863	137.339	158.435	0.0248
34.976	137.592	170.922	0.0318
35.089	137.847	173.824	0.0437
35.202	138.102	166.972	0.0555
35.318	138.355	161.692	0.0646
35.438	138.606	165.788	0.0675
32.209	131.63	-175.178	0.0288
32.354	131.853	160.225	0.0468
32.489	132.083	147.516	0.0674
32.619	132.318	145.41	0.0732
32.747	132.554	151.259	0.0572
32.873	132.793	154.85	0.0463
32.998	133.032	151.486	0.0492
33.122	133.272	151.081	0.0584
33.247	133.512	151.653	0.0643
33.372	133.752	150.062	0.0641
33.497	133.993	145.897	0.0594
33.62	134.236	146.064	0.0484
33.737	134.483	156.882	0.035
33.851	134.733	178.464	0.027
33.964	134.983	-163.278	0.0205
34.081	135.231	-141.558	0.0136
34.202	135.477	-115.701	0.0124
34.325	135.722	-141.512	0.0132
34.449	135.967	-174.858	0.0215
34.575	136.21	-179.236	0.0304
34.705	136.45	177.877	0.035
34.834	136.693	169.185	0.0331
34.948	136.946	161.35	0.0248
35.059	137.202	166.28	0.0183
35.17	137.457	-178.008	0.0202
35.279	137.716	-176.851	0.0305
35.386	137.975	170.653	0.0444
35.497	138.232	161.273	0.0574
35.615	138.484	162.266	0.0621
32.373	131.505	-125.698	0.0288
32.532	131.717	-177.212	0.039
32.679	131.939	154.713	0.066
32.815	132.169	146.718	0.0766
32.945	132.404	147.015	0.0571

Table C.8 continued from previous page

33.071	132.643	146.757	0.0389
33.196	132.883	144.008	0.0365
33.32	133.124	146.72	0.0427
33.444	133.365	148.441	0.0454
33.569	133.606	146.811	0.0438
33.695	133.846	144.58	0.0417
33.818	134.09	148.035	0.0328
33.931	134.34	168.965	0.0194
34.038	134.596	-139.646	0.0138
34.147	134.85	-110.622	0.0122
34.263	135.1	-90.404	0.007
34.385	135.345	-42.584	0.0051
34.51	135.589	-59.877	0.0042
34.635	135.833	-130.869	0.0103
34.764	136.075	-145.393	0.0241
34.9	136.312	-156.112	0.0355
35.034	136.551	-171.422	0.039
35.146	136.806	178.998	0.0308
35.251	137.067	-176.881	0.0186
35.358	137.326	-152.055	0.0119
35.462	137.588	-144.708	0.0146
35.563	137.852	-171.142	0.0196
35.667	138.115	166.033	0.027
35.778	138.373	161.08	0.031
32.517	131.394	-108.03	0.0599
32.691	131.595	-139.019	0.0546
32.854	131.805	178.188	0.063
33.004	132.025	158.884	0.074
33.141	132.255	154.015	0.0601
33.269	132.493	153.311	0.0429
33.393	132.734	156.196	0.0364
33.515	132.977	164.363	0.0368
33.639	133.219	171.855	0.034
33.765	133.46	175.483	0.0285
33.892	133.699	173.862	0.0261
34.016	133.942	177.879	0.0202
34.122	134.199	-152.679	0.0109
34.218	134.463	-81.386	0.0095
34.32	134.723	-40.108	0.0062
34.433	134.976	74.93	0.0065

Table C.8 continued from previous page

34.554	135.223	91.232	0.0125
34.68	135.466	113.644	0.0091
34.807	135.709	-157.56	0.0136
34.942	135.947	-141.394	0.0335
35.09	136.176	-144.929	0.0499
35.235	136.408	-161.078	0.0558
35.341	136.668	-171.413	0.0435
35.437	136.935	-162.489	0.0213
35.536	137.201	-75.845	0.01
35.631	137.47	-42.007	0.0195
35.721	137.742	-31.726	0.0193
35.812	138.014	-9.051	0.014
35.911	138.281	24.465	0.0116